Eindhoven University of Technology

MASTER

Improving RAPTOR tokamak plasma profile simulations
neutral beam injection module and automated model parameter optimization

Geelen, P.J.M.

Award date:
2013

Link to publication

Improving RAPTOR tokamak plasma profile simulations: Neutral Beam Injection module and automated model parameter optimization

Author:
Paul Geelen

Supervisors:
Dr. Ir. Federico Felici
Dr. Ir. Maarten De Bock

Abstract

The q-profile, also known in literature as the safety factor profile, is an important quantity because it determines the stability as well as the performance of a fusion plasma. A strong degree of control over this q-profile makes the operation of a tokamak fusion reactor more stable (avoidance of plasma instabilities) and efficient (optimal q-profile shape). Control of the q-profile can be achieved through either open-loop (feedforward) control or closed-loop (feedback) control, or a combination of both. For the development and testing of both types of control a fast control-oriented transport code which can simulate the evolution of the safety factor profile in time is crucial. The RAPTOR (RApid Plasma Transport simulatOR) code was developed with this aim in mind. The performance of the open-loop and closed-loop control system strongly depends on the quality of the RAPTOR predictions.

During this research the predictions of RAPTOR were improved by adding a fast Neutral Beam Injection module (NBI) and by developing a generic method to estimate the model parameters in RAPTOR.

The NBI system is an important external heating and current drive actuator to alter the q-profile of a fusion plasma. It is used at many existing tokamaks and will be an important actuator for ITER. The developed fast Neutral Beam Injection module, based on a pencil beam approach, produces results similar to more complete beam codes for an ITER-like scenario.

In RAPTOR an ad-hoc model is used, instead of a first principle physics model, to describe the electron heat diffusivity χ_e in view of computational speed. The structure of the ad-hoc model is given by the physics knowledge, and only the unknown physics of χ_e, which is more complicated and less well understood, is captured in its model parameters. During this research on the one hand the ad-hoc model was extended in order to better describe physical phenomena such as the sawtooth instability and the degradation of transport due to higher temperature. On the other hand a generic parameter identification method was developed to estimate RAPTOR's model parameters. For the TCV tokamak in Lausanne it was shown that the developed method is capable of finding the model parameters such that the RAPTOR predictions agree within twenty percent with measurements.

As a result of the work presented in this thesis, the RAPTOR code is now equipped with a NBI module that allows RAPTOR to simulate a multitude of tokamaks including ITER. Benchmarks of this fast NBI module for an ITER-like scenario showed good agreement with large scale NBI codes, while running significantly faster. Furthermore the extension of the transport model and a newly developed model-parameter estimation routine now results in a better description of the physics and allows for a less ad-hoc and more automated method to implement RAPTOR on a variety of tokamaks.

Contents

Chapter 1

Introduction

1.1 Introduction

Fusion energy is a promising source of energy which has several advantages over the conventional energy sources [1]:

1. Universal availability and virtually inexhaustible fuel (heavy water and lithium);

2. No emission of greenhouse gases or other combustion pollutants such as SO_x and NO_x;

3. No long lived or high level radioactive waste.

The fusion process involves two light nuclei, typically isotopes of hydrogen, that are merged together to form a new set of elements. The most promising reaction to occur involves the fusion of a deuterium nucleus (D) and a tritium nucleus (T). This reaction creates a helium nucleus and an energetic neutron which is used to generate electricity:

$$D + T \rightarrow^4 He(3.5MeV) + n(14.1MeV), \tag{1.1}$$

The fusion deuterium-tritium fuel must be heated to a high temperature so that the thermal velocities of the nuclei are sufficiently high to overcome the mutual Coulomb repulsive forces and produce the required reactions. The required temperature is about 100 million degrees C [9]. At this temperature the fusion fuel is in the form of a plasma (a "gas" of charged particles) and cannot be contained by material walls.

A solution to avoid contact of the plasma with the walls is to confine the plasma magnetically. The tokamak exploits this principle: it uses magnetic coils and plasma current which generate a helical field that confines the hot plasma. This machine is shaped like a torus and its field lines are "closed", i.e. they form nested flux surfaces. Plasma particles (ions and electrons) are free to move along the magnetic field lines but their motion across magnetic field lines is strongly inhibited. A schematic of the tokamak configuration and its coils are shown in Figure 1.1. The TCV experiment at the École Polytechnique Fédérale de Lausanne is one of an estimated 25 devices in the world which exploits this concept.

The magnetic geometry determines the stability and confinement of the plasma. A key attribute of a tokamak is that the helical field is generated by a current driven in the plasma while the shape of the magnetic surfaces (e.g. elongation, triangularity) can be controlled with external magnets. The radial profile of plasma current determines the q profile (In many literature also defined as the safety factor profile). The latter represents how many toroidal periods a field line covers for one poloidal period. In Figure 1.2 the radial q and parallel current density profiles are depicted. The shape of the safety factor profile determines in which plasma scenario the tokamak is operating. The different plasma scenarios mentioned in Figure 1.2 have the following features:
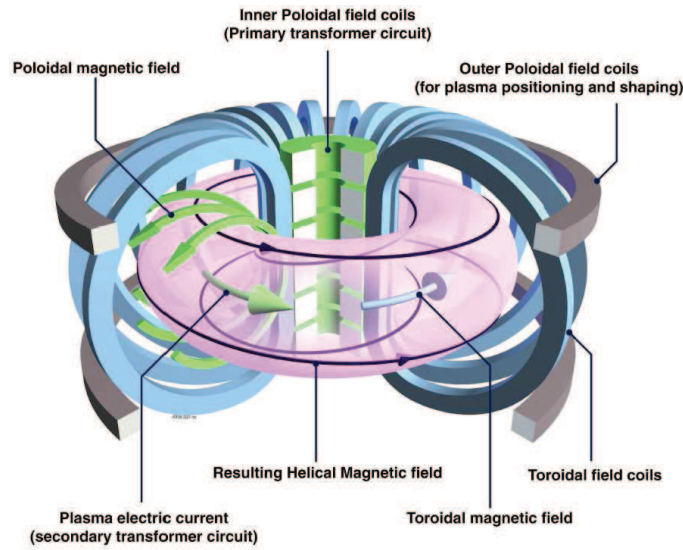
Figure 1.1: A schematic of the tokamak configuration showing the major components. (Figure reprinted from [2])
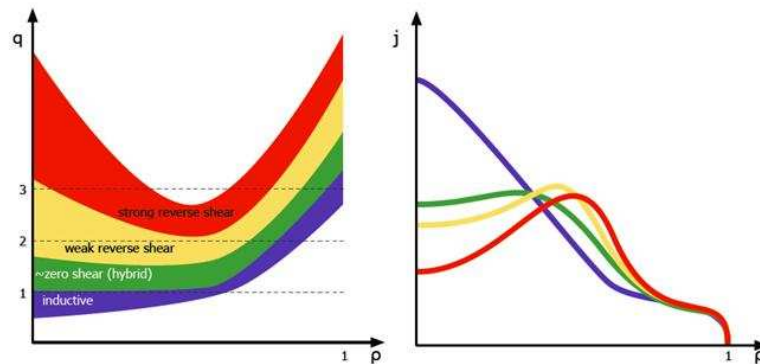
Figure 1.2: The different q profiles, which are determined by the radial distribution of the parallel current density j, define the different tokamak operating scenarios. The normalized radial coordinate ρ is zero in the center of the plasma and one at the plasma edge (Figure reprinted from [3])

- The inductive plasma scenario (the High Confinement Mode) is the most promising scenario for ITER to reach a fusion power output ten times higher than the input heating power of the plasma. The inductive plasma scenario is characterized by a peaked current density profile (most plasma current is driven inductively) and a resulting monotonic q profile. Because q is smaller than one near the plasma center, sawtooth crashes of the plasma can occur. This deteriorates the performance (lower energy gain) and may serve as a trigger for other deleterious MHD modes;

- The hybrid plasma scenario is characterized by a centrally flat (zero shear) q profile which is greater than one everywhere. This q profile is achieved by driving a significant part of the plasma current non-inductively off-axis. The absence of a $q = 1$ surface means that no sawtooth crashes occur. (More information about sawtooth crashes is given in Section 4.1);

2

- In the advanced scenarios (weak reverse shear, strong reverse shear) a significant amount of plasma current is driven off-axis and non-inductively. This causes a reversed/non-monotonic q profile, which triggers internal transport barriers (ITB) resulting in locally reduced transport and thus improved energy confinement. A disadvantage of the advanced scenarios is that they must operate close to the ideal magnetohydrodynamics (MHD) stability limits.

It can be concluded that the q profile is an important quantity because it determines the stability as well as the performance of a fusion plasma. A strong degree of control over this q profile makes the operation of a tokamak more stable and efficient. The success of ITER, the world's largest tokamak yet to be built, strongly depends on the ability to control and shape this safety profile. Control of the safety factor profile can be achieved through either open-loop (feedforward) control or closed-loop (feedback) control, or a combination of both. Open-loop control is used to calculate the trajectory that the profiles should follow during their transient evolution towards/from their stationary state. Closed-loop control is used to maintain the desired profiles in real-time around an operating point.

For development and testing of both types of control a fast transport code which can simulate the temporal evolution of the safety factor profile is crucial. The RAPTOR (RApid Plasma Transport simulatOR) code [3] was developed for this purpose. It is a fast code to calculate the coupled electron temperature T_e and q profile evolution: to calculate the safety factor profile, information about the electron temperature is needed and vice versa. Besides the fast calculation of the T_e and q profiles, RAPTOR returns the sensitivity of the time evolution of these profiles to a set of model or input parameters. This last feature proved to be extremely useful and makes RAPTOR unique compared to other existing codes. In Chapter 2 the equations and assumptions used in RAPTOR are explained. In the remaining of this section a brief introduction is given on feedforward and feedback control and the role of RAPTOR in these control schemes. This introduction will serve to motivate in Section 1.3 the added value and applications of the work presented in this thesis.

Feedforward control

An important task of tokamak physics operators at the different tokamak research facilities in the world consists of the design of plasma evolution trajectories. A trajectory is the time evolution of a tokamak actuator, e.g Electron Cyclotron Heating and Current Drive or Neutral Beam Heating and Current Drive. The tokamak physics operator determines pre-shot (*open loop*) the auxiliary heating, current drive and plasma current trajectories necessary to reach a given plasma scenario. These plasma scenarios are determined by their q profile (See Figure 1.2). By actively shaping the q profile, known as profile control, a desired plasma scenario can be reached. The choice of actuator trajectories made by the tokamak physics operator to reach a plasma scenario is traditionally the result of a substantial amount of trial-and-error attempts and his extensive experience gained during tokamak operation. The RAPTOR code offers an alternative approach for the planning of open loop trajectories. Coupling RAPTOR to a nonlinear optimization routine makes it possible to calculate which actuator trajectories are necessary to reach a prescribed q profile and thus a desired plasma scenario. This approach is sketched in Figure 1.3. The cost function defines how much the final q profile deviates from the desired one. The nonlinear optimization routine takes actuator constraints (e.g: maximum power of actuator and ramp rate) and physics constraints (e.g avoiding sawtooth crashes by the constraint $q > 1$ everywhere at all times) into account.

RAPTOR is a light-weight, control-oriented transport code capable of calculating the safety factor profile evolution in time as well as the profile sensitivity to a set of model parameters or input parameters (affecting the temporal evolution of the actuator trajectories). This information can be fed to the nonlinear optimization routine. This routine uses the profile sensitivities to compute an improved set of actuator trajectories, iteratively converging to an optimum. If the analytic expressions for the profile sensitivities were not available they would have to be obtained numerically. This would increase the CPU burden significantly knowing that typically hundreds of iterations are necessary to calculate the optimal actuator trajectories and that at each iteration step the extra amount of simulations required to calculate the numerical profile sensitivity scales with the
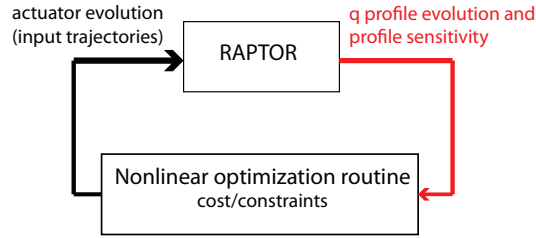
Figure 1.3: Schematic of the approach to calculate actuator trajectories. RAPTOR, which simulates the tokamak profile, is coupled to a nonlinear optimization routine to calculate the required actuator trajectories to reach a specified q profile.

number of input parameters. Other existing fast transport codes do not provide the analytical expressions for the profile sensitivities, which makes RAPTOR a very suitable code for designing optimal feedforward trajectories regarding tolerable CPU times.

There are multiple advantages using the RAPTOR code for open loop trajectory planning:

1. The numerical approach can reduce the number of trial-and-error attempts. In this way RAPTOR can provide the required actuator trajectories to reach a plasma scenario more rapidly and at lower cost in terms of machine time;

2. The proposed method [3] is applicable to machines which are yet to be built, such as ITER. In the ITER experiment actuator trajectories must be designed with great caution, because the occurrence of plasma instabilities (e.g Neoclassical Tearing Modes) could seriously damage the machine. RAPTOR can reduce the number of trial-and-error attempts, saving costly machine operation time;

3. New and better (e.g. reach more rapidly a stationary state for the plasma q profile) trajectories could be discovered. In addition to this, the discovered unexpected actuator trajectories could lead to new insight;

4. Since actuator and physics constraints are explicitly included in the trajectory design, the obtained trajectories can be analyzed with respect to their influence on the various constraints, and vice versa.

Feedback control

Feedback control methods differ from the feedforward method by the fact that real-time profile measurements are used to decide the appropriate real-time actuator responses to obtain the desired q and T_e profiles. While with feedforward control the required actuator actions are only determined once pre-shot, in feedback control the actuator settings are constantly adjusted during a shot to reduce the difference between the measured profiles and the desired ones.

Instead of only using measurements which are restricted to a certain spatial resolution and measuring frequency, RAPTOR can be used in the feedback control schemes. Due to its speed it estimates the future behavior of the plasma faster than it actually happens in real-time and at any desired spatial resolution. For this purpose RAPTOR is included as prediction model in a state observer (e.g. a Kalman Filter). At each step in a state observer, RAPTOR is used in a time update step to generate a predicted state estimate, from which a set of predicted measurements is computed. This state estimate is then complemented and improved based on the discrepancy between predicted measurements and actual measurements in a measurement update step, yielding an updated state estimate. A key advantage of this approach is that a state estimate is available at an arbitrary spatial and temporal scale, which provides a solid framework on which various plasma measurements can be collected and interpreted.

With the availability of a real-time plasma state observer, numerous state feedback control techniques become feasible for use in plasma profile control. RAPTOR contains analytical expressions to calculate the state sensitivities. A fast calculation of local linearizations is possible due to this feature and LTI control techniques, such as LQR or H-infinity control become candidates for closing the control loop. The ability of the transport simulation code to also predict future behavior of the plasma enables the use of another promising technique: model-predictive control. Some promising results of this control scheme were reported in [4].

1.2   Problem formulation

RAPTOR can be used to design control systems in order to tailor the q-profile to a desired operation regime by means of an open-loop and/or closed-loop control approach. A strong degree of control over this q profile makes the operation of a tokamak more stable (avoidance of plasma instabilities) and efficient (optimal q profile).

The performance of the open-loop and closed-loop control system strongly depends on the quality of the RAPTOR predictions. RAPTOR achieves its fast computational speed by using simplified physics and approximations. A major assumption in RAPTOR is the ad-hoc model for the heat diffusivity term χ_e, as will be further discussed in Chapter 4. The structure of the model is given by the physics knowledge, and only the unknown physics of χ_e which is more complicated and less well understood is captured in the model coefficients. These model coefficients need to be tuned for each tokamak individually in order to match the predictions for the evolution of the radial evolution of the electron temperature T_e and q profiles with experimental evidence. The model parameters in χ_e cannot be computed directly with existing theory. Computationally heavy gyrokinetic simulations could be used to calculate the heat diffusivity profile, but this would require massive computation time. Therefore the coefficients are manually tuned to experimental data. This approach is time consuming and lacks a systematic character. This motivates the development of generic method to estimate the model parameters.

Besides the lack of a systematic way to estimate the model parameters, RAPTOR does not contain a Neutral Beam Injector (NBI) model. The NBI system is an important external heating and current drive actuator to alter the q profile shape of a fusion plasma. It is used at many existing tokamaks and will be an important actuator for ITER. The missing NBI model in the control oriented RAPTOR code limits its applicability to these tokamaks.

1.3   Aim of this work

The general aim is to improve RAPTOR predictions of the T_e and q profile evolution. This is achieved in particular by

1. Developing a light-weight Neutral Beam Injector (NBI) model for RAPTOR in Chapter 3 to calculate the deposited power to the electron and current drive in the plasma;

2. Adding more physics to the heat diffusivity χ_e and electrical conductivity σ models in Chapter 4 by incorporating the effect of external heating and sawtooth crashes;

3. Developing a generic parameter identification method in Chapter 5 to make the best possible estimates of the χ_e model coefficients when measured data or interpretative simulations of the T_e and q profiles are available.

With these improvements, it is expected that the RAPTOR predictions will be more accurate. This enhances the performance of the open-loop and closed-loop control system and ultimately makes the operation of a tokamak more stable and efficient.

Chapter 2

The RAPTOR code

RAPTOR (RApid Plasma Transport simulatOR) is a lightweight, simplified transport code complex enough to contain the most important physics and sufficiently fast to use for feedforward and real-time feedback control. RAPTOR solves the coupled poloidal flux diffusion equation and electron temperature transport. By using assumptions the RAPTOR code is simpler and contains less physics than existing transport codes such as ASTRA [5] and CRONOS [6]. In [3] it is shown that by making the right choices of which physics to simplify, results comparable to these heavier codes have been obtained. RAPTOR has the unique feature to return not only the profile evolution but also the sensitivity of the profile evolution to a chosen set of parameters. This chapter, which is largely based on [3], start with the main equations for the poloidal flux diffusion, energy transport and particle transport and is followed by the reduced physics model that is solved by RAPTOR. The main assumptions that leads to this reduced physics model are explained as well.

2.1 Poloidal flux diffusion equation

In Figure 2.1 the coordinate system which is used in this thesis is introduced. The various plasma quantities that will be used throughout the text are indicated as well.
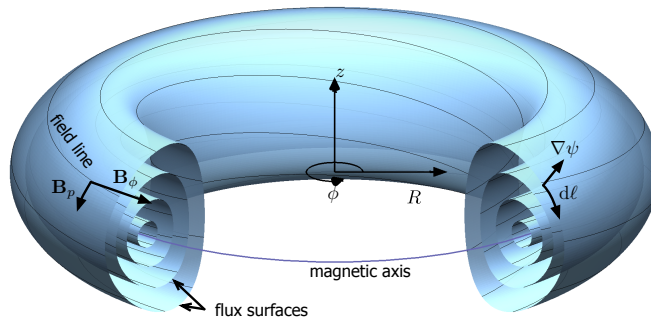
Figure 2.1: Definition of the used coordinate system and multiple plasma parameters. (Figure reprinted from [3])

The poloidal magnetic flux is defined as

$$\psi = -\int \mathbf{B} \cdot \mathbf{dA_z}, \tag{2.1}$$

The magnetic field $\mathbf{B}$ is composed out of a toroidal component (parallel to $\mathbf{e}_\phi$) and poloidal component (orthogonal to $\mathbf{e}_\phi$). The poloidal magnetic flux is a measure of the flux of the magnetic

field through a disk of radius R, perpendicular to $\mathbf{e_z}$.

Besides the poloidal magnetic flux, also a toroidal magnetic flux definition can be defined

$$\Phi = \int \mathbf{B} \cdot \mathbf{dS}_\phi,$$

The toroidal magnetic flux Φ is a measure for how many magnetic field lines cross the surface area $\mathbf{dS}_\phi$ enclosed by a magnetic flux surface. The flux label ρ can be introduced from the definition of the toroidal magnetic flux

$$\rho = \sqrt{\frac{\Phi}{\pi B_0}}, \tag{2.2}$$

In this equation B_0 is the magnitude of the magnetic field at the magnetic axis R_0. The flux label ρ can be used to label the flux surfaces in the poloidal plane. Each flux surface has an unique label, ranging from $\rho = 0$ at the magnetic axis to $\rho = \rho_e$ at the plasma edge.
From Equation 2.1 it can be seen that the current density parallel to the magnetic field $\mathbf{B}$ is linked to ψ, because this current density has a component in the $\mathbf{e}_\phi$ direction which creates a magnetic field that is parallel to $\mathbf{dA_z}$.

The objective of the RAPTOR code is to simulate the radial evolution of the q profile in time. The q profile is defined as

$$q = \frac{\partial \Phi}{\partial \psi},$$

Its reciprocal, the rotational transform, ι is

$$\iota = \frac{1}{q},$$

The q profile is determined by the current density parallel to the magnetic field $\mathbf{B}$ (see Figure 1.2). From Ohm's law the expression for this current density parallel to the magnetic field $\mathbf{B}$ can be formulated

$$j_\| = \sigma_\| E_\| + (j_{bs} + j_{cd}), \tag{2.3}$$

The first term in the righthand side of the equation is the inductive current drive, the two other terms are non inductive current sources. The term j_{bs} represents the bootstrap current. This current arises due to the radial pressure gradient in a tokamak. The second non inductive current source j_{cd} is the auxiliary current drive. Examples are current driven by a neutral beam injection system or electron cyclotron (heating) system.
Averaging Equation 2.3 over a flux surface and taking into account that $\sigma_\|$ is constant on a flux surface yields

$$j_\| = \sigma_\| E_\| + < (j_{bs} + j_{cd}) >, \tag{2.4}$$

In Equation 2.4 $j_\|$ and $E_\|$ are coupled and can be written as function of ψ. After some math (For details see [3]) Equation 2.4 can be formulated as

$$\sigma_\| \Big(\frac{\partial \psi}{\partial t} + \frac{\rho \dot{B}_0}{2 B_0} \frac{\partial \psi}{\partial \rho} \Big) = \frac{R_0 J^2}{\mu_0 \rho} \frac{\partial}{\partial \rho} \Big(\frac{G_2}{J} \frac{\partial \psi}{\partial \rho} \Big) - \frac{V'}{2\pi\rho} (j_{bs} + j_{cd}), \tag{2.5}$$

with

$$\dot{B}_0 = \frac{\partial B_0}{\partial t};$$

$$J = \frac{RB_\phi}{R_0 B_0} \; ; \qquad\qquad \text{J reflects the diamagnetic or paramagnetic effect of the plasma}$$

$$G_2 = \frac{V'}{4\pi^2} \left\langle \frac{(\bigtriangledown \rho)^2}{R^2} \right\rangle \; ; \qquad\qquad \text{Geometric quantity depending only on the fluxsurface geometry}$$

$$V' = \frac{\partial V}{\partial \rho} \; . \qquad\qquad \text{V is the volume enclosed by a fluxsurface}$$

Equation 2.5 is a parabolic partial differential equation and is known in literature as the poloidal flux diffusion equation. Due to the introduction of the ρ coordinate this equation is $1D$. The poloidal flux diffusion equation is used to calculate the spatial profile of the poloidal flux ψ evolving in time under the influence of inductive and non-inductive current drive sources.

This spatial poloidal flux ψ profile is used together with Equation 2.2 to obtain the q profile

$$q = \frac{\partial \Phi}{\partial \psi} = 2\pi B_0 \rho \frac{\partial \rho}{\partial \psi}$$

2.2   Particle and energy transport

In order to calculate the conductivity $\sigma_\parallel$, bootstrap current and auxiliary current, information about the radial T_e, T_i, n_e and n_i profiles is needed. The n_e and n_i profiles follow from the continuity equation

$$\frac{\partial n_\alpha}{\partial t} + \bigtriangledown \cdot (n_\alpha \mathbf{u}_\alpha) = s_\alpha, \tag{2.6}$$

Here s_α is the localized particle source and $\mathbf{u}_\alpha$ the local velocity of the electrons or ions ($\alpha = i$ or e).

The T_e and T_i profiles follow from the electron and ion energy transport

$$\frac{3}{2}(V')^{5/3} \Big(\frac{\partial}{\partial t} - \frac{\dot{B}}{2B_0} \frac{\partial}{\partial \rho} \rho \Big) \Big[(V')^{-5/3} n_\alpha T_\alpha \Big] + \frac{1}{V'} \frac{\partial}{\partial \rho} \Big(q_\alpha + \frac{5}{2} T_\alpha \Gamma_\alpha \Big) = P_\alpha, \tag{2.7}$$

In this equation P_α is the net external and ohmic power ($P_{ohmic} = jE$) to the species, Γ_α and q_α are the convective and diffusive heat fluxes respectively.

Equations 2.5, 2.6 and 2.7 form a set of five coupled differential equations which are used to solve the radial evolution of the poloidal flux ψ in time and hence the q profile.

2.3   Reduced physics model

The aim of RAPTOR, as indicated by its name RApid Plasma Transport simulatOR, is to provide a fast control-oriented transport physics code. This fast code opens a wide variety of application possibilities as already discussed in the introduction of this thesis. In RAPTOR the set of five coupled differential equations are simplified resulting in a reduced physics model. The assumptions yielding to this reduced physics model are discussed in this section

The RAPTOR code solves the 1D profile diffusion equations 2.5 and 2.7 for $\psi(\rho,t)$ and $T_e(\rho,t)$ respectively. The other kinetic profiles T_i, n_e and n_i are kept fixed. The first motivation for this assumption is that the most important nonlinear coupling between plasma profiles during a tokamak discharge originates from the electron temperature-dependent conductivity $\sigma_\parallel$, bootstrap current $j_{bs}(n_e, T_e)$ and the q profile dependent confinement. The second motivation is that actuators for temperature and current density are reasonably effective while the density profile is in practice less well controlled during a discharge and globally follows a pre-defined evolution. By

assuming fixed T_i, n_e and n_i profiles one needs to solve only two coupled differential equations instead of five to obtain the q profile.

On top of the assumptions for the kinetic profiles four more assumptions are made to yield a reduced model for the ψ and T_e profile evolution. These will be discussed in the remaining of this section.

Fixed equilibrium assumption

In RAPTOR a fixed equilibrium is assumed. As a result the flux surface geometry and enclosed toroidal flux Φ (and hence the distribution of ρ) are fixed. Note that this does allow the poloidal flux profile ψ, and hence q to change in time. As a consequence of the fixed equilibrium, the vacuum toroidal magnetic field B_0 is constant ($\dot{B}_0 = 0$) and the geometric profile quantities G_1, G_2, V' and J are fixed in time and only need to be computed once. In [3] it is shown that the fixed equilibrium assumption is valid for a wide range of β (= plasma pressure/magnetic pressure) values.

Ad-hoc transport model and losses

The electron energy transport equation 2.7 depends on the convective Γ_α and diffusive q_α heat fluxes. In RAPTOR the convective heat flux, usually small and very hard to measure, is neglected ($\Gamma_\alpha = 0$) and for the diffusive heat flux it is assumed that the electron temperature gradient is the only driving source. This results in

$$q_e = -V'G_1 n_e \chi_e \frac{\partial T_e}{\partial \rho}, \tag{2.8}$$

For the electron heat diffusivity χ_e RAPTOR uses an ad-hoc model, which presently takes anomalous diffusion and the q profile dependent confinement into account. This model was extended to incorporate the effect of sawteeth and the nonlinear effect of confinement deterioration with increasing temperature gradient, which indirectly depends on external heating. More details on the ad-hoc model and the modifications are given in Chapter 4.

Neoclassical conductivity and bootstrap current

The neoclassical conductivity depends on the electron temperature. The expression that is used in RAPTOR is

$$\sigma_\| = c_{neo}(\rho)\sigma_{Spitzer}(T_e(\rho,t)) \propto c_{neo}(\rho)T_e[eV]^{3/2},$$

In the above formula c_{neo} represents the neoclassical correction, which depends on geometric effects and collisionality [3]. In RAPTOR this term is calculated only once for an equilibrium.

For the bootstrap current in Equation 2.5 a simplified expression is obtained by assuming $n_e = n_i$ and $\frac{\partial \ln T_e}{\partial \psi} = \frac{\partial \ln T_i}{\partial \psi}$

$$j_{bs} = -\frac{2\pi J(\psi)R_0}{R_{pe}}\frac{\partial \rho}{\partial \psi}\left[\zeta_{31}\frac{\partial n_e}{\partial \rho}T_e + (\zeta_{31} + R_{pe}\zeta_{32} + (1 - R_{pe})\alpha\zeta_{34})\frac{\partial T_e}{\partial \rho}n_e\right],$$

Here $R_{pe} = p_e/p$ is the ratio between electron and total pressure and the coefficients ζ_{31}, ζ_{32}, ζ_{34}, α depend on geometric effects and collisionality [3]. These coefficients are, like c_{neo}, only evaluated once for a given equilibrium.

Parameterized external heating and current drive sources

Presently RAPTOR has only a model for electron cyclotron current drive (ECCD) and electron cyclotron heating (ECH). Extensive models for ECCD and ECH calculations exist (e.g. TORAY [10] or LUKE [11]), but to reduce the computational cost RAPTOR approximates the power and

current densities by weighted gaussian distributions. The power density to the electrons P_e is modeled as

$$P_e(\rho, t) = P(t)\exp\left(\frac{-4(\rho - \rho_{dep})^2}{w_{dep}^2}\right) \Big/ \int_0^{\rho_e} \exp\left(\frac{-4(\rho - \rho_{dep})^2}{w_{dep}^2}\right)V'd\rho,$$

with ρ_{dep} the location of the peak of the deposition and w_{dep} the deposition width.
For the current density the following heuristic expression is used

$$j_{cd}(\rho, t) = c_{cd}e^{\rho^2/0.25}\frac{T_e}{n_e}e^{-4(\rho - \rho_{dep})^2/w_{dep}^2}P(t),$$

The factor c_{cd} is used to calibrate this expression to a specific machine.

In many existing tokamaks not only ECH, ICRH (ion cyclotron resonant heating) and ECCD are used for auxiliary heating and current drive but also a Neutral Beam Injection (NBI) system. For ITER, the largest tokamak presently under construction, the NBI system will be a vital actuator to reach a high net energy gain. In Chapter 3 a physical model for the NBI electron heating and current drive is presented which allows RAPTOR to be used for feedback and feedforward control at ITER and many existing tokamaks that utilize a NBI system.

Reduced physics model

By taking all the assumptions in this section into account the flux diffusion equation 2.5 reduces to

$$\sigma_\parallel \frac{\partial \psi}{\partial t} = \frac{R_0 J^2}{\mu_0 \rho} \frac{\partial}{\partial \rho}\left(\frac{G_2}{J}\frac{\partial \psi}{\partial \rho}\right) - \frac{V'}{2\pi\rho}(j_{bs} + j_{cd}), \tag{2.9}$$

Equation 2.7 for the spatial evolution of the electron temperature T_e in time becomes

$$V'\frac{\partial}{\partial t}[n_e T_e] = \frac{\partial}{\partial \rho}G_1 V' n_e \chi_e \frac{\partial T_e}{\partial \rho} + V' P_{e,\text{ohmic \& external}}, \tag{2.10}$$

Solving the reduced physics model

RAPTOR solves this set of two coupled nonlinear parabolic PDEs using a finite elements approach. The continuous profiles $\psi(\rho, t)$, $T_e(\rho, t)$ are transformed to [3]

$$\psi(\rho, t) = \sum_{\alpha=1}^{n_{sp}} \Lambda_\alpha(\rho)\hat{\psi}_\alpha(t) \quad \text{and} \quad T_e(\rho, t) = \sum_{\alpha=1}^{n_{sp}} \Lambda_\alpha(\rho)\hat{T}_{e\alpha}(t),$$

in which $\Lambda_\alpha(\rho)$ is a basis function and $\hat{\psi}_\alpha(t)$ and $\hat{T}_{e\alpha}(t)$ are the coefficients. The continuous $\psi(\rho, t)$ and $T_e(\rho, t)$ profiles are transformed to a linear combination of n_{sp} basis functions. A state vector x can be introduced containing the basis functions coefficients $\hat{\boldsymbol{\psi}}(t) = [\hat{\psi}_1(t), ..., \hat{\psi}_{n_{sp}}(t)]^T$ and $\hat{\boldsymbol{T}}_{\boldsymbol{e}}(t) = [\hat{T}_{e1}(t), ..., \hat{T}_{en_{sp}}(t)]^T$

$$x(t) = \left[\begin{array}{c} \hat{\boldsymbol{\psi}}(t) \\ \hat{\boldsymbol{T}}_{\boldsymbol{e}}(t) \end{array}\right], \tag{2.11}$$

By the introduction of the state vector $x(t)$, Equations 2.9 and 2.10 can be formulated as

$$f = f(\dot{x}(t), x(t), u(t)) = 0 \quad \forall t$$

After discretizing the time $t = [t_0, ..., t_k, ...t_{n_k}]$, this continuous equation is discrete

$$f_k = f(x_{k+1}, x_k, u_k) = 0 \quad \forall k \tag{2.12}$$

This equation is solved iteratively at each time step k to obtain the state x_k. Once the state vector is known, all the important ι, T_e and U_{pl} profiles in this thesis can be calculated as follows

$$\iota(\rho, t_k) = \boldsymbol{c}_\iota^T(\rho)\hat{\boldsymbol{\psi}}(t_k), \tag{2.13}$$

$$U_{pl}(\rho, t_k) = \boldsymbol{c}_\Lambda^T(\rho)\dot{\hat{\boldsymbol{\psi}}}(t_k), \tag{2.14}$$

$$T_e(\rho, t_k) = \boldsymbol{c}_\Lambda^T(\rho)\hat{\boldsymbol{T}}_{\boldsymbol{e}}(t_k), \tag{2.15}$$

where the vector elements are given by

$$[\boldsymbol{c}_\iota(\rho)]_\alpha = \frac{1}{2\pi B_0 \rho}\frac{\partial \Lambda_\alpha}{\partial \rho},$$

$$[\boldsymbol{c}_\Lambda^T(\rho)]_\alpha = \Lambda_\alpha$$

Chapter 3

Development of a lightweight NBI module for RAPTOR

Neutral beam Injection heating (NBIH) and current drive (NBCD) are robust methods to heat the plasma and to drive a non-inductive current. It does not depend on coupling conditions at the edge or a resonance frequency like is the case for electron/ion cyclotron heating. In this chapter a model is presented to calculate the neutral beam electron heating and current drive. This model will be used in the RAPTOR code and serves as an additional actuator to influence the plasma contained in a tokamak. Because the beam code will be coupled to RAPTOR it is required that the code is sufficiently fast to run very rapidly, yet sufficiently complex to contain the most important physics. Therefore a pencil beam approach was used: the neutral beam is represented by a single line, neglecting finite beam width effects. More assumptions were made to enhance the speed of the NBI code. To retain RAPTOR's unique feature to provide the sensitivity of the T_e and q profile time evolution to a set of model or input parameters, effort was made during the development of the NBI code to provide the analytical expressions of the sensitivities of the neutral beam heating and current drive to its model and input parameters. The NBI model and all the assumptions are explained in this chapter as well as results of the code in comparison with other existing beam codes which contain more physics.

3.1 Neutral beam electron heating

3.1.1 Model

The total beam power at the plasma edge of the tokamak is defined as P_a. The power losses between the acceleration grid and the plasma edge are taken into account in this number. The beam power for a given energy E is related to the total beam density $n_{tot,a}$ simply by $P_a = v_{beam} E n_{tot,a}$. There are three basic atomic processes leading to beam absorption: charge exchange, ionization by ions and ionization by electrons. The absorption of the beam depends upon the cross-section for these processes $\sigma(E, n_e, T_e, Z_{eff})$. Janev's fitting formula provides a suitable analytic expression for $\sigma(E, n_e, T_e, Z_{eff})$ for a single-impurity plasma [7]

$$\sigma(E, n_e, T_e, Z_{eff}) = \frac{e^{S_1(E, n_e, T_e)}}{E}[1 + (Z_{eff} - 1)S_z(E, n_e, T_e)]10^{-20}\mathrm{m}^2,$$

where

$$S_1 = \sum_{i=1}^{2}\sum_{j=1}^{3}\sum_{k=1}^{2} A_{ijk}(\ln E)^{i-1}[\ln(n/n_0)]^{j-1}(\ln T_e)^{k-1} \tag{3.1}$$

$$S_z = \sum_{i=1}^{3}\sum_{j=1}^{2}\sum_{k=1}^{2} B_{ijk}(\ln E)^{i-1}[\ln(n/n_0)]^{j-1}(\ln T_e)^{k-1}, \tag{3.2}$$

with E, n_e, T_e expressed in units of keV/u, cm^{-3} and keV, respectively, and $n_0 = 10^{13}$ cm^{-3}. A_{ijk} and B_{ijk} are fitting coefficients depending on the plasma impurity. The values are tabled in [7]. Inspection of the behavior of the beam stopping cross-section on the parameters E, n_e, Z_{eff} and T_e shows that only the dependencies of the cross-section on E and Z_{eff} are strong [7]. This allows for the following assumption to make the calculation of the cross-section computationally faster: $\sigma(E, n_e, T_e, Z_{eff}) \approx \sigma(E, Z_{eff})$. In Equations 3.1 and 3.2 n_e and T_e can be set to their mean values.

Since the injected neutrals go in a straight line, because they are not affected by the magnetic field, the decay of the beam particle density on a straight line path $\mathrm{d}s$ is governed by the equation [9]

$$n_{tot,s} = n_{tot,a} e^{- \int_{s=a}^{s} n_e(s)\sigma(E,Z_{eff})\,\mathrm{d}s},$$

The beam power at a location on the beamline inside the plasma is

$$P(s) = v_{beam} E n_{tot,s} = v_{beam} E n_{tot,a} e^{- \int_{s=a}^{s} n_e(s)\sigma(E,Z_{eff})\,\mathrm{d}s} = P_a e^{- \int_{s=a}^{s} n_e(s)\sigma(E,Z_{eff})\,\mathrm{d}s}, \quad (3.3)$$

A hydrogen neutral beam mainly produces H, H_2 and H_3 particles. A deuterium beam mainly produces D, D_2 and D_3 particles. The particles of a hydrogen or deuterium beam have an energy of respectively E, E/3 and E/3. The total power P_a is divided over these beam particles according to the ratio $P_{frac,1}$, $P_{frac,2}$ and $P_{frac,3}$ respectively. In order to compute the total beam power at a location inside the plasma, a summation over the different beam particles is done

$$P_{beam}(s) = P_a \sum_{i=1}^{3} P_{frac,i} e^{- \int_{s=a}^{s} n_e(s)\sigma(E/i,Z_{eff})\,\mathrm{d}s},$$

The beam power deposited in the plasma per unit length is

$$-\frac{\mathrm{d}P_{beam}(s)}{\mathrm{d}s} \approx \frac{P_{beam}(s - \Delta s/2) - P_{beam}(s + \Delta s/2)}{\Delta s},$$

which can be derived as:

$$-\frac{\mathrm{d}P_{beam}(s)}{\mathrm{d}s} = P_a n_e(s) \sum_{i=1}^{3} \sigma(E/i, Z_{eff}) P_{frac,i} e^{- \int_{s=a}^{s} n_e(s)\sigma(E/i,Z_{eff})\,\mathrm{d}s}, \quad (3.4)$$

This beam power deposited in the plasma per unit volume is

$$P_{dep}(s) = -\frac{\mathrm{d}P_{beam}(s)}{\mathrm{d}V} = -\frac{\mathrm{d}P_{beam}(s)}{\mathrm{d}s}\frac{\mathrm{d}s}{\mathrm{d}\rho}\frac{\mathrm{d}\rho}{\mathrm{d}V}, \quad (3.5)$$

Once the neutral beam particles entering the plasma have become ionized, the resulting fast ions are slowed down by Coulomb collisions. As the slowing down occurs energy is passed to the particles of the plasma, causing heating of both electrons and ions. In the developed model it is assumed that all the energy is deposited at the fluxsurface where the neutral particle becomes ionized and thus diffusion of the particles is neglected. ITER beam ions typically slow down in $t_s = 0.5$ seconds [8]. Assuming a diffusion coefficient $D = 0.1\mathrm{m}^2 \cdot \mathrm{s}^{-1}$ [8], yields that the beam ions can diffuse $x \approx 20$ cm before they are slowed down ($x = \sqrt{Dt_s}$). This is ten percent of the minor radius of ITER. The beam ions diffuse inwards and outwards in the plasma, resulting in a partial averaging-out of the effect.

At high injection velocity the electron heating is initially dominant. Then, as the beam ions slow down, the heating is transferred to the ions. From the Fokker-Planck theory an expression can be derived to calculate the overall heating fractions to the ions ϕ_i and electrons ϕ_e allowing for the time dependent energy of the beam ions [9]

$$\phi_e(x(E,s)) = 1 - \frac{1}{x}\left[\frac{1}{3}\ln\frac{1 - x^{1/2} + x}{(1 + x^{1/2})^2} + \frac{2}{\sqrt{3}}\left(\tan^{-1}\frac{2x^{1/2} - 1}{\sqrt{3}} + \frac{\pi}{6}\right)\right], \quad (3.6)$$

In this equation $x = \varepsilon_{bo}(E)/E_c(E,s)$, with $\varepsilon_{bo}(E) = 0.5m_b(E)v_b^2(E)$ the initial beam energy and $E_c(E,s)$ the critical beam energy at which the electron and ion heating rates are equal. The critical beam energy is [9]

$$E_c(E,s) = \left(\frac{3\sqrt{\pi}}{4}\right)^{2/3}\left(\frac{m_i}{m_e}\right)^{1/3}\frac{m_b}{m_i}T_e(s),$$

with m_i the mass of the plasma ions and m_b the mass of the beam ions.

Equation 3.6 has to be evaluated for the three different neutral beam particles. Combining Equation 3.5 and 3.6 yields the electron heating by the neutral beam per unit volume

$$\begin{aligned}
P_{NBI,e}(s) &= \phi_e(E,s)P_{dep}(s) \\
&= \frac{\mathrm{d}s}{\mathrm{d}\rho}\frac{\mathrm{d}\rho}{\mathrm{d}V}P_a n_e(s)\sum_{i=1}^{3}\phi_e(x(E/i,s))\sigma(E/i,Z_{eff})P_{frac,i}e^{-\int_{s=a}^{s}n_e(s)\sigma(E/i,Z_{eff})\,\mathrm{d}s}
\end{aligned} \quad (3.7)$$

3.1.2 Numerical implementation

Equation 3.7 gives the NBI plasma electron heating in function of the distance on the beamline, s, from the beam source. RAPTOR computes the electron temperature profile T_e and q profile versus the toroidal flux coordinate ρ. For coupling of the developed NBI code to RAPTOR it is required that the NBI electron heating is calculated in function of ρ. Obviously this requires information about the plasma fluxsurface geometry and beamline geometry (modeled in Appendix A.1): the intersection of the beamline with the fluxsurfaces determines which ρ coordinates are crossed and how often. To illustrate this the off-axis neutral beam system of ITER (Figure 3.1) is given as a specific example.
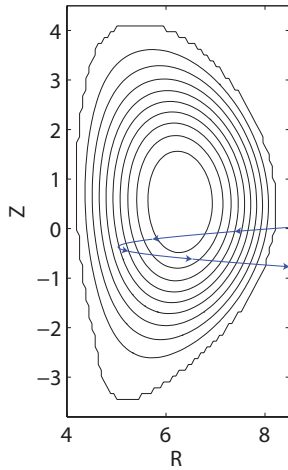

Figure 3.1: Reference equilibrium for ITER and the projection of the most off-axis NBI injection beamline in the poloidal plane.
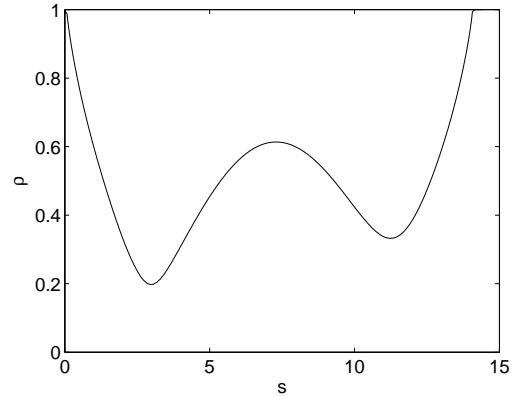
Figure 3.2: From the figure in the left hand panel the NBI code computes the evolution of the ρ coordinate over the beamline. $s = 0$ starts at the plasma edge.

The developed neutral beam code computes the NBI plasma electron heating in function of the coordinate s. Then a mapping is done from s to ρ space on the basis of the computed information shown in Figure 3.2. In this example $\rho = 0.4$ is crossed four times, so the NBI electron heating at the four corresponding s locations is added up. The information about $\frac{\mathrm{d}s}{\mathrm{d}\rho}$ can also be extracted from Figure 3.2. The information about the mapping from s to ρ space is stored in a matrix in the

14

code in order to make a fast projection from one coordinate space to the other. To date RAPTOR uses a fixed equilibrium assumption (see Chapter 2) which means this transformation matrix has to be calculated only once. An overview of the algorithm is given in Appendix A.2.

A key advantage of RAPTOR is that it uses analytical expressions for the gradients instead of finite differences making the code fast. To preserve this feature effort was made, as described in Appendix A.3, to calculate the analytical expressions for the derivatives of the NBI electron heating profile to the model parameters such as P_a or E. In Appendix A.4 a verification of these analytical expressions versus the finite difference approximation is shown.

3.2 Neutral beam current drive

3.2.1 Model

The current driven by the fast beam ions as they slow down by collisions on the plasma electrons and ions on each flux surface ρ can be derived from the uniform field solution to the Fokker-Planck equation for the fast ions [16]. This method does not take into account the possible trapping of the fast ions [12]

$$J_f(\rho) = e Z_b S(\rho) \tau_s \xi_b v_b I(y_c, \hat{Z}),$$
(3.8)

In Equation 3.8 e is the electron charge, Z_b is the charge number of the beam species and $v_b = \sqrt{2E_b/m_b}$ is the injection velocity of the neutral beam particles. S is the fast ion source rate per unit volume defined as

$$S = \frac{2P_{dep}(\rho)}{m_b v_b^2},$$

In this equation P_{dep} is the deposited beam power per unit volume defined by Equation 3.5.

In the equation for the fast ion current ξ_b is the initial pitch angle of the fast ions. A simple analytic expression, which tends to be valid for the outer flux surfaces of the plasma, is [13]

$$\xi_b \approx R_t/(R_0 + \rho),$$

where R_0 is the major radius of the plasma and R_t is the tangency major radius of the beam centerline.

In Equation 3.8 τ_s is the Spitzer slowing down time [17]

$$\tau_s = 6.27 \cdot 10^8 \frac{A_b T_e^{3/2}}{Z_b^2 n_e \ln \Lambda},$$

with $\ln \Lambda$ the Coulomb logarithm, which is typically around 17 in tokamak plasmas. A_b, Z_b are the atomic number and charge number of the injected ions, n_e is the electron density in cm^{-3} and T_e is the electron temperature in eV.

In Equation 3.8 the function $I(y_c, \hat{Z})$ has to be evaluated at each fluxsurface ρ

$$I(y_c, \hat{Z}(\rho)) = (1 + y_c^3)^{\hat{Z}/3} \int_0^1 \left[\frac{y^3}{y^3 + y_c^3} \right]^{\frac{\hat{Z}}{3}+1} dy,$$
(3.9)

$$\hat{Z} = \frac{\sum_i \ln(\Lambda_{bi}) n_i(\rho) Z_i^2/A_b}{\sum_i \ln(\Lambda_{bi}) n_i(\rho) Z_i^2/A_i},$$

$$\ln(\Lambda_{bi}) = 19.1 + \ln[A_i/(A_i + A_b)(T_e A_b E_b/n_{e20})^{1/2}],$$

with $y = v/v_b$, $y_c = v_c/v_b$, $v_c = \sqrt{2E_c/m_b}$, the mass numbers A_b and A_i of the beam particles and plasma bulk species respectively and charge numbers Z_b and Z_i.

The integral in Equation 3.9 has to be computed for each fluxsurface, because $\hat{Z}$ and y_c change on each fluxsurface. To increase the calculation speed of the beam code only the mean value of $\hat{Z}$ over the different fluxsurfaces is used for the computation of this integral, because the integral is a weak function on $\hat{Z}$. The value of y_c dominates the integral in the function $I(y_c, \hat{Z})$. To increase the calculation speed a fit of this integral was made for various values of y_c.

The fast ions injected by the neutral beam circulate around the torus. These fast ions get slowed down by collisions with the electrons inside the plasma. As a result the electrons circulate toroidally in the same direction as the beam ions producing a current that partially cancels the beam ion current. This is modified in turn, when neoclassical electron trapping effects are taken into account. The degree of cancelation depends on the charge, $Z_b e$, of the fast beam ions, the effective plasma charge, $Z_{eff} e$, and the number of trapped electrons. The net neutral beam driven current density, with the summation over the three energy components of the beam, is then

$$J_{NB}(\rho) = \left[1 - \frac{Z_b}{Z_{eff}}[1 - G(Z_{eff}, \epsilon)]\right] \sum_{i=1}^{3} J_{f_i}(\rho), \qquad (3.10)$$

where G is the neoclassical trapped electron correction factor approximated by Mikkelsen and Singer [14], which is in error by less than 1% for $1 \leq Z_{eff} \leq 3$ and $0 \leq \epsilon \leq 0.2$ [15]

$$G(Z_{eff}, \epsilon) \approx (1.55 + \frac{0.85}{Z_{eff}})\sqrt{\epsilon} - (0.20 + \frac{1.55}{Z_{eff}})\epsilon, \qquad (3.11)$$

with $\epsilon = \rho/R$.

3.2.2 Numerical implementation

The current drive profiles by fast ions $J_{f_i}(\rho)$ are needed to calculate the net neutral beam current drive $J_{NB}(\rho)$ using Equation 3.10. These profiles can easily be computed by Equation 3.8, because $P_{dep}(\rho)$ is readily available in ρ space from calculating the NBI electron heating profile. In Appendix A.3 the analytical expressions for the derivatives of the NBI current drive profile to its model parameters are shown. In Appendix A.4 a verification of these analytical expressions versus the finite difference approximation is shown.

3.3 Summary of the model

Table 3.1 summarizes the specifications of the developed NBI model. This table also gives an overview of the physics implementations of two other codes which will be used in Section 3.5 for a benchmark against the developed NBI model.

Table 3.1: Specifications multiple NBI codes

Specification	MODEL	ASTRA [5]	NEMO/SPOT [6]
Neutral beam representation	1D	3D	3D
Ionization cross section	Janev	Janev	ADAS
Fast ion solver	2D Fokker Planck (non-bounced averaged)	2D Fokker Planck (bounced averaged)	Monte Carlo
Diffusion	no	yes	yes
Loss	no	Separatrix	First wall
Ripple loss	no	First orbit	yes
Electron shielding model	Mikkelsen and Singer	Kim	Lin-Liu

The neutral beam is modeled as a single line in the model in contrast to all the other codes which consider the full 3D geometry of the beam. The ionization cross section used in NEMO/SPOT is

16

obtained from the ADAS database. The developed model and ASTRA code use Janev's fitting formula which takes the multistep ionization into account.

The fast ion solver simulates the slowing down of the beam ions. The NEMO/SPOT code uses a Monte Carlo simulation. The model and ASTRA code are based on the 2D Fokker Planck equation. ASTRA, in contrast with the model, uses the bounced averaged Fokker Planck theory in order to include orbit effects.

All the codes mentioned in the table, except the developed model, calculate the diffusion of the neutral beam particles once they get ionized. The model assumes the neutral beam particles are deposited locally disregarding the diffusion of the particles.

The model assumes no loss of beam particles. NEMO/SPOT models the loss of beam particles to the first wall. ASTRA judges a new born fast ion is immediately lost if the first orbit crosses the separatrix.

A toroidal field ripple affects the transport of the beam ions in two ways. The particles can be trapped in a magnetic well created by the ripple or diffused away due to stochastic banana diffusion [18].

The electron shielding model (Mikkelsen and Singer) used in the model is an approximation of the Start and Cordey model. The latter can be used for all aspect ratios. The different models of the electron shielding all take into account the trapped banana electrons which disturb the motion of circulating electrons and hence the electron current.

3.4 Benchmark of the lightweight model for NBI electron heating and current drive

In this section the results of the benchmark to check the model's calculation of the neutral beam electron heating and current drive are presented. In order to calculate these two quantities the neutral beam power deposition profile needs to be calculated. Firstly a benchmark of the model against ALCBEAM [19], a NBI simulation code developed for ALCATOR C-MOD, is performed to check the calculation of the neutral beam power deposition profile. Then the model is compared with two other codes (ASTRA and NEMO/SPOT) to benchmark the calculation of the neutral beam electron heating and current drive.

Benchmark of the power deposition profile

Figure 3.3 depicts the setup used for the benchmark of the power deposition profile calculated by ALCBEAM and the model. This configuration simplifies the beam attenuation calculation of the model, because the ρ coordinate corresponds with the radial tokamak coordinate through a linear mapping. For this benchmark the full, second and third energy components of the neutral beam are modeled.
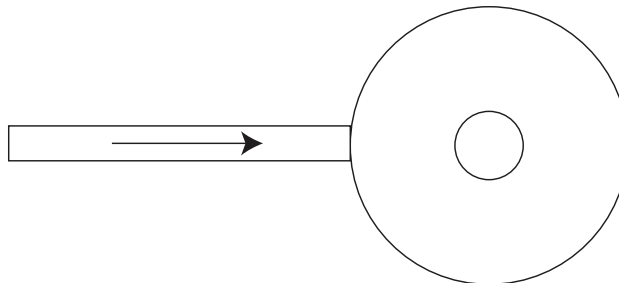

Figure 3.3: Top view of the neutral beam configuration used for the benchmark of the model with ALCBEAM. The neutral beam lies in the plane of paper.

Figure 3.4 shows the beam power inside the tokamak versus the major radius. The beam attenuation calculated by the model and ALCBEAM are in good agreement.
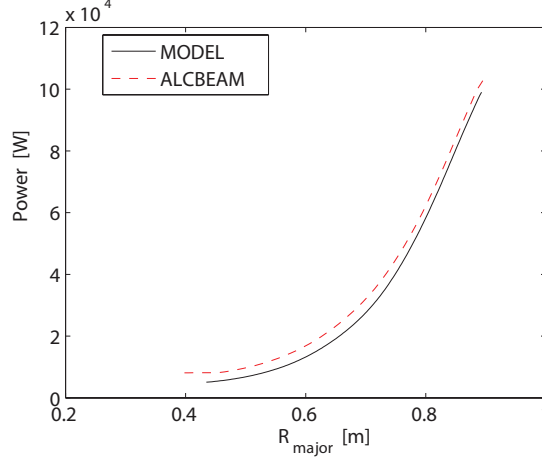

Figure 3.4: The beam power versus the major radius.

The beam power profile is used by the model to calculate the beam power deposition inside the tokamak. Figure 3.5 shows the beam power deposition profile $(\frac{\mathrm{d}P_{beam}(s)}{\mathrm{d}s})$ calculated by ALCBEAM and the model. The beamline crosses each fluxsurface twice in the configuration used in the benchmark. The profiles calculated by the model and ALCBEAM are in good agreement.
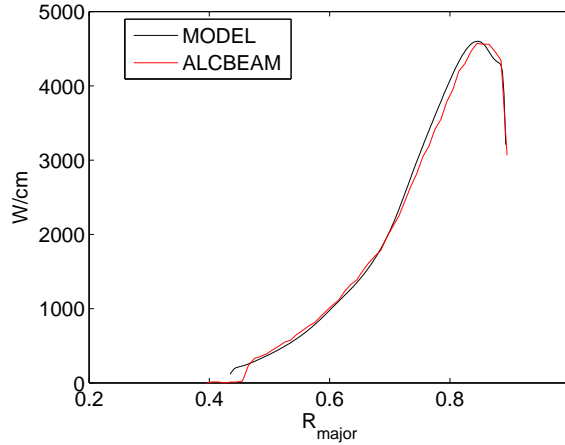

Figure 3.5: The beam power deposition [W/cm] versus the major radius.

Benchmark of the neutral beam electron heating and current drive

The benchmark of the model against ALCBEAM shows the calculation of the beam power deposition profile is reliable. In this section the results of a benchmark of the neutral beam electron heating and current drive calculated by the model and two other codes (ASTRA and NEMO/SPOT) are presented. This benchmark is based on an ITER-like scenario. Only the full energy component of the beam was simulated. This because the second and third energy components are calculated with the same equations and a benchmark of only one energy component will allow for

a clean comparison, because no mixing of errors of the first, second and third energy components will occur. The results of the ASTRA and NEMO/SPOT code were obtained from a case study performed for ITER [20]. Figure 3.6 depicts the electron temperature and density profiles that were used in the simulation. These two profiles together with the NBI parameters shown in Table 3.2 and the magnetic equilibrium shown in Figure 3.1 are the inputs for the developed model for the benchmark.
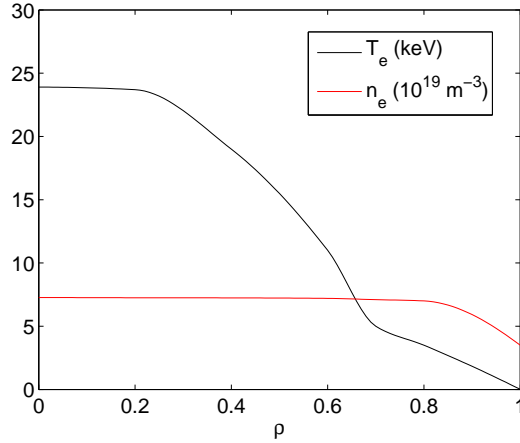

Figure 3.6: The profiles of the electron temperature and density.

Table 3.2: Parameters used in the benchmark

species	Deuterium
energy of the beam E_b	1 MeV
injection power	33 MW
Z_{eff}	2.17
$E_b : E_b/2 : E_b/3$	1:0:0

Figure 3.7 depicts the neutral beam power transferred to the electrons. It shows the three codes yield slightly different results with exceptions of the region close to $\rho = 0.2$ where the developed code peaks and differs significantly from the two other codes. The results of the model lie close within the solution space of the two more advanced codes. Figure 3.8 shows the neutral beam current drive calculated by the model and the two other codes. The result of the three codes are very similar with exception of again the region close around $\rho = 0.2$. The peaking of profiles is a result of the pencil beam approach. It vanishes for a finite beam [21]. In Appendix A.5 an comprehensive explanation is given.
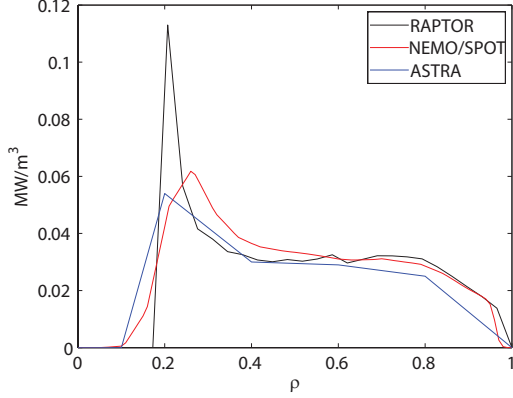
Figure 3.7: The beam power to the electrons versus ρ calculated by the developed model, ASTRA and NEMO/SPOT.
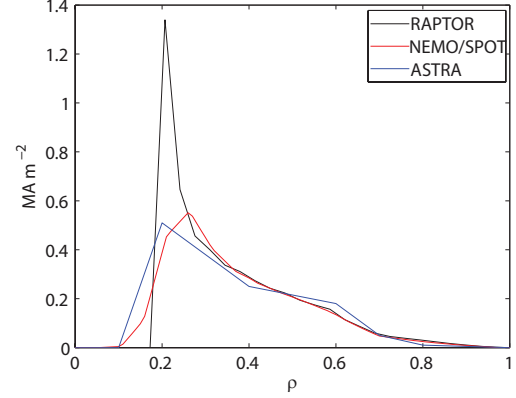

Figure 3.8: The neutral beam current drive versus ρ calculated by the developed model, ASTRA and NEMO/SPOT.

In Figure 3.9 the integrated power density deposition profile over the plasma volume is shown for various number of ρ gridpoints. The total power deposited is nearly insensitive to the number of gridpoints and converges, as required, to the input power of 33 MW.
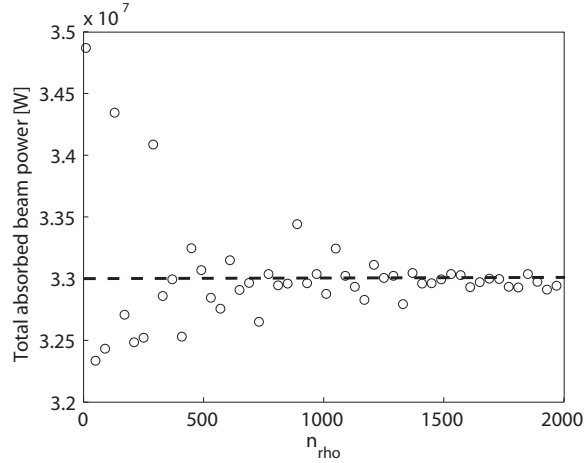

Figure 3.9: The integrated power deposition profile [W/m^3] over the plasma volume for various number of ρ gridpoints.

The occurrence of the singularity at $\rho = 0.2$ was removed by applying a smoothing algorithm on the calculated NBI electron heating profile. The peaked power to the electrons was smeared out over the user specified region of $0.1 \leq \rho \leq 0.2$. In this way the diffusion and finite beam width effects in this region are crudely modeled. The smoothing algorithm uses a half normal distribution and has as constraint that the total integrated power in this region must remain unchanged: the smoothing algorithm can not add or remove energy, but only redistribute it. In Figure 3.10 the smoothing function is plotted. It has unit $[W/m^3]$ and the integrated power $[W]$ of this function is one. The power is redistributed by multiplying the half normal distribution with the total integrated power in the region $0.1 \leq \rho \leq 0.2$. The developed NBI module can only smooth one peak, in the future the option should be added to smear out several peaks in the NBI electron heating profile. In Figures 3.11 and 3.12 the results of the benchmark are shown again, this time with the smoothing algorithm enabled.
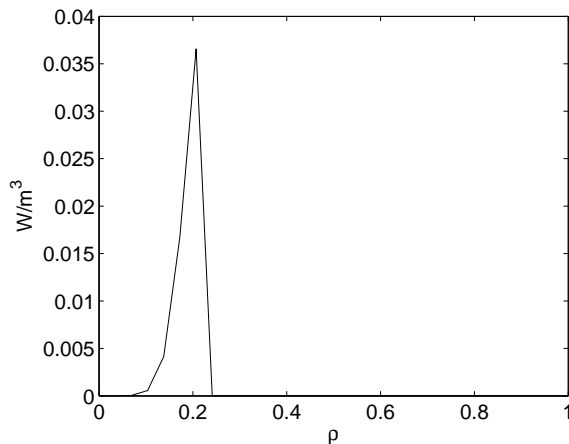
Figure 3.10: The half normal distribution that is used to smooth the NBI electron heating and current drive profiles [W/m^3] in the region of $0.1 \leq \rho \leq 0.2$.
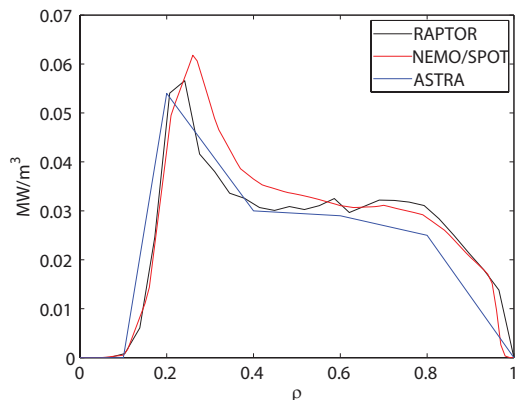

Figure 3.11: The beam power to the electrons versus ρ calculated by the developed model, ASTRA and NEMO/SPOT. In the developed NBI model the smoothing algorithm was enabled, which is in a sense modeling the diffusion of the beam ions in the region where the smoothing is applied.
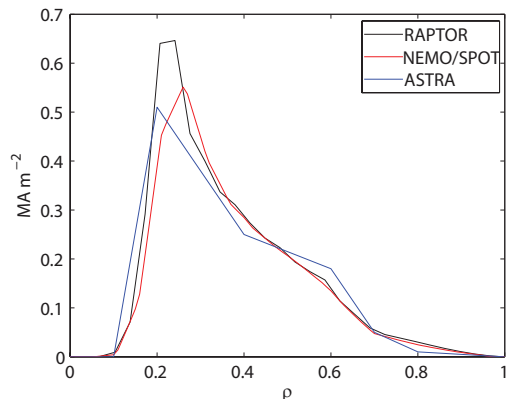

Figure 3.12: The neutral beam current drive versus ρ calculated by the developed model, ASTRA and NEMO/SPOT. In the developed NBI model the smoothing algorithm was enabled. The maximum value of the current drive profile predicted by the developed model is greater than the one calculated by ASTRA and NEMO/SPOT. The maximum varies significantly between different NBI codes. The maximum predicted by OFMC is 0.75 MA m^{-2} (published in [20]). The developed code result lies within the solution space of the various codes.

To increase confidence in the developed NBI code, effort was payed to perform more benchmarks. The NEMO/SPOT code was used to generate four different NBI scenarios which were used to benchmark the developed NBI code against. In Appendix A.6 the results are reported. These four benchmarks together with the benchmark presented in this chapter give great confidence that the developed NBI code is able to predict NBI electron heating and current drive accurately. It should be noted that the developed NBI code overestimates the current drive for the benchmark

depicted in Figure A.18. This could be caused by the high value of Z_{eff} that was used for this benchmark. The neoclassical trapped electron correction factor G (See Equation 3.11) may not be valid anymore in this Z_{eff} regime. Further research should be done to explain the overestimation of the current drive for the specific benchmark.

An important design criterion for the NBI module was that it should calculate the NBI electron heating and current drive fast, so it will not slow down the RAPTOR calculations. On Genuine Intel 1.83GHz CPU (2006) the NBI module is able to calculate the two profiles in 4 milliseconds when using 21 gridpoints. To put this number in perspective: a similar NBI run in the NEMO/SPOT code takes around 17 seconds on a 3 GHz Intel(R) Xeon(R) CPU E5450 processor [22]. It must be noted that for the typical runtime of the developed NBI module, the time to calculate the transformation matrix that determines which ρ coordinates are crossed by the beamline is excluded. This because this matrix has to be calculated only once, after this initialization step the same matrix can be used during the entire shot simulation of the NBI, thanks to the fixed equilibrium assumption in RAPTOR. Finally a typical run of an ohmic shot in RAPTOR takes 0.0465 seconds on a Genuine Intel 1.83GHz CPU when using 21 gridpoints. The information is graphically summarized in Figure 3.13.
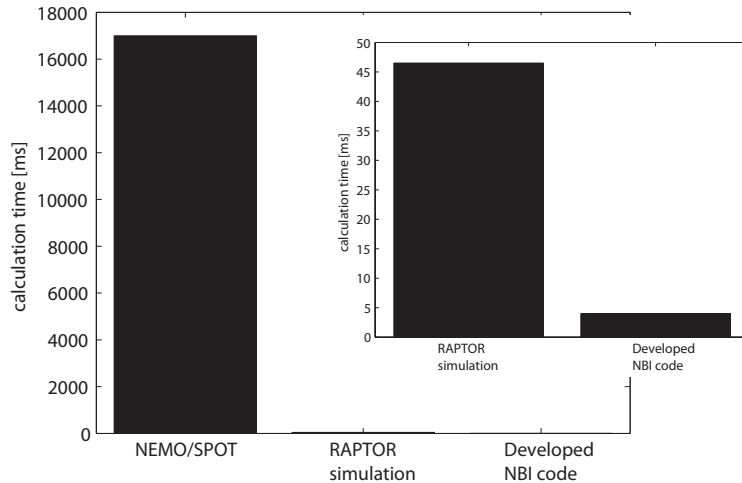

Figure 3.13: The typical run times of the NBI code NEMO/SPOT, an ohmic shot in RAPTOR and the developed NBI code.

3.5   Conclusions

The Neutral Beam Injection (NBI) system is an important external heating and current drive actuator to alter the q-profile of a fusion plasma. It is used at many existing tokamaks and will be an important actuator for ITER.

A NBI code was developed for the RAPTOR code which can predict the neutral beam electron heating and current drive. There were two design criteria for the code:

1. The code had to be sufficiently fast to run very rapidly in order to not slow down RAPTOR;

2. The code had to be sufficiently complex to contain the most important physics.

The two design criteria were met. The developed fast Neutral Beam Injection module, based on a pencil beam approach, produces results similar to more complete beam codes for an ITER-like scenario. The execution time of the developed NBI code is approximately ten percent of the execution time of RAPTOR.

Chapter 4

Adaptations to the electrical conductivity σ and heat diffusivity χ_e ad-hoc model

4.1 Introduction

In this section the ad-hoc model for the electron heat diffusivity χ_e and the model for the neo-classical electrical conductivity σ which are presently used in RAPTOR are discussed.

The expression for the ad-hoc model of χ_e, which includes the anomalous diffusion and the q profile dependent confinement, reads

$$\chi_e = \chi_{neo} + c_{ano}\rho q F(s) + \chi_{central} e^{\rho^2/\delta_0^2}, \tag{4.1}$$

In this equation χ_{neo} is a small constant representing neoclassical diffusion. The much larger anomalous diffusion is captured by c_{ano}, and the presence of q in the anomalous diffusion term accounts for increased confinement at higher plasma currents I_p, because transport is then suppressed. The term $F(s)$ is a shear-dependent function to include the effect of improved confinement (ic) at low and negative magnetic shear.

This effect makes the advanced scenarios, as shortly introduced in the introduction of this thesis, possible. The expression for the function $F(s)$ (see Figure 4.1) is

$$F(s) = \frac{a_{ic}}{1 + \exp[w_{ic}(d_{ic} - s)]} + (1 - a_{ic}), \tag{4.2}$$

The term a_{ic} accounts for the amount of reduction of transport, d_{ic} is the level of the shear at which the transition takes place. The sharpness of the transition is governed by the term w_{ic}.

In the electron heat diffusivity equation 4.1, the term containing $\chi_{central}$ is an ad-hoc term representing a local confinement decrease at the center of the plasma, used to model the experimental observation that the T_e profile is relatively flat near the center.
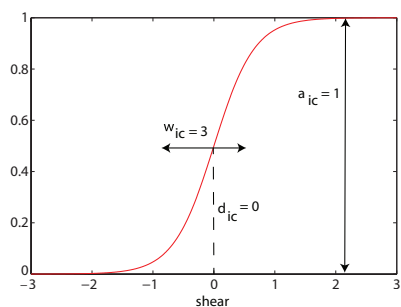

Figure 4.1: Shear-dependent function $F(s)$.

The neoclassical electrical conductivity formula presently used in RAPTOR reads

$$\sigma_{\parallel} = c_{neo}(\rho)\sigma_{Spitzer}(T_e(\rho, t)) \propto c_{neo}(\rho)T_e[eV]^{3/2}, \tag{4.3}$$

Two physical mechanisms were added to the ad-hoc χ_e model during this work: the global effect of sawtooth crashes occurring in the center of the plasma and the nonlinear effect of confinement

deterioration with increasing temperature gradient.

The neoclassical electrical conductivity model $\sigma_{\parallel}$ was extended to include the sawtooth behavior. More information about the two physical mechanisms is given before presenting the modified models.

- The sawtooth crash is an internal magnetohydrodynamic MHD reconnection event that repeatedly mixes plasma from the core and outer regions of tokamaks, cools and flattens the central temperature profile and redistributes the current by magnetic reconnection. The instability occurs in the region where the safety factor q is below unity [23]. The periodic character of the sawtooth crash and hence its name can be understood as follows: In a tokamak plasma the temperature, and therefore the current density, is peaked in the center. As soon as the current density in the center reaches a certain level, the safety factor q drops below unity and a sawtooth crash occurs. After the occurrence of this instability q is again at or above one. Now the process starts over, the temperature profile peaks and hence the current density profile until q drops below unity and the instability resets the profiles again. The periodic increase of the temperature followed by a sharp decrease plotted versus time looks like the teeth of a saw;

- Confinement deterioration is observed when temperature gradients are increased, due to a multitude of effects including 3D turbulence [24].

4.2 Modified models for the electrical conductivity σ and heat diffusivity χ_e

To include the two described complex physical mechanisms, the choice was made not to use (first principle) physics models as it would slow down RAPTOR significantly. This level of accuracy is also not required, because RAPTOR already computes an approximate solution due to the used simplifications and approximations. Instead, the global effect of the sawtooth behavior on the electrical conductivity and heat diffusivity equations was modeled as well as a global scaling effect of the thermal confinement deterioration with increasing temperature.

The modified model for the heat diffusivity is

$$\chi_e = \chi_{neo} + c_{\chi saw}G(q) + c_{ano}\rho q F(s)\left(\frac{T_{e_0}[eV]}{1000}\right)^{c_{T_e}} + \chi_{central}e^{\rho^2/\delta_0^2}, \tag{4.4}$$

In this equation the part in black was the original heat diffusivity equation, the two terms in red were added to include on the one hand sawtooth crashes and on the other hand the confinement deterioration with increasing temperature and temperature gradient . The latter physical process is represented by the red term with the c_{T_e} coefficient. The numerator T_{e_0} is the electron temperature in the core of the plasma, making the total term dimensionless.

The sawtooth crashes, which are responsible for lower heat confinement in the core of the plasma, are modeled by the second term in the χ_e equation. The term $G(q)$ is a q profile dependent function

$$G(q) = \frac{1}{1 + \exp[w_{\chi saw}(q - 0.95)]}, \tag{4.5}$$

For q values smaller and around 0.95 the plasma exhibits sawtooth behavior and the $G(q)$ function is nonzero. In this regime the heat conductivity is enhanced by the $c_{\chi saw}G(q)$ term to mimic lower confinement. The sharpness of the transition around q equals 0.95 is determined by $w_{\chi saw}$. Note that by assuming constant values for $w_{\chi saw}$
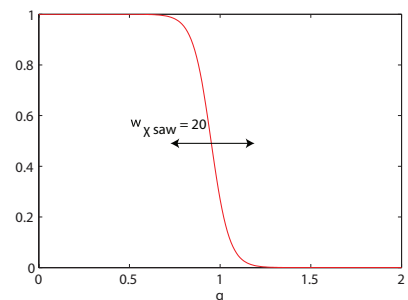

Figure 4.2: Function $G(q)$.

and $c_{\chi saw}$ a "time-averaged" effect of the sawteeth is modeled.

The neoclassical electrical conductivity formula in RAPTOR was extended by the red sawtooth term.

$$\sigma_{\parallel} = c_{neo}(\rho)\ W(q)\ \sigma_{Spitzer}(T_e), \tag{4.6}$$

A sawtooth crash redistributes the current by magnetic reconnection. As a result the current density profile is flattened after a sawtooth crash.

To push enough current to the edge of the plasma after a sawtooth crash, the electrical conductivity is reduced in the center of the plasma by multiplication with $W(q)$. This function (see Figure 4.2) reads

$$W(q) = \frac{c_{\sigma saw}}{1 + \exp[w_{\sigma saw}(0.95 - q)]} + (1 - c_{\sigma saw}),$$

In this equation $w_{\sigma saw}$ represents the sharpness of the transition around q equals 0.95, the term $0 \leq c_{\sigma saw} \leq 1$ accounts for the amount of reduction of the electrical conductivity. Note that by assuming constant values for $w_{\sigma saw}$ and $c_{\sigma saw}$ a "time-averaged" effect of the sawteeth is modeled.
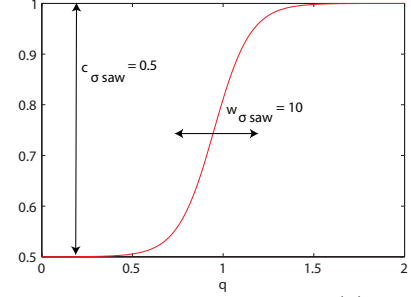

Figure 4.3: Function $W(q)$.

4.3 Determination of the model parameters

The neoclassical electrical conductivity and heat diffusivity can be calculated with first principle physics models. The results could be used to tune the ten model coefficients of χ_e in RAPTOR.

$$\chi_{neo},\ c_{\chi saw},\ w_{\chi saw},\ c_{ano},\ \chi_{central},\ \delta_0,\ a_{ic},\ w_{ic},\ d_{ic} \text{ and } c_{T_e},$$

and the two $\sigma_{\parallel}$ model parameters

$$c_{\sigma saw} \text{ and } w_{\sigma saw},$$

This approach is time consuming and not desired because the aim of RAPTOR is to make reliable T_e and ι predictions. Due to all the simplifications and assumptions, systematic errors in the calculated T_e and ι profiles can be captured in the model parameters of the χ_e and $\sigma_{\parallel}$ models. This could result in χ_e and $\sigma_{\parallel}$ profiles that differ from the first principle calculations, but T_e and ι profiles that agree with experimental evidence.

The model parameters are presently tuned by hand to yield reasonable q and T_e profiles that match experimental observations. During this research a method was developed to estimate in a generic way the model coefficients to quantitatively reproduce existing experiments. More details can be found in Chapter 5.

Chapter 5

Estimation of the model parameters in the RAPTOR code

5.1 Introduction

RAPTOR uses an ad-hoc model to describe the heat diffusivity χ_e (see Equation 4.1) and a sawteeth correction term in the electrical conductivity $\sigma_\parallel$ equation (see Equation 4.6). In this chapter a generic method is presented which estimates the optimal χ_e and $\sigma_\parallel$ model parameters in order to quantitatively match RAPTOR with measurements or results from more complete codes. The chapter starts with the theory of parameter estimation for dynamical systems, followed by a explanation of the used method. Before presenting the results of the parameter estimation for RAPTOR at the TCV tokamak in Lausanne, a demonstration of the algorithm is given.

5.2 Theory

5.2.1 Nonlinear Least Squares

Let y_k be a set of measurements, at given times k, of profiles of a dynamical system excited with inputs trace $u(t)$ and let $\hat{y}_k(p)$ be the simulated measurements obtained by simulating a nonlinear model with parameter set p. The difference between the measured and simulated values can be defined as the residual

$$r_k(p) = y_k - \hat{y}_k(p), \tag{5.1}$$

The problem of determining the model parameters p can be formulated as the minimization of the cost function

$$J(p) = \sum_k \|r_k^2(p)\|_1, \tag{5.2}$$

where the 1-norm is taken over the radial grid at time k. A local minimum $dJ/dp = 0$ can be found by gradient descent. The cost function, in literature also known as the objective function, is often weighted because [27]:

- The measured quantities may have different physical dimensions, or may be measured on different scales. For example, some of the measurements in the measurement vector y_k may represent voltages, falling into the range zero to hundred. Other measurements, however, may be temperature measured in electronvolt with values in a much higher range. Without weighting, the cost function will be dominated by the temperature residuals, and only the model parameters p which minimize this residual and not the voltage residual are found;

- Some measurements may be known to be less reliable than others. Thus, weighting is needed to make sure that the parameter estimates are less influenced by these measurements relative to the more accurate ones.

The weighted objective function is

$$J(p) = \sum_k \|\nu_k r_k^2(p)\|_1 \tag{5.3}$$

5.2.2 Statistical Background

Let $\hat{p}$ denote the estimated parameter vector. To investigate the reliability and precision of the estimated model parameters one needs to compute the covariance matrix for the parameters. This matrix can be approximated as follows [27]

$$\text{cov}(\hat{p}) = C \approx 2\sigma^2 \left(H(\hat{p}) \right)^{-1}, \tag{5.4}$$

in which $H(\hat{p}) = \partial^2 J/\partial p^2$ denotes the Hessian matrix of the cost function evaluated at $\hat{p}$. The standard deviations of the measurements errors σ can be estimated from the residuals, assuming that the measurement errors are independent and normally distributed with expected value 0 [27]

$$\sigma^2 = \frac{1}{n_k - n_p} \sum_k \|\nu_k r_k^2(\hat{p})\|_1 = \frac{1}{k - n_p} J(\hat{p}), \tag{5.5}$$

with n_p the number of model parameters and n_k the number of measurements.
The diagonal elements of the covariance matrix contain the variance of the parameters $\hat{p}$

$$\text{var}(\hat{p}_i) = C_{ii}, \tag{5.6}$$

The off-diagonal elements give information about the covariance between the parameters. The Correlation Matrix R, with elements R_{ij}, can be computed from the Covariance Matrix C

$$R_{ij} = \frac{C_{ij}}{\sqrt{C_{ii}C_{jj}}}, \tag{5.7}$$

A $100(1-\alpha)\%$ marginal confidence interval for the ith parameter is given by [27]:

$$\hat{p} \pm t_{k-n_p}^{\alpha/2} \sqrt{\text{var}(\hat{p}_i)}, \tag{5.8}$$

in which $t_{k-n_p}^{\alpha/2}$ denotes a quantile of the t-distribution with $k - n_p$ degrees of freedom. The relative $100(1-\alpha)\%$ marginal confidence interval for the ith parameter is

$$1 \pm \frac{t_{k-n_p}^{\alpha/2} \sqrt{\text{var}(\hat{p}_i)}}{\hat{p}}, \tag{5.9}$$

The confidence interval should be interpreted as follows: there is a $100(1-\alpha)\%$ probability that the calculated confidence intervals will contain the true parameters p. This is different from the statement that there is a $100(1-\alpha)\%$ probability that the true parameters are in the confidence intervals.

5.2.3 Parameter Identifiability

Model identifiability is the problem of determining whether the parameters of a given mathematical model can be uniquely recovered from data. The parameter estimation problem raises the two following questions which are closely related:

- Identifiability of the parameterized model, i.e., the question whether there are two distinct choices of the unknown parameters p that produce the same input-output relationship. A mathematical model is said to be identifiable at $\hat{p}$ if there exists an input signal u^* such that $\hat{y}(\hat{p}, u^*) = \hat{y}(p, u^*) \rightarrow \hat{p} = p$. If such u^* does not exist, the model is said to be fundamentally unidentifiable at that choice of parameters;

- Richness of the input, i.e., the problem of generating an input such that the above relation holds. Such an input u^*, if it exists, is called persistently exciting with respect to mathematical model at $\hat{p}$.

Identifiability properties are global properties holding for the full parameter space. However, for highly nonlinear systems restricting attention to a local analysis is often the only situation that is feasible in terms of computational complexity [25]. Only the question about local identifiability is addressed in this thesis. The unknown parameters p of a mathematical model are locally identifiable from data corresponding to given an input u if

$$\hat{y}(\hat{p}, u) = \hat{y}(p, u) \rightarrow \hat{p} = p, \tag{5.10}$$

Note that this identifiability condition applies to a given experiment defined by a fixed input. It is therefore equivalent to the question whether the given input u is persistently exciting at $\hat{p}$. The necessary condition for $\hat{p}$ being an isolated minimum of the cost function J is that the Hessian is positive definite at the solution $\hat{p}$. This is equivalent to requiring that the Hessian matrix has full rank. This rank test can be performed by applying the Singular Value Decomposition (SVD):

$$H(\hat{p}) = \frac{\partial^2 J}{\partial p^2} = U\Sigma V^T, \tag{5.11}$$

In this equation Σ contains the singular values, and the columns of U are basis functions in the parameter space determining the linear combinations of the original parameters that will be identifiable from the measurements. When Σ contains one or more singular values significantly smaller than the rest the Singular Value Decomposition can be formulated as

$$H(\hat{p}) = \begin{bmatrix} U_1 \ U_2 \end{bmatrix} \begin{bmatrix} \Sigma_1 & 0 \\ 0 & \Sigma_2 \end{bmatrix} \begin{bmatrix} V_1^T \\ V_2^T \end{bmatrix}, \tag{5.12}$$

where the singular values in Σ_2 are considerably smaller than those in Σ_1. The columns U_2 contain (combinations of) parameters which are poorly identifiable.

A quantitative measure of the parameter identifiability can be obtained by analyzing the width of the confidence intervals (Equation 5.8) of the estimated parameter set. A large confidence interval for an estimated parameter $\hat{p}$ means that the cost function J does not vary much when this parameter is perturbed. This allows for a quantitative measure of the identifiability of the parameters. Finally, the correlation between parameters, obtained from R (Equation 5.7), indicates that insufficient information is available in the data to estimate the model parameters uniquely, hence that either the model structure should be reconsidered or further experiments with different input sequence performed.

5.2.4 Parameter scaling in identifiability

Scaling of the model parameters is important for proper convergence in nonlinear optimization and for the Singular Value Decomposition of the Hessian. If parameters have vastly different magnitudes, then the singular values are not directly comparable [27]. To overcome this problem, the relative variance of parameters is used in the nonlinear least squares optimization [25]

$$\bar{p} = \Gamma^{-1} p, \tag{5.13}$$

where $\Gamma^{-1} = \text{diag}(|p_1|, ..., |p_n|)$

This parameter scaling results in a scaled Hessian [25]

$$H(\bar{p}) = \Gamma \frac{\partial^2 J}{\partial p^2} \Gamma = \Gamma H(p) \Gamma, \tag{5.14}$$

The singular value decomposition of the scaled Hessian yields singular values that are directly comparable. This makes a proper analysis of the parameter space that is identifiable possible.

A scaled Hessian yields a scaled Covariance matrix, and hence a scaled variance

$$\text{var}(\bar{p}) = \text{var}(\Gamma^{-1} p), \tag{5.15}$$

The statistical analysis presented in Section 5.2.2 can still be applied using the scaled parameters $\bar{p}$. To transform the variance of the scaled model parameters to the variance of the "real" parameters, the following relation holds

$$\text{var}(\bar{p}) = \text{var}(\Gamma^{-1} p) = \Gamma^{-2} \text{var}(p) \rightarrow \text{var}(p) = \Gamma^2 \text{var}(\bar{p}), \tag{5.16}$$

When using scaled parameters in the nonlinear least squares optimization, the $100(1 - \alpha)\%$ marginal confidence interval for the ith unscaled parameter can still be computed after using the transformation presented in Equation 5.16.

5.3   Implementation

5.3.1   Definition of the cost function

The cost function J for model parameter estimation of RAPTOR is defined such that the calculated radial $T_e(\rho)$ and $\iota(\rho)$ profiles match the measurements. The loop voltage $U_{pl}(\rho)$ at the final time k, which can be measured fairly accurately, was also included to this cost function as a constraint to the parameter estimation problem. In this work a constant weighting ν was chosen such that the contribution of U_{pl} [V] ($\mathcal{O}(1-10)$), T_e [eV] ($\mathcal{O}(1000)$) and ι [-] ($\mathcal{O}(1)$) is of the same order and that only the more reliable measurements in the ρ region between 0.1 and 0.9 were used. Lastly, also parameter scaling was applied with Γ^{-1} containing the initial guess of the model parameters. The cost function defined in Equation 5.3 becomes

$$J(\bar{p}) = \sum_{k=1}^{n_k} \|\nu_{T_e} r_{T_e,k}^2(\bar{p})\|_1 + \sum_{k=1}^{n_k} \|\nu_\iota r_{\iota,k}^2(\bar{p})\|_1 + \|\nu_{U_{pl}} r_{U_{pl},n_k}^2(\bar{p})\|_1 = \nu_{T_e} J_{T_e} + \nu_\iota J_\iota + \nu_{U_{pl}} J_{U_{pl}}, \tag{5.17}$$

the weighting factors that will be used in this thesis are defined as follows

$$\nu_{T_e} = \begin{cases} 0 & \text{if } \rho < 0.1 \ \lor \ \rho > 0.9, \\ \frac{1}{1000 n_k} & \text{if } 0.1 \leq \rho \leq 0.9. \end{cases}$$

$$\nu_\iota = \begin{cases} 0 & \text{if } \rho < 0.1 \ \lor \ \rho > 0.9, \\ \frac{1}{n_k} & \text{if } 0.1 \leq \rho \leq 0.9. \end{cases}$$

$$\nu_{U_{pl}} = \begin{cases} 0 & \text{if } \rho < 0.1 \ \lor \ \rho > 0.9, \\ \frac{1}{10} & \text{if } 0.1 \leq \rho \leq 0.9. \end{cases}$$

The optimal model parameters in RAPTOR to describe a dataset containing the U_{pl}, T_e and ι radial profiles evolving in time can now be estimated by minimizing the cost function in Equation 5.17. An additional feature was added to find the optimal model parameters for multiple datasets, n_d, at once. For this purpose the cost function definition is

$$J(\bar{p}) = \sum_{n_d} \nu_{T_e} J_{T_e} + \nu_\iota J_\iota + \nu_{U_{pl}} J_{U_{pl}}, \tag{5.18}$$

where n_d is the number of datasets.

5.3.2 Overview of the parameter estimation algorithm

In Figure 5.1 the flow diagram of the developed algorithm to estimate the model parameters is shown. To start the parameter optimization routine, an initial guess of the model parameters p must be specified. The user can choose to optimize the (sub)set of ten χ_e model parameters in Equation 4.4

$$\chi_{neo}, \ c_{\chi saw}, \ w_{\chi saw}, \ c_{ano}, \ \chi_{central}, \ \delta_0, \ a_{ic}, \ w_{ic}, \ d_{ic} \text{ and } c_{T_e},$$

and/or the (sub)set of two $\sigma_\parallel$ model parameters in Equation 4.6

$$c_{\sigma saw} \text{ and } w_{\sigma saw},$$

RAPTOR uses the initial guess of the model parameters to solve the nonlinear poloidal flux diffusion equation and nonlinear electron energy transport equation to obtain the state vector $x(t)$, defined in Equation 2.11. This state vector is used to compute the profiles $T_e(\rho)$, $\iota(\rho)$ and U_{pl} (see Equation 2.13). The model predictions are compared to measured data by computing the cost function J. The cost function, is minimized with an optimization routine. The Sequential Quadratic Programming (SQP) algorithm [26], which is readily available in MATLAB, was used for this purpose. The SQP algorithm finds the minimum of the cost function by changing the model parameters p. If the objective function is not at its minimum the algorithm computes a new set of parameters p for which the cost function is expected to be lower. When the objective function is in its minimum the optimal parameters are found for which the ι, U_{pl} and T_e profiles of RAPTOR match the experimental data best.
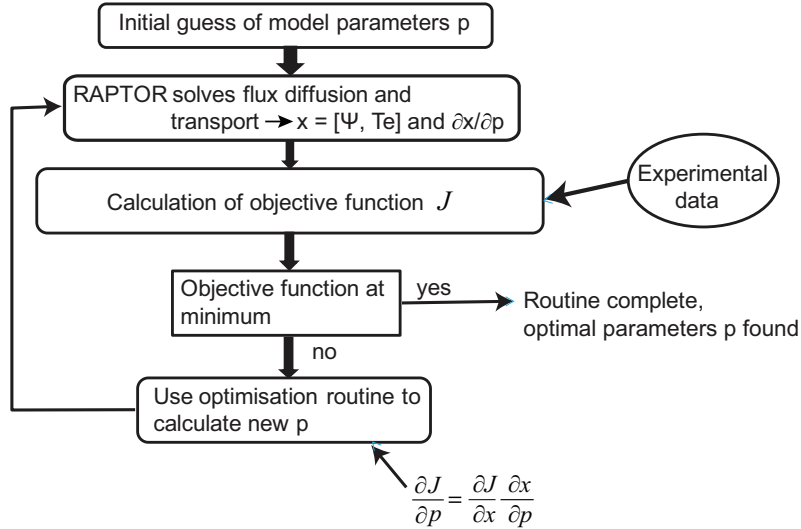

Figure 5.1: Algorithm to estimate model parameters. The cost function gradient dJ/dp is computed analytically using the ψ and T_e profiles sensitivities, dx/dp. More information is given in Section 5.3.3.

5.3.3 Computation of the cost function gradient

The performance of the Sequential Quadratic Programming algorithm critically depends on the derivative of the cost function to the model parameters dJ/dp. This cost function gradient gives information about in which direction in parameter space the cost function decreases. The choice was made to describe dJ/dp analytically. This has two major advantages. The first one is that the SQP algorithm converges faster to the optimal model parameters because no finite difference

approximation is needed to approximate the derivative of the cost function to the model parameters. The second advantage is that the analytical solution is exact in contrast with the numerical approximation, which enhances the performance of the SQP algorithm. The analytical expression for $\mathrm{d}J/\mathrm{d}p$ is computed as follows

$$\frac{\mathrm{d}J}{\mathrm{d}p} = \frac{\partial J}{\partial x}\frac{\partial x}{\partial p}$$

The term $\partial J/\partial x$ can easily be obtained from direct differentiation of the cost function. The term $\partial x/\partial p$ is obtained from the forward sensitivity equation.

To obtain the state vector x, RAPTOR solves Equation 2.12 (which contains the flux diffusion equation and electron energy transport) at discrete-time points k [3]

$$f_k = f(x_{k+1}, x_k, u_k) = 0 \quad \forall k$$

Differentiating this equation to a vector of model parameters p results in the forward sensitivity equation

$$0 = \frac{df_k}{dp} = \frac{\partial f_k}{\partial x_{k+1}}\frac{\partial x_{k+1}}{\partial p} + \frac{\partial f_k}{\partial x_k}\frac{\partial x_k}{\partial p} + \frac{\partial f_k}{\partial u_k}\frac{\partial u_k}{\partial p} + \frac{\partial f_k}{\partial p} \tag{5.19}$$

This equation is recursively solved starting from the initial condition $\partial x_0/\partial p$, yielding $\partial x_k/\partial p$, for $k \in [1, ..., n_k]$. Below, more details about the terms in the forward sensitivity equation are given

- The first two terms on the right hand side contain the Jacobians $\partial f_k/\partial x_{k+1}$ and $\partial f_k/\partial x_k$. These are already computed by RAPTOR [3];

- The third term depends on the model parameters of the input actuators. In our case where only the model parameters in χ_e and σ are optimized, this term is equal to zero;

- The last term is nonzero for model parameters, i.e. parameters that affect the model directly by altering the equations. In our case the parameters in χ_e and σ are model parameters. Presently the term $\partial f_k/\partial p$ was not computed in RAPTOR, because the code was not used for model parameter estimation yet. During this research the term was added to the code. To compute the term $\partial f_k/\partial p$ the analytical derivatives of χ_e and σ with respect to the model parameters p were computed. These expressions can be found in Appendix B.1.

Now every term in the sensitivity equation is known, the state sensitivities $\partial x_k/\partial p$ can be computed by solving the ODE (Equation 5.19) for each parameter in the parameter vector p. Once the state sensitivities are known, the cost function gradient with respect to the model parameters $\mathrm{d}J/\mathrm{d}p$ can be computed.

A check was made between the analytical calculation of the cost function gradient $\mathrm{d}J/\mathrm{d}p$ and the numerical approximation. A typical result is shown in figure 5.2, the analytical and numerical gradient agree.
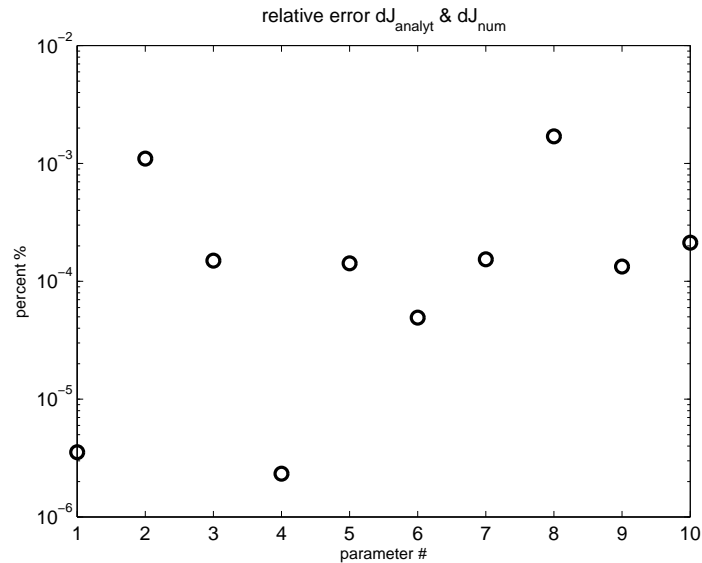
Figure 5.2: A perturbation δp was added to the parameters $\chi_{neo}(1)$, $c_{ano}(2)$, $a_{ic}(3)$, $w_{ic}(4)$, $d_{ic}(5)$, $c_{\chi saw}(6)$, $w_{\chi saw}(7)$, $c_{T_e}(8)$, $c_{\sigma saw}(9)$ and $w_{\sigma saw}(10)$. The variation of the cost function J was calculated numerically $dJ = J(p + \delta p) - J(p)$ and with the analytical gradient: $dJ = \frac{dJ}{dp}\delta p$. dJ was nonzero for all parameter perturbations and its numerical and analytical calculated values agree well, as can be seen from the relative difference between them.

5.4 Demonstration: Finding known model parameters from simulated data

A numerical experiment was performed to demonstrate that the developed algorithm is able to find the optimal model parameters in χ_e and $\sigma_\parallel$. The algorithm that was used is shown in Figure 5.1. For this experiment the block with experimental data in this figure contains data of the T_e, q and U_{pl} profiles generated by RAPTOR itself without any artificial noise. A plasma shot of 0.3 seconds with reversed shear and sawteeth was simulated. A time step of 1ms was used in the simulation and eleven ρ gridpoints equally distributed from 0 to 1. In Figure 5.3 the typical profile evolutions during this experiment are shown.
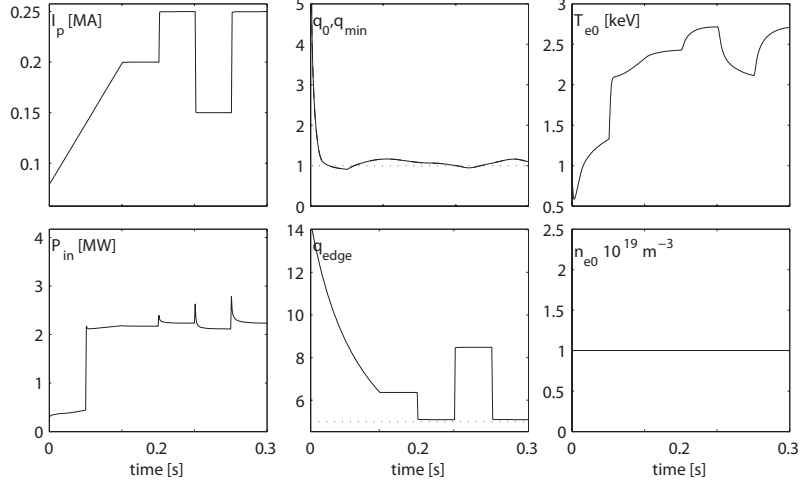
Figure 5.3: Time traces of key quantities for the simulated experiment.

The numerical experiment was performed to show that the algorithm is capable to find the model parameters $\chi_{neo} = 0.5$, $c_{ano} = 7$, $a_{ic} = 0.5$, $w_{ic} = 3$, $c_{\chi saw} = 10$, $w_{\chi saw} = 10$, $c_{T_e} = 0.8$, $c_{\sigma saw} = 0.5$ and $w_{\sigma saw} = 10$ which were used to simulate the data.

In Figure 5.4 the cost function is plotted versus the number of iteration steps. The cost function reduces as the number of iterations increase. This is because the estimated model parameters converge to the true model parameters. At the final iteration step, the estimated model parameters are converged to the exact solution as is shown in Figure 5.5.
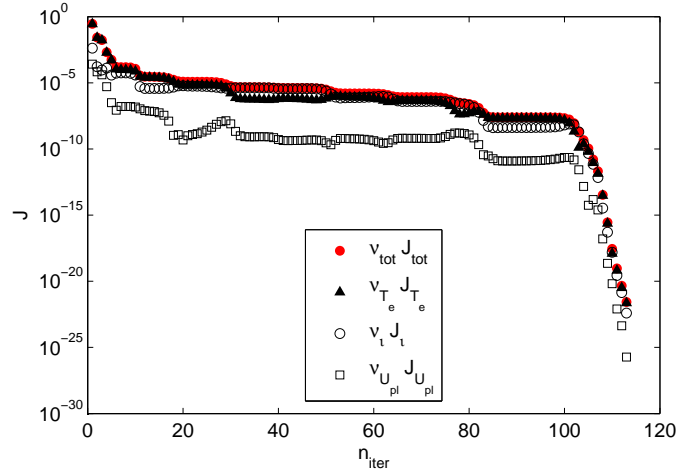
Figure 5.4: The cost function versus the iteration steps of the numerical experiment to demonstrate the parameter estimation algorithm. The definition of the cost function J and weighting factors ν were introduced in Section 5.3.1.
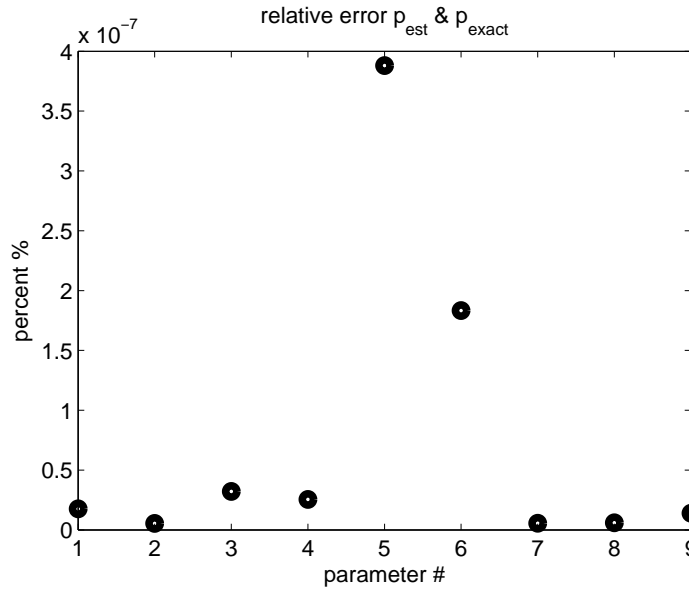
33

Figure 5.5: An numerical experiment was designed in which sawteeth and reversed shear are present. No noise was added. The developed algorithm is able to find back the parameters $\chi_{neo}(1)$, $c_{ano}(2)$, $a_{ic}(3)$, $w_{ic}(4)$, $c_{\chi saw}(5)$, $w_{\chi saw}(6)$, $c_{T_e}(7)$, $c_{\sigma saw}(8)$ and $w_{\sigma saw}(9)$ that were used to generate the data. This figure shows that the relative difference between the estimated parameters and the exact parameters is negligible at the final iteration step.

In Figure 5.6 the relative error of ι versus time and iteration step is depicted. In Figure 5.7, the relative error of T_e versus time and iteration step is plotted, and in Figure 5.8 the relative error of the loop voltage U_{pl} at the final time point (0.3s) is shown versus iteration step. The relative errors reduce with increasing number of iterations as the estimated model parameters converge to the model parameters which were used to generate the data.
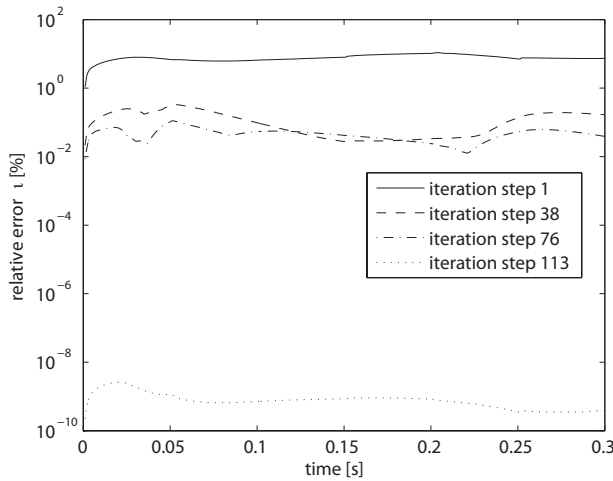

Figure 5.6: The relative error of ι versus time and iteration step.
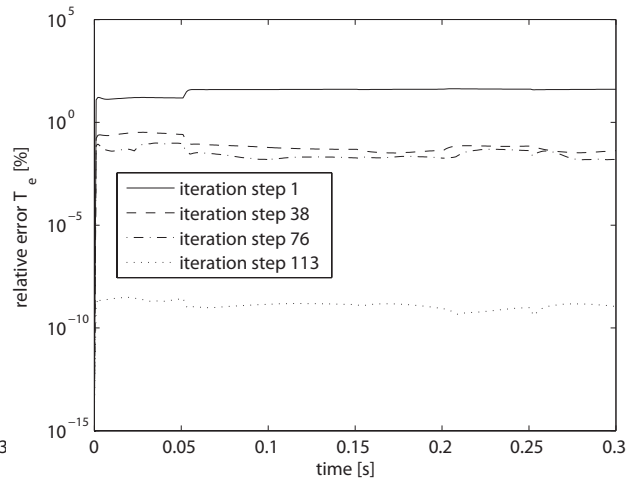

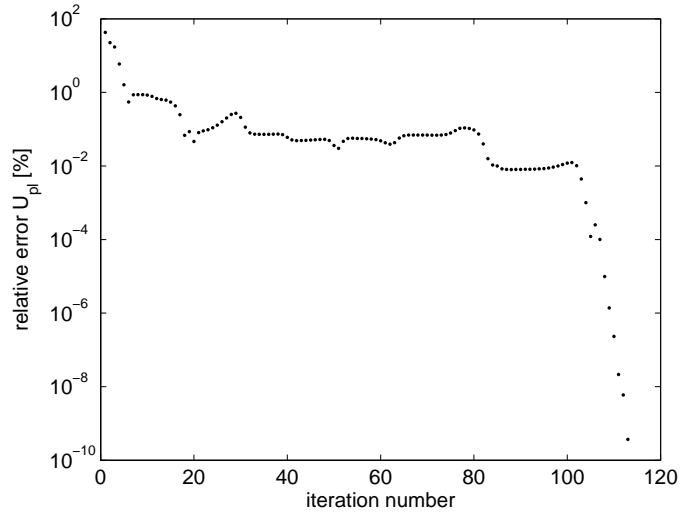Figure 5.7: The relative error of T_e versus time and iteration step.

Figure 5.8: The relative error of loop voltage U_{pl} at the final time point (0.3s) versus iteration step.

This numerical experiment shows that the developed parameter estimation algorithm is able to find the optimal parameters which describe the experimental data best.

5.4.1 Adding noise to numerical experiment

It is not sufficient to compute the optimal parameters and to state that this is the estimated value of the unknown model parameters in χ_e and $\sigma_\parallel$. It must also be investigated what the reliability and precision of the estimated parameters is. A parameter is ill-determined if its estimated value can be affected strongly by seemingly insignificant variations in the data. In essence, then, it is attempted to answer the question 'If the series of experiments were repeated many times, how would the estimates differ from one replication to the next'. Therefore a new numerical experiment was performed. The algorithm that was used is shown in Figure 5.1. For this experiment the block with experimental data in this figure contains the synthetic data of the T_e, q and U_{pl} profiles generated by RAPTOR contaminated with an artificial white noise source with a standard deviation of 0.01. This numerical experiment also reflects reality: an experiment with measured T_e, q and U_{pl} is never clean but always contaminated with noise.

A 50ms seconds plasma with reversed shear but no (!) sawteeth was simulated. In the numerical experiment the algorithm was used to find back the model parameters χ_{neo}, c_{ano}, $\chi_{central}$, δ_0, a_{ic}, w_{ic}, d_{ic}, $c_{\chi saw}$, $w_{\chi saw}$ and c_{T_e} which were used to generate the synthetic dataset. Indeed, one expects that the model parameters $c_{\chi saw}$, $w_{\chi saw}$ cannot be found back, because the dataset reflects a plasma condition without sawteeth crashes.

In Table 5.1 the results of this numerical experiment are presented. The first thing that should be noted is the large difference between the estimated and exact values of $c_{\chi saw}$ and $w_{\chi saw}$. During the parameter optimization process the values of $c_{\chi saw}$ and $w_{\chi saw}$ remained at their initial values. The changes in the two model parameters cannot be observed in the model's input-output mapping, which means the two parameters are not identifiable. This is expected because a plasma condition without sawteeth crashes was simulated: the safety profile q is at all time at every location greater than one, making the Equation 4.5 equal to zero everywhere. The same conclusion could be drawn by analyzing the singular value decomposition (SVD) of the Hessian matrix at the estimated model parameters $\hat{p}$ plotted in Figure 5.9. The plot shows two Hessian singular values that are very small. This corresponds to directions in parameter space that have only very small influence on the cost function J. In this example the two columns of U that correspond to the small singular values are a linear combination of only $c_{\chi saw}$ and $w_{\chi saw}$. Thus, without

35

even knowing the plasma conditions of the experiment the conclusion that the $c_{\chi saw}$ and $w_{\chi saw}$ parameters are unobservable can again be drawn from the SVD analysis.

The information from the singular value decomposition of the Hessian model can be used for model reduction. The subspace corresponding to the $c_{\chi saw}$ and $w_{\chi saw}$ parameters can be removed. This subspace has only very small influence on the cost function J. For the reduced model the standard deviations of the estimated parameters $\hat{p}$ and the 95% confidence intervals are tabled in Table 5.1.

Table 5.1: Results parameter estimation for the numerical experiment contaminated with white noise.

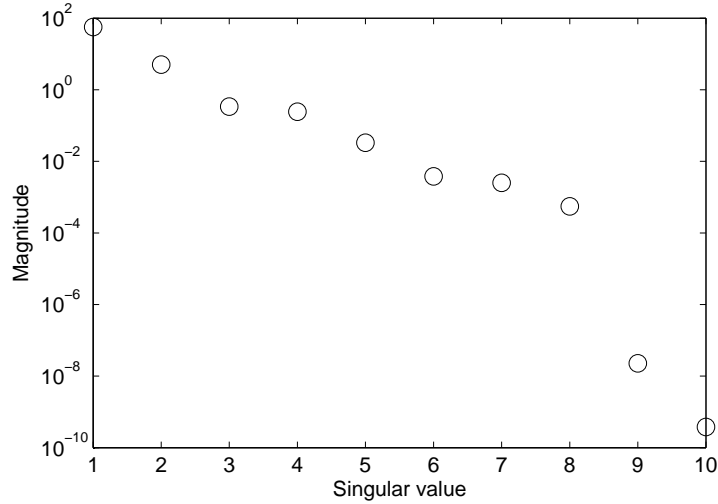|	χ_{neo}	c_{ano}	$\chi_{central}$	δ_0	a_{ic}	d_{ic}	w_{ic}	$c_{\chi saw}$	$w_{\chi saw}$	c_{T_e}
true p	0.5	4	20	0.25	0.5	0.1	3	3	10	0.5
estimated $\hat{p}$	0.4634	4	19.9809	0.2491	0.5049	0.0686	2.9661	6	7	0.5015
relative error [%]	7.3186	0	0.0956	0.3603	0.9830	31.38	1.1301	-	-	0.3005
95 % conf. int. $\hat{p}$ [%]	61.425	1.4737	14.8212	6.2319	11.094	126.533	19.0764	-	-	1.7242

Figure 5.9: The Singular values of the Hessian matrix.

The true parameters are all covered by the 95% confidence intervals. However, there is a large degree of uncertainty for the model parameters χ_{neo} and d_{ic}. The Correlation Matrix provides some insight into the nature of the ill conditioning. For the optimal solution, the Correlation Matrix is

$$R(\hat{p}) = \begin{bmatrix} 1.0000 & -0.8511 & 0.3485 & -0.6226 & 0.4664 & -0.3813 & -0.6329 & 0.5384 \\ -0.8511 & 1.0000 & -0.1916 & 0.4673 & -0.2901 & 0.2072 & 0.4193 & -0.8623 \\ 0.3485 & -0.1916 & 1.0000 & -0.9331 & -0.1367 & -0.2785 & 0.0806 & -0.0106 \\ -0.6226 & 0.4673 & -0.9331 & 1.0000 & 0.0065 & 0.3643 & 0.1063 & -0.1868 \\ 0.4664 & -0.2901 & -0.1367 & 0.0065 & 1.0000 & -0.7936 & -0.9297 & 0.2508 \\ -0.3813 & 0.2072 & -0.2785 & 0.3643 & -0.7936 & 1.0000 & 0.7154 & -0.1102 \\ -0.6329 & 0.4193 & 0.0806 & 0.1063 & -0.9297 & 0.7154 & 1.0000 & -0.3246 \\ 0.5384 & -0.8623 & -0.0106 & -0.1868 & 0.2508 & -0.1102 & -0.3246 & 1.0000 \end{bmatrix}$$

Note the strong positive and negative correlations between pairs of parameters. For example, the strong negative correlation between χ_{neo} ($R(\hat{p})_{21}$) and c_{ano} ($R(\hat{p})_{22}$) tells us that by increasing χ_{neo} and simultaneously decreasing c_{ano} we can obtain a solution that is very nearly as good as

our optimal solution.

Parameter d_{ic} ($R(\hat{p})_{66}$) has a strong negative correlation with a_{ic} ($R(\hat{p})_{65}$). This can be understood by looking at Figure 4.1: the value of the shear function $F(s)$, and thus the cost function J, remains the same when d_{ic} is slightly increased and a_{ic} decreased.

5.4.2 Conclusions numerical experiment

The developed algorithm for parameter estimation successfully retrieves model parameters and a statistical approach was used to gain more insight in the reliability and precision of the estimated parameters. The remaining of this chapter will present the results for the parameter estimation of RAPTOR for TCV shots.

5.5 Parameter estimation for TCV

The Tokamak à Configuration Variable (TCV) is an experimental tokamak at the École Polytechnique Fédérale de Lausanne, Switzerland. The medium size TCV tokamak was designed to study confinement and stability for a wide variety of plasma shapes. This is made possible by a set of sixteen independently controlled poloidal field coils, as well as a vacuum vessel that can accommodate highly elongated plasmas. TCV is equipped with an electron cyclotron heating (ECH) and current drive (ECCD) system.

During a two week visit to TCV, data from the extensive transport code ASTRA [5] was gathered. The ASTRA code simulated five TCV shots constrained with the diagnostics information at TCV:

1. A steady state Ohmic shot;

2. A steady state shot with constant ECH;

3. A shot with time-varying ECH;

4. Shot 46712 with time-varying ECCD and ECH;

5. Shot 46715 with time-varying ECCD and ECH.

The free model parameters of χ_e and σ in RAPTOR were tuned to match ASTRA's q, T_e and U_{pl} profiles for each shot specific and for all shots together. The goal of this research at TCV was to demonstrate the developed parameter estimation method and to tune RAPTOR for the TCV tokamak. This enhances the TCV closed-loop and open-loop control schemes that make use of the RAPTOR predictions.

5.5.1 All shots simultaneously

RAPTOR uses simplifications and assumptions. The unknown physics of χ_e and σ which is more complicated and less well understood is captured in its model parameters. This unmodeled physics is different for each of the five shots. Therefore it is expected that the estimated model parameters will differ for each shot.

In this section the optimal model parameters for not one specific shot, but the five shots simultaneous are estimated. In the remainder of this chapter it will be investigated if the estimated model parameter of the several shots simultaneously are "universally" applicable, i.e do they describe each specific shot well?

The cost function which was minimized for the five shots simultaneous is given by Equation 5.18. The choice was made to optimize the following model parameters in $\sigma_\parallel$ and χ_e

$$\chi_{neo}, \ c_{ano}, \ c_{\chi saw}, \ w_{\chi saw}, \ c_{T_e}, \ c_{\sigma saw} \text{ and } w_{\sigma saw},$$

The model parameters which describe sawteeth are listed, because sawtooth crashes are present in the TCV shots. However, the model parameters a_{ic}, w_{ic}, d_{ic} were not estimated. This because

the TCV shots do not represent advanced plasma scenarios characterized by a very low ($s \leq 0.01$) or negative magnetic shear s for which the function $F(s)$ (Equation 4.2) is nonzero. This can be seen from the figures in Appendix B.2 which show that the temporal evolution of the minimum magnetic shear in the ρ interval between 0.05 and 1 largely exceeds 0.01.

As a result, the ASTRA simulation data does not contain information about the a_{ic}, w_{ic}, d_{ic} model parameters, i.e the given datasets are not persistently exciting at these model parameters, which means they are unidentifiable. The default values $a_{ic} = 1, w_{ic} = 3, d_{ic} = 0.01$ were used throughout the parameter estimation procedure for the TCV shots.

In Table 5.2 the estimated parameters are given when using all shots simultaneously, later in this chapter the properties of the estimated parameters are investigated by discussing the corresponding 95 % confidence intervals. In the remainder of this chapter the model parameters are estimated for each shot specific. Each time a comparison with the optimal model parameters obtained from optimizing for all the five shots simultaneous is made.

Table 5.2: Estimated parameters all shots.

	χ_{neo}	c_{ano}	$c_{\chi saw}$	$w_{\chi saw}$	c_{T_e}	$c_{\sigma saw}$	$w_{\sigma saw}$
estimated p^*	0.4705	2.5743	13.4097	25.9812	0.9247	0.6673	1.0000
95 % conf. int. p^* [%]	8.76	6.227	16.7834	23.92	6.39	1.843	23.4811

5.5.2 Ohmic shot

The model parameters a_{ic}, w_{ic}, d_{ic} are not identifiable from the steady state Ohmic dataset, because the magnetic shear is positive as already explained in the previous section. During the simulation of the steady state Ohmic shot with the ASTRA code, the sawtooth module was turned off. Therefore only the model parameters χ_{neo}, c_{ano} and c_{T_e} in the RAPTOR code remained to be optimized in order to match the T_e, q and U_{pl} profiles with ASTRA. The heat diffusivity equation (Equation 4.4) reduces in this case to

$$\chi_e = \chi_{neo} + c_{ano}\rho q \Big(\frac{T_{e_0}[eV]}{1000} \Big)^{c_{T_e}},$$

The neoclassical electrical conductivity formula does not contain model parameters to estimate. The cost function which was minimized to obtain the optimal model parameters was introduced in Section 5.3.1. In this case only one time slice of the ASTRA data was used for the optimization, since the steady state shot has time constant T_e, ι and U_{pl} profiles. The cost function minimizes the difference between the T_e, ι and U_{pl} profiles calculated by ASTRA and RAPTOR. The evolution of the cost function versus the iteration steps is depicted in Figure 5.10. The estimated parameters at the final iteration step are shown in Table 5.3. Figures 5.11, 5.12 and 5.13 show that the T_e, ι and U_{pl} profiles of RAPTOR and ASTRA agree well for the shot-specific optimal parameters. The discrepancy becomes larger when using the model parameters obtained from optimizing the five TCV shots at once. The 95 % confidence intervals of the estimated model parameters, shown in Table 5.3, are large. This is of three reasons

1. The Ohmic shot is in steady state. The plasma profile dynamics are not sufficiently excited, making the parameters poorly identifiable. This is reflected by the large confidence intervals;

2. Analyzing the Correlation Matrix $R(\hat{p})$ learns that c_{ano} and c_{T_e} are strongly negatively correlated: the effect of increasing c_{ano} on χ_e can be compensated by reducing c_{T_e};

$$R(\hat{p}) = \begin{bmatrix} 1.0000 & 0.8384 & -0.8364 \\ 0.8384 & 1.0000 & -0.9996 \\ -0.8364 & -0.9996 & 1.0000 \end{bmatrix}$$

3. The extremely large confidence interval of c_{T_e} is caused by the fraction $T_{e_0}[eV]/1000 \approx 1$. The exponent c_{T_e} has very little influence on the fraction.
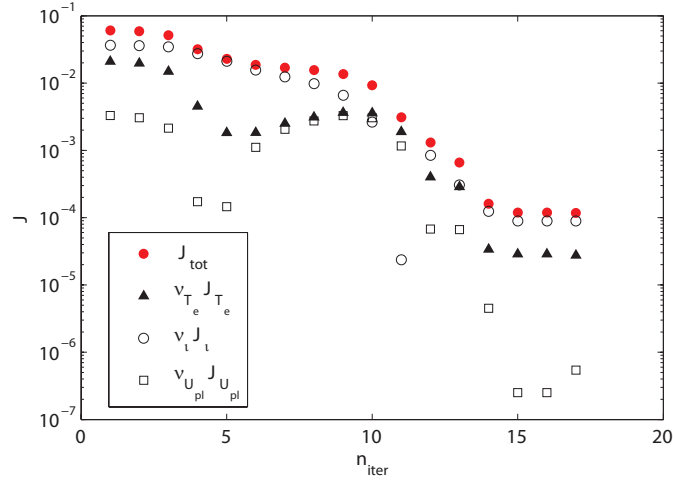
38

Figure 5.10: Cost function versus iteration step for the shot specific optimization. The definition of the cost function J and weighting factors ν were introduced in Section 5.3.1.
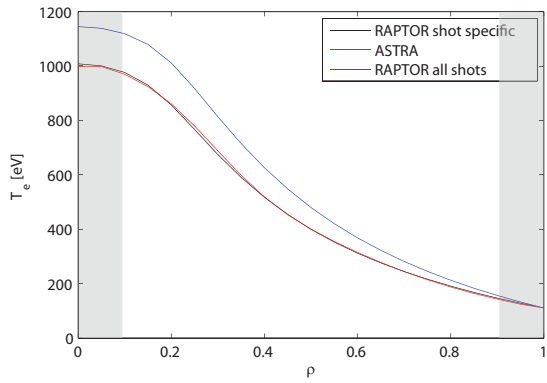

Figure 5.11: The T_e profiles of ASTRA and RAP-TOR. The difference between the profiles in the grey zones was disregarded during the cost function minimization. This because the cost function is only defined for the region $0.1 \leq \rho \leq 0.9$.
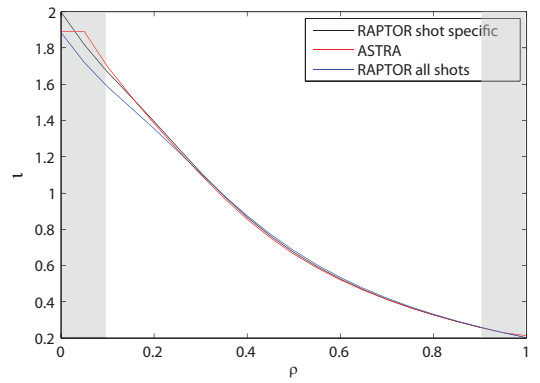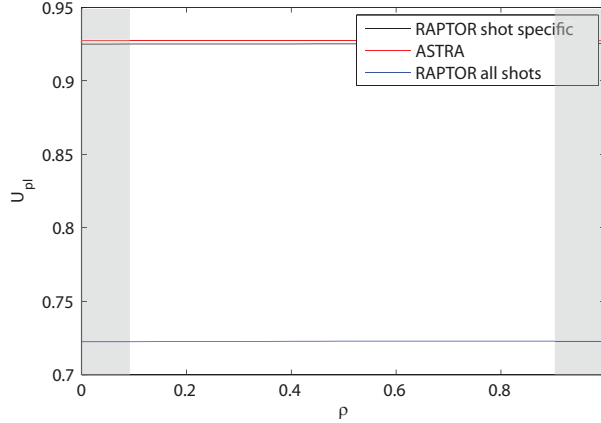

Figure 5.12: The ι profiles of ASTRA and RAP-TOR. The difference between the profiles in the grey zones was disregarded during the cost function minimization. This because the cost function is only defined for the region $0.1 \leq \rho \leq 0.9$.

Figure 5.13: The U_{pl} profiles of ASTRA and RAPTOR. The difference between the profiles in the grey zones was disregarded during the cost function minimization. This because the cost function is only defined for the region $0.1 \leq \rho \leq 0.9$.

Table 5.3: Estimated model parameters in RAPTOR for the Ohmic shot

	χ_{neo}	c_{ano}	c_{T_e}
estimated p^*	0.6093	4.7880	0.1049
95 % conf. int. p^* [%]	6.5218	114.4873	$1.2876e+05$

5.5.3 ECH constant shot

ASTRA simulated a steady state shot with constant ECH power. In this shot sawteeth were present. The $\chi_{neo}, c_{ano}, c_{\chi saw}, w_{\chi saw}, c_{T_e}, c_{\sigma saw}$ and $w_{\sigma saw}$ model parameters in RAPTOR were estimated. The evolution of the cost function versus the iteration steps is depicted in Figure 5.14. Like for the Ohmic shot, only one time slice of the ASTRA data was used for the optimization, since the steady state ECH shot has time constant T_e, ι and U_{pl} profiles. The estimated parameters at the final iteration step are shown in Table 5.4. The T_e, ι and U_{pl} profiles of RAPTOR and ASTRA agree well for the shot-specific optimal parameters (See Figures 5.15, 5.16 and 5.17). The discrepancy becomes larger when using the model parameters obtained from optimizing the five TCV shots at once. The 95 % confidence intervals of the estimated model parameters, shown in Table 5.4, are large. Just like with the Ohmic shot of the previous section, the large confidence intervals are a consequence of the lack of time evolution of the profiles. The constant T_e, ι and U_{pl} profiles can be approximated by RAPTOR by using different parameter combinations. This is reflected by the Correlation Matrix

$$R(\hat{p}) = \begin{bmatrix} 1.0000 & -0.8005 & -0.9743 & -0.9861 & -0.9805 & -0.2456 & 0.0423 \\ -0.8005 & 1.0000 & 0.6746 & 0.8686 & 0.8457 & 0.2895 & -0.0318 \\ -0.9743 & 0.6746 & 1.0000 & 0.9240 & 0.9478 & 0.1585 & -0.0817 \\ -0.9861 & 0.8686 & 0.9240 & 1.0000 & 0.9777 & 0.2739 & -0.0417 \\ -0.9805 & 0.8457 & 0.9478 & 0.9777 & 1.0000 & 0.0959 & -0.2069 \\ -0.2456 & 0.2895 & 0.1585 & 0.2739 & 0.0959 & 1.0000 & 0.9391 \\ 0.0423 & -0.0318 & -0.0817 & -0.0417 & -0.2069 & 0.9391 & 1.0000 \end{bmatrix}$$

The Correlation Matrix shows strong correlations between the parameters, meaning that insufficient information is available in the data to estimate the model parameters uniquely. This results in the large confidence intervals. As an intermediate conclusion -as already explained in Section 5.2.3- it can be stated that the model parameters can only be uniquely estimated if the data is

sufficiently rich. In the remainder of this chapter, shots are therefore used which are not in steady state.
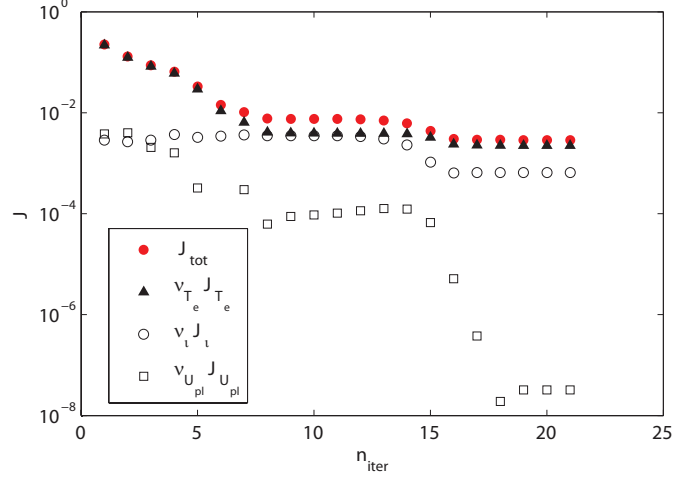

Figure 5.14: Cost function versus iteration step for the shot specific optimization. The definition of the cost function J and weighting factors ν were introduced in Section 5.3.1.
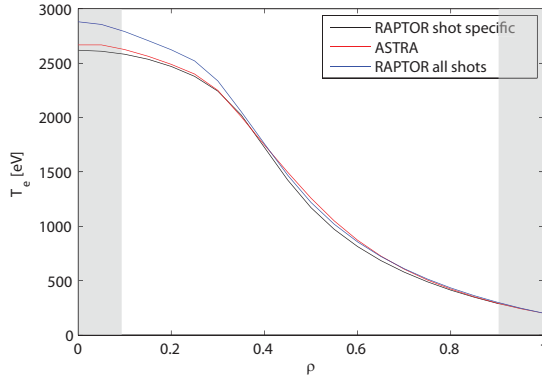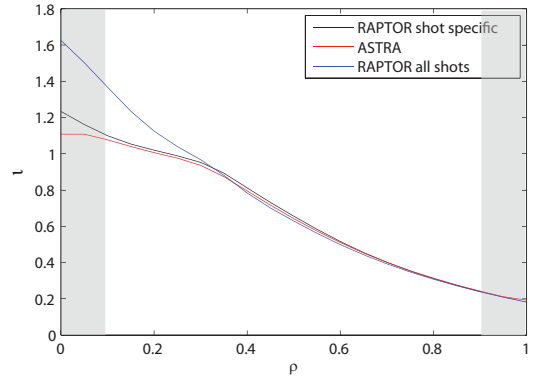

Figure 5.15: The T_e profiles of ASTRA and RAPTOR. The difference between the profiles in the grey zones was disregarded during the cost function minimization. This because the cost function is only defined for the region $0.1 \leq \rho \leq 0.9$.
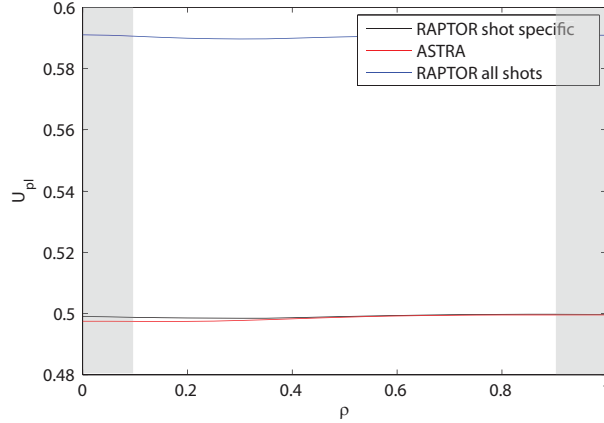

Figure 5.16: The ι profiles of ASTRA and RAPTOR. The difference between the profiles in the grey zones was disregarded during the cost function minimization. This because the cost function is only defined for the region $0.1 \leq \rho \leq 0.9$.

Figure 5.17: The U_{pl} profiles of ASTRA and RAPTOR. The difference between the profiles in the grey zones was disregarded during the cost function minimization. This because the cost function is only defined for the region $0.1 \leq \rho \leq 0.9$.

Table 5.4: Estimated model parameters in RAPTOR for the ECH constant shot.

	χ_{neo}	c_{ano}	$c_{\chi saw}$	$w_{\chi saw}$	c_{T_e}	$c_{\sigma saw}$	$w_{\sigma saw}$
estimated p^*	0.1097	6.7700	40.3061	24.2333	0.1079	0.4007	25.7524
95 % conf. int. p^* [%]	614.8452	31.5018	597.0649	399.5239	35.1810	163.2638	370.6626

5.5.4 ECH varying shot

ASTRA simulated a shot with varying electron cyclotron heating. In the middle of the shot (at $t = 0.9s$) the ECH power was changed. This shot contains sawteeth. Time traces of key quantities of the shot are depicted in Figure 5.18. The simulated dataset is richer compared to the two previous discussed shots, because it contains T_e, ι and U_{pl} profile dynamics due to the change in ECH power. In Table 5.5 the estimated parameters for this shot are listed. Firstly, the RAPTOR predictions are compared with ASTRA before analyzing the identifiability of the parameters. In Figure 5.19 the decrease of the cost function is plotted with increasing iteration steps for the shot specific estimated parameters. The cost function is dominated by the electron temperature residue. This can also be concluded from analyzing Figures 5.20 and 5.21: the relative error of T_e is larger than the relative error of the two other profiles. From this figure it can also be seen that the relative error of the T_e profile is smaller when using the estimated parameters for all the five shots simultaneously than when using the shot specific parameters. However, the shot specific parameters result in a better total solution: the sum of the weighted relative errors of the T_e, ι and U_{pl} profiles is lower than when using the estimated parameters for all shots at once.
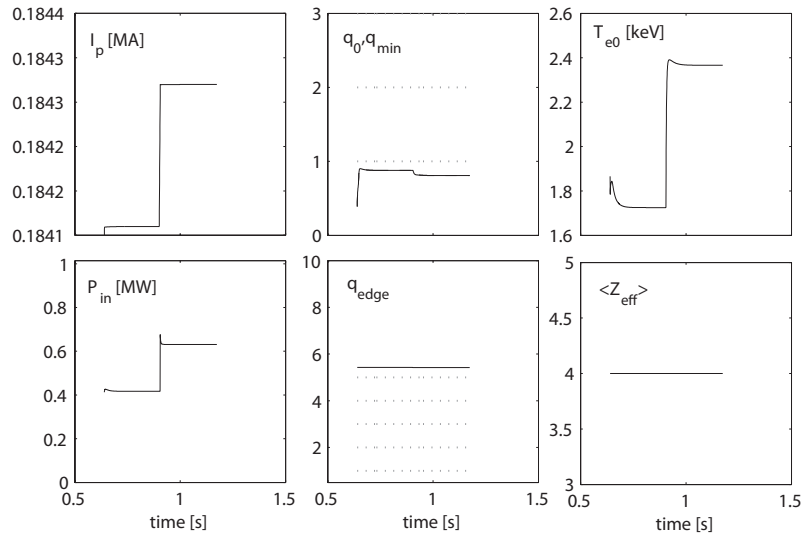
Figure 5.18: Time traces of key quantities for the ECH varying shot.
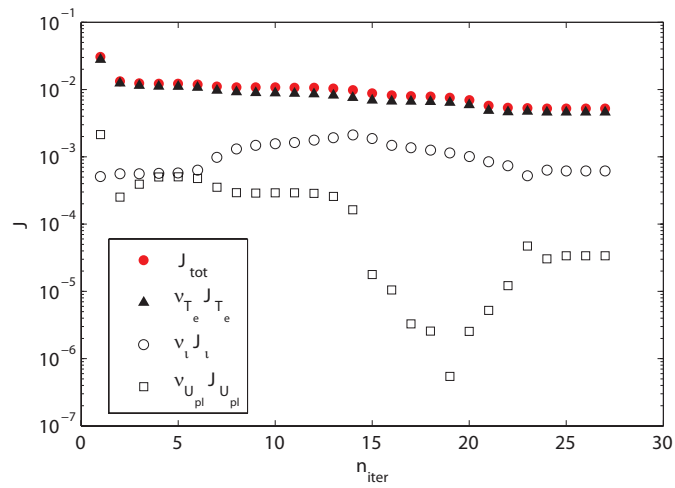

Figure 5.19: Cost function versus iteration step for the shot specific optimization. The definition of the cost function J and weighting factors ν were introduced in Section 5.3.1.
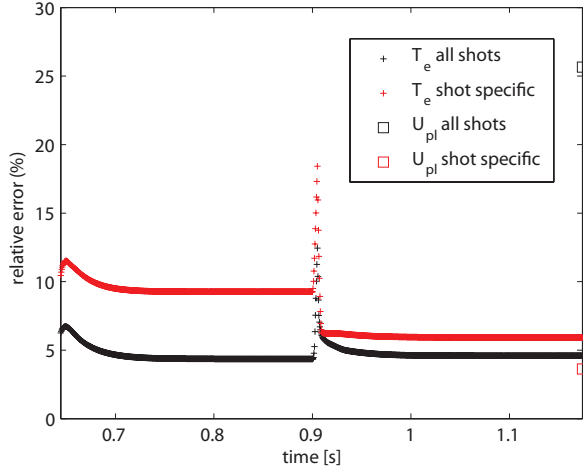
Figure 5.20: The relative difference between the T_e and U_{pl} profiles of ASTRA and RAPTOR defined by $\frac{100}{n_{rho}}\|\frac{\Delta T_e(t)}{T_{e,ASTRA}(t)}\|_1$ and $\frac{100}{n_{rho}}\|\frac{\Delta U_{pl}(t_{final})}{U_{pl,ASTRA}(t_{final})}\|_1$ respectively. The 1-norm is taken over the radial ρ grid. The plot shows the results of the RAPTOR profiles generated with shot optimized parameters and "all shots" optimal parameters.
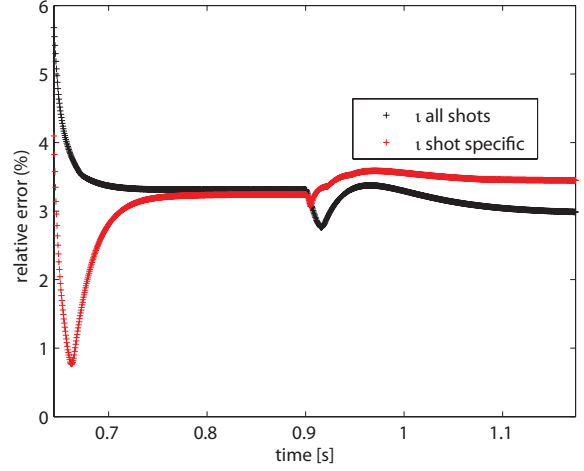
Figure 5.21: The relative difference between the ι profile of ASTRA and RAPTOR defined by $\frac{100}{n_{rho}}\|\frac{\Delta \iota(t)}{\iota_{ASTRA}(t)}\|_1$. The 1-norm is taken over the radial ρ grid. The plot shows the results of the RAPTOR profiles generated with shot optimized parameters and "all shots" optimal parameters.

Table 5.5 shows that the 95 % confidence intervals become smaller compared to the steady state ohmic shot and the steady state shot with constant ECH. The shot with varying ECH shot is a richer dataset because it contains time-varying profiles. The confidence interval of χ_{neo} is large. This can be understood by considering the relative contribution of χ_{neo} to the χ_e profile. A typical χ_e profile for this shot is depicted in Figure 5.22. The relative contribution of χ_{neo} to the χ_e profile is very small. Perturbing the value of χ_{neo} will have little influence on χ_e and thus the cost function. It can be concluded that the model parameter χ_{neo} is poorly observable in the data. Lastly, the large confidence intervals of the model parameters $c_{\chi saw}$, $w_{\chi saw}$, $c_{\sigma saw}$ and $w_{\sigma saw}$ can be understood by analyzing the contribution of the sawteeth to the cost function. The cost function which was minimized is shown in Equation 5.17. The 1-norm of the profile differences of ASTRA and RAPTOR is taken over the ρ interval from 0.1 to 0.9. The sawteeth occur in the region $0 \leq \rho \leq 0.2$. As a results the contribution of the sawteeth region to the 1-norm is little and hence the cost function. Variations of the $c_{\chi saw}$, $w_{\chi saw}$, $c_{\sigma saw}$ and $w_{\sigma saw}$ model parameters therefore do not change the cost function as much as the model parameters that have influence on the full ρ interval (e.g c_{ano} or c_{T_e}).
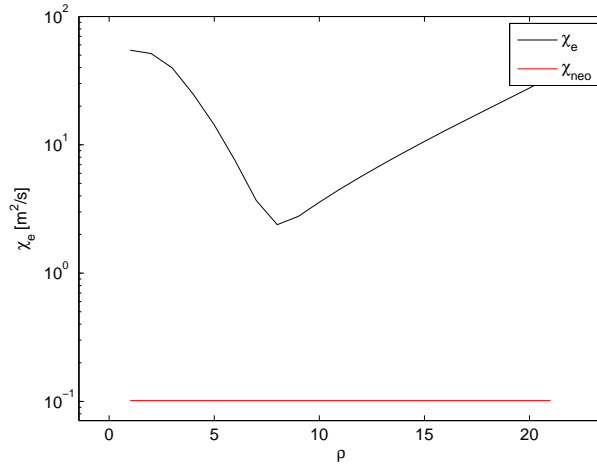
Figure 5.22: Typical χ_e profile for the shot with ECH varying power.

Table 5.5: Estimated model parameters in RAPTOR for the ECH varying shot

	χ_{neo}	c_{ano}	$c_{\chi saw}$	$w_{\chi saw}$	c_{T_e}	$c_{\sigma saw}$	$w_{\sigma saw}$
estimated p^*	0.1014	4.2582	55.0000	32.1570	0.4313	0.3426	25.6677
95 % conf. int. p^* [%]	220.63	3.5773	25.5445	15.2315	9.1555	44.0934	104.2817

5.5.5 ECCD/ECH shot 46712

ASTRA simulated TCV shot 46712 with varying ECCD and ECH. The total power of the electron cyclotron was changed four times during the shot. In this shot sawtooth crashes were present. Time traces of key quantities of the shot are depicted in Figure 5.23. The evolution of the cost function versus the iteration steps is depicted in Figure 5.24. The estimated parameters at the final iteration step are shown in Table 5.6.

The T_e, ι and U_{pl} profiles of RAPTOR and ASTRA agree well for the shot-specific optimal parameters. This can be see from Figures 5.25 and 5.26 which show that the temporal evolution of the relative errors between the ASTRA and RAPTOR profiles are small. The discrepancy becomes larger when using the model parameters obtained from optimizing the five TCV shots at once. In Figure 5.27 the temporal evolution of the relative profile errors is plotted again, but this time the T_e and ι profiles are plotted that correspond to a given error at specific time point. The 95 % confidence intervals of the estimated model parameters, shown in Table 5.6, are smaller compared to the two previously discussed steady state shots and the shot with the one time only changing ECH power. In this case the ECH and ECCD powers are changed four times during the shot, leading to a more informative dataset from which the model parameters can be estimated. The Correlation Matrix for this shot is

$$
R(\hat{p}) = \begin{bmatrix}
1.0000 & -0.3566 & -0.4965 & -0.9987 & -0.0817 & 0.1176 & 0.9862 \\
-0.3566 & 1.0000 & 0.2101 & 0.3925 & -0.8705 & 0.0594 & -0.2160 \\
-0.4965 & 0.2101 & 1.0000 & 0.4878 & -0.1254 & -0.4249 & -0.5017 \\
-0.9987 & 0.3925 & 0.4878 & 1.0000 & 0.0476 & -0.0814 & -0.9767 \\
-0.0817 & -0.8705 & -0.1254 & 0.0476 & 1.0000 & 0.0387 & -0.2149 \\
0.1176 & 0.0594 & -0.4249 & -0.0814 & 0.0387 & 1.0000 & 0.2046 \\
0.9862 & -0.2160 & -0.5017 & -0.9767 & -0.2149 & 0.2046 & 1.0000
\end{bmatrix}
$$

The Correlation matrix shows strong cross correlation between parameters. The model parameters can not be determined uniquely. (e.g c_{ano} and c_{T_e} are strongly negatively correlated: the effect of

45

increasing c_{ano} on the cost function can be compensated by reducing c_{T_e}).
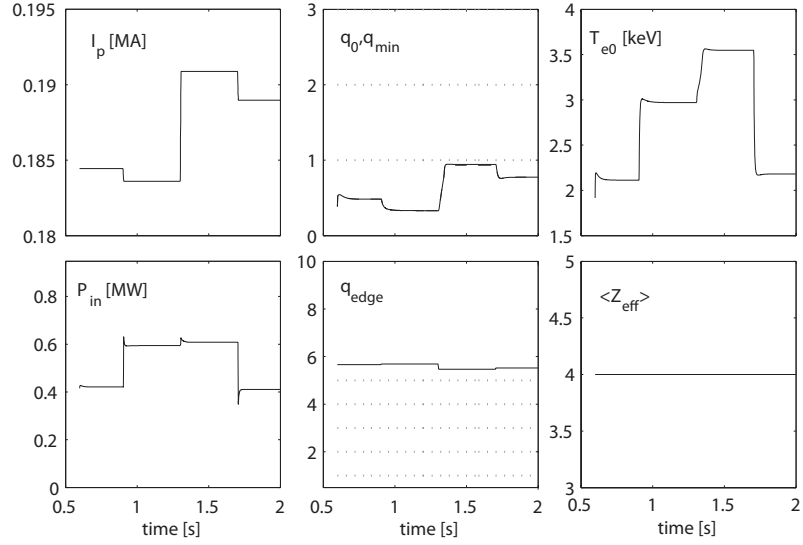

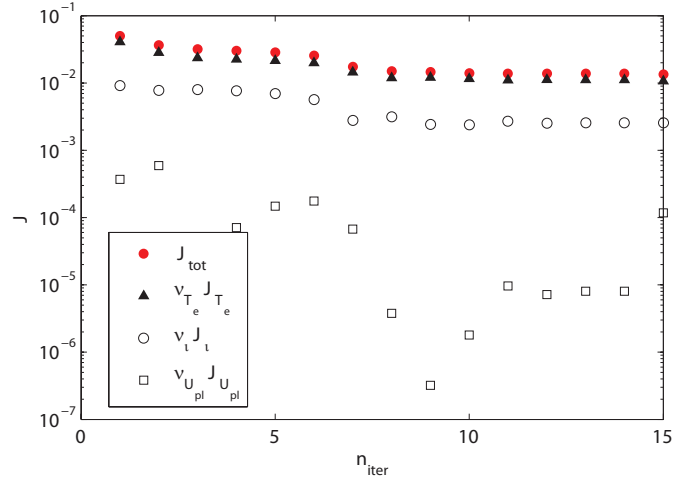Figure 5.23: Time traces of key quantities for the ECCD/ECH shot 46712.

Figure 5.24: Cost function versus iteration step for the shot specific optimization. The definition of the cost function J and weighting factors ν were introduced in Section 5.3.1.

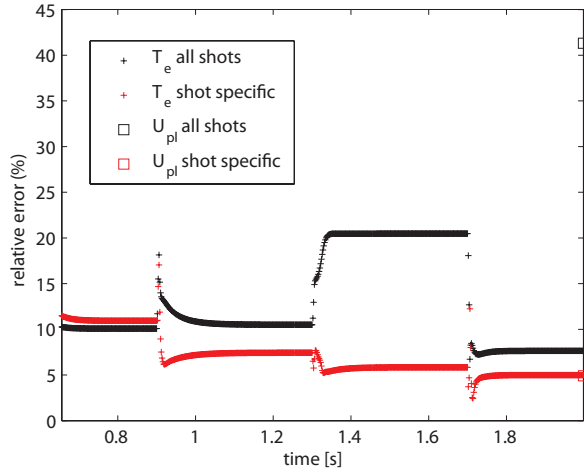Figure 5.25: The relative difference between the T_e and U_{pl} profiles of ASTRA and RAPTOR defined by $\frac{100}{n_{rho}}\|\frac{\Delta T_e(t)}{T_{e,ASTRA}(t)}\|_1$ and $\frac{100}{n_{rho}}\|\frac{\Delta U_{pl}(t_{final})}{U_{pl,ASTRA}(t_{final})}\|_1$ respectively. The 1-norm is taken over the radial ρ grid. The plot shows the results of the RAPTOR profiles generated with shot optimized parameters and "all shots" optimal parameters.
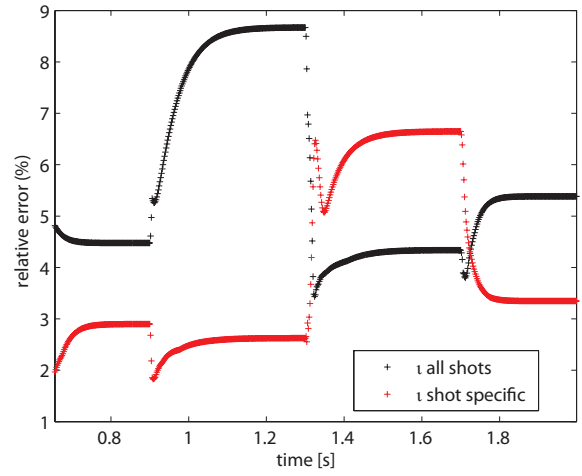
Figure 5.26: The relative difference between the ι profile of ASTRA and RAPTOR defined by $\frac{100}{n_{rho}}\|\frac{\Delta\iota(t)}{\iota_{ASTRA}(t)}\|_1$. The 1-norm is taken over the radial ρ grid. The plot shows the results of the RAPTOR profiles generated with shot optimized parameters and "all shots" optimal parameters.
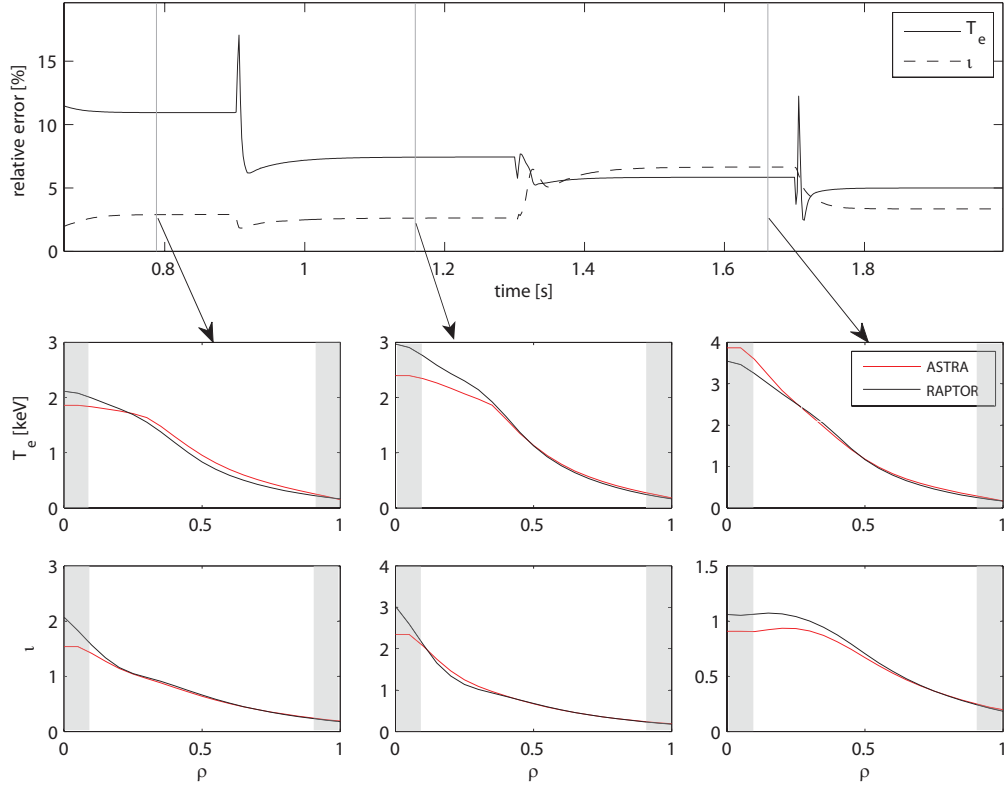
Figure 5.27: Relative error plots for the shot-optimized model parameters and the corresponding T_e and ι profiles. The difference between the profiles in the grey zones was disregarded during the cost function minimization. This because the cost function is only defined for the region $0.1 \leq \rho \leq 0.9$.

Table 5.6: Estimated model parameters in RAPTOR for the ECCD/ECH 46712 shot

	χ_{neo}	c_{ano}	$c_{\chi saw}$	$w_{\chi saw}$	c_{T_e}	$c_{\sigma saw}$	$w_{\sigma saw}$
estimated p^*	0.1302	4.1753	4.1977	17.0948	0.1071	0.2098	46.1202
95 % conf. int. p^* [%]	21.89	4.9592	6.70	23.7394	39.2445	11.0186	5.0968

5.5.6   ECCD/ECH shot 46715

TCV shot 46715 contains sawteeth and has varying ECH and ECCD. Like in shot 46712, the electron cyclotron power was changed four times during the shot. Time traces of key quantities of the shot are depicted in Figure 5.28. The evolution of the cost function versus the iteration steps is depicted in Figure 5.29. The estimated parameters at the final iteration step are listed in Table 5.7.

Figures 5.30 and 5.31 show that the temporal evolution of the relative errors between the ASTRA and RAPTOR profiles are small when using the shot-specific optimal parameters. From these two figures it can also be seen that the relative errors of the T_e and U_{pl} profiles are larger when using the estimated model parameters for all the five shots simultaneously than when using the shot specific parameters. The difference between the ι profile of ASTRA and RAPTOR decreases when using the model parameters for all the five shots at once. The cost function was constructed such that the ι, T_e and U_{pl} profiles have equal importance to be minimized. The shot-specific parameters, which yield better estimates for two of the three profiles (T_e and U_{pl}), result therefore

in a lower costfunction.

In Figure 5.27 the temporal evolution of the relative profile errors is plotted again, but this time the T_e and ι profiles are plotted that correspond to a given error at specific time point
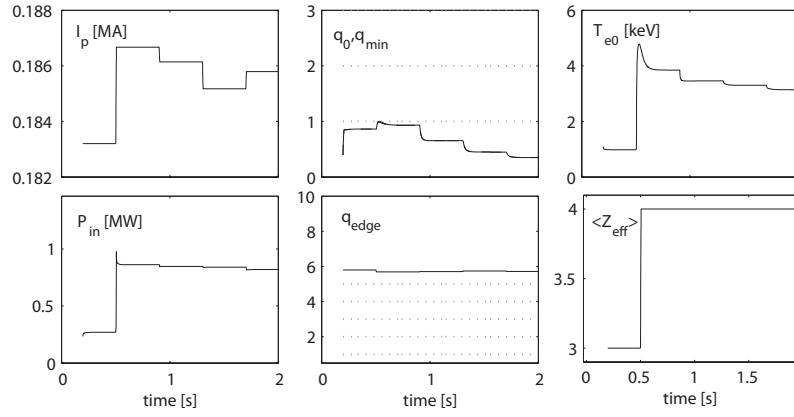

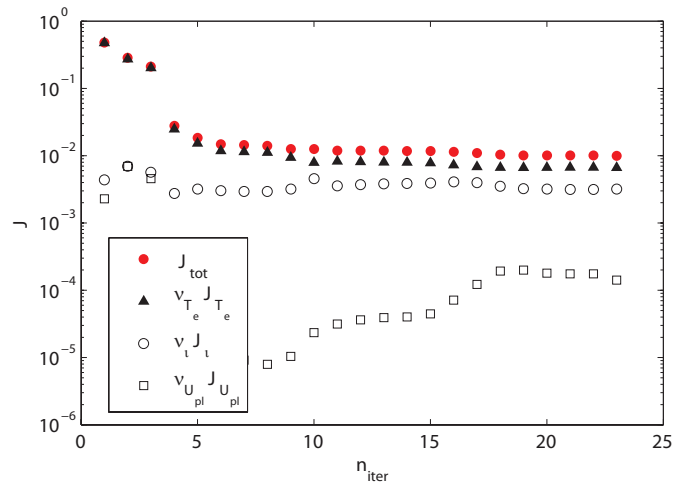Figure 5.28: Time traces of key quantities for the ECCD/ECH shot 46715.

Figure 5.29: Cost function versus iteration step for the shot specific optimization. The definition of the cost function J and weighting factors ν were introduced in Section 5.3.1.
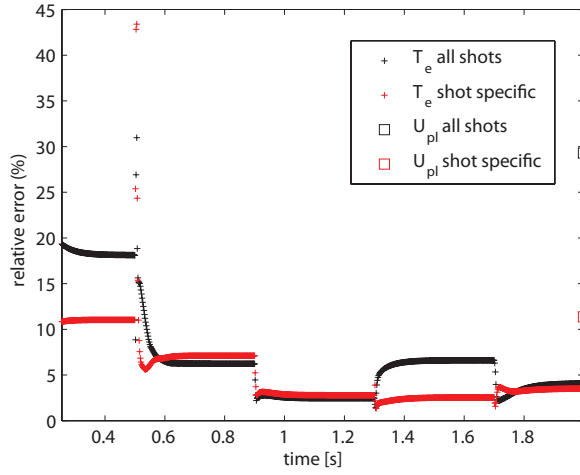
Figure 5.30: The relative difference between the T_e and U_{pl} profiles of ASTRA and RAPTOR defined by $\frac{100}{n_{rho}}\|\frac{\Delta T_e(t)}{T_{e,ASTRA}(t)}\|_1$ and $\frac{100}{n_{rho}}\|\frac{\Delta U_{pl}(t_{final})}{U_{pl,ASTRA}(t_{final})}\|_1$ respectively. The 1-norm is taken over the radial ρ grid. The plot shows the results of the RAPTOR profiles generated with shot optimized parameters and "all shots" optimal parameters.

Figure 5.31: The relative difference between the ι profile of ASTRA and RAPTOR defined by $\frac{100}{n_{rho}}\|\frac{\Delta\iota(t)}{\iota_{ASTRA}(t)}\|_1$. The 1-norm is taken over the radial ρ grid. The plot shows the results of the RAPTOR profiles generated with shot optimized parameters and "all shots" optimal parameters.
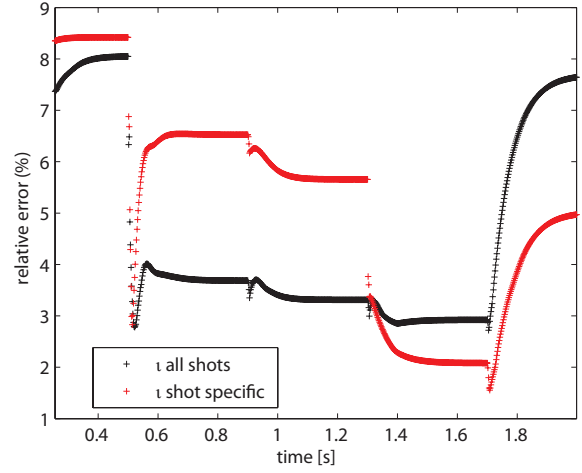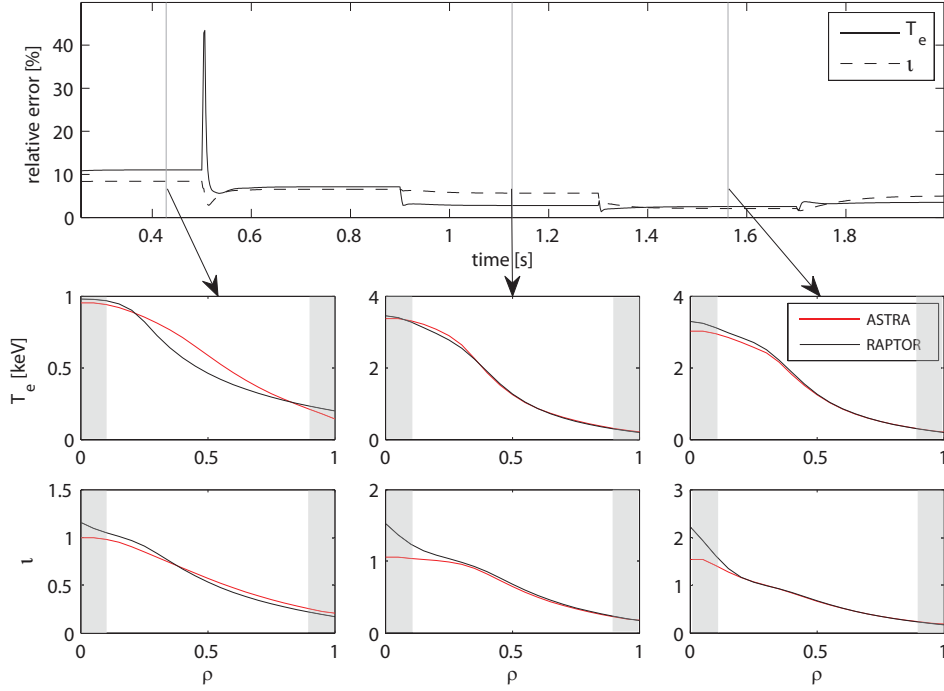
Figure 5.32: Relative error plots for the shot-optimized model parameters and the corresponding T_e and ι profiles. The difference between the profiles in the grey zones was disregarded during the cost function minimization. This because the cost function is only defined for the region $0.1 \leq \rho \leq 0.9$.

Table 5.7: Estimated model parameters in RAPTOR for the ECCD/ECH 46715 shot

	χ_{neo}	c_{ano}	$c_{\chi saw}$	$w_{\chi saw}$	c_{T_e}	$c_{\sigma saw}$	$w_{\sigma saw}$
estimated p^*	0.1553	7.1550	10.5143	22.2398	0.1519	0.2182	20.1452
95 % conf. int. p^* [%]	176.29	6.6971	6.5384	23.9578	26.4807	10.3758	36.9827

5.6   Overview of the estimated model parameters

In Table 5.8 an overview is given of the estimated model parameters for each shot specific and all shots simultaneous.

Table 5.8: Estimated parameters

	χ_{neo}	c_{ano}	$c_{\chi saw}$	$w_{\chi saw}$	c_{T_e}	$c_{\sigma saw}$	$w_{\sigma saw}$
Ohmic shot							
	χ_{neo}	c_{ano}	$c_{\chi saw}$	$w_{\chi saw}$	c_{T_e}	$c_{\sigma saw}$	$w_{\sigma saw}$
estimated p^*	0.6093	4.7880	00.0000	00.0000	0.1049	00.0000	00.0000
95 % conf. int. p^* [%]	6.5218	114.4873	00.0000	00.0000	$1.2876e+05$	00.0000	00.0000
ECCD/ECCH shot 46712							
	χ_{neo}	c_{ano}	$c_{\chi saw}$	$w_{\chi saw}$	c_{T_e}	$c_{\sigma saw}$	$w_{\sigma saw}$
estimated p^*	0.1302	4.1753	4.1977	17.0948	0.1071	0.2098	46.1202
95 % conf. int. p^* [%]	21.89	4.9592	6.70	23.7394	39.2445	11.0186	5.0968
ECCD/ECCH shot 46715							
	χ_{neo}	c_{ano}	$c_{\chi saw}$	$w_{\chi saw}$	c_{T_e}	$c_{\sigma saw}$	$w_{\sigma saw}$
estimated p^*	0.1553	7.1550	10.5143	22.2398	0.1519	0.2182	20.1452
95 % conf. int. p^* [%]	176.29	6.6971	6.5384	23.9578	26.4807	10.3758	36.9827
ECH constant shot							
	χ_{neo}	c_{ano}	$c_{\chi saw}$	$w_{\chi saw}$	c_{T_e}	$c_{\sigma saw}$	$w_{\sigma saw}$
estimated p^*	0.1097	6.7700	40.3061	24.2333	0.1079	0.4007	25.7524
95 % conf. int. p^* [%]	614.8452	31.5018	597.0649	399.5239	35.1810	163.2638	370.6626
ECH varying shot							
	χ_{neo}	c_{ano}	$c_{\chi saw}$	$w_{\chi saw}$	c_{T_e}	$c_{\sigma saw}$	$w_{\sigma saw}$
estimated p^*	0.1014	4.2582	55.0000	32.1570	0.4313	0.3426	25.6677
95 % conf. int. p^* [%]	220.63	3.5773	25.5445	15.2315	9.1555	44.0934	104.2817
All shots							
	χ_{neo}	c_{ano}	$c_{\chi saw}$	$w_{\chi saw}$	c_{T_e}	$c_{\sigma saw}$	$w_{\sigma saw}$
estimated p^*	0.4705	2.5743	13.4097	25.9812	0.9247	0.6673	1.0000
95 % conf. int. p^* [%]	8.76	6.227	16.7834	23.92	6.39	1.843	23.4811

The model parameters differ for each shot. The model parameters for all shots at once yield T_e and ι predictions that differ at most 20 percent from the profiles of ASTRA for the shots

- ECCD/ECH shot 46712 (see Figures 5.25 and 5.26);

- ECCD/ECH shot 46715 (see Figures 5.30 and 5.31);

- ECH shot with varying ECH (see Figures 5.20 and 5.21).

5.7 Conclusions

A systematic method was developed to estimate the model parameters of χ_e and σ in RAPTOR. The results presented in this chapter show that the method is able to find the model parameters such that RAPTOR agrees with the results of the more complete ASTRA code for the TCV tokamak. The identifiability of the model parameters increases when the dataset contains more time-variation in the profiles. The analysis of the Correlation Matrix shows that, occasionally, model parameters can not be estimated independently: the effect of a specific model parameter can be compensated by an other model parameter.

The shot-specific estimated model parameters differ from each other. This is the result of the simplifications and assumptions used in RAPTOR. The unmodeled physics is captured in the model parameters. This results in the variation of the model parameters for different plasma conditions, because the unmodeled physics changes. Therefore the model parameters were estimated such that the RAPTOR predictions are reliable for a variety of plasma conditions. For this purpose the estimation of the model parameters was done for a dataset containing five different TCV plasma conditions. Model parameters were found for which the maximum relative error of the predicted T_e and ι profiles were below 20 %.

With these model parameters RAPTOR can be used to within an accuracy of 20 % to enhance the TCV closed-loop and open-loop control schemes that make use of the RAPTOR predictions. For better accuracy, extensive runs of the proposed method should be run on many different shots,

such that classes of shots with similar physics properties - and hence model parameters - can be identified and subsequently modeled more accurately with RAPTOR.

Chapter 6

Conclusions

RAPTOR can be used in open-loop and closed-loop control schemes. These control schemes can be used to tailor the q-profile to a desired operation regime. A strong degree of control over this q profile makes the operation of a tokamak more stable (avoidance of plasma instabilities) and efficient (optimal q profile). The performance of the open-loop and closed-loop control system strongly depends on the quality of the RAPTOR predictions.

In this thesis a fast Neutral Beam Injection (NBI) module was developed for RAPTOR. This allows RAPTOR to simulate a multitude of tokamaks including ITER. Benchmarks of this fast NBI module for an ITER-like scenario showed good agreement with large scale NBI codes, while running significantly faster. The more extensive conclusions about this part can be found in Section 3.5.

During this research, the RAPTOR predictions were improved by the extension of the transport model and a newly developed model-parameter estimation routine. This resulted in a better description of the physics and allows for a less ad-hoc and more automated method to implement RAPTOR on a variety of tokamaks.

The model-parameter estimation routine was developed to estimate RAPTOR's model parameters in a systematic way. The model parameters of RAPTOR were estimated for the TCV tokamak. Model parameters were found for which the maximum relative error of the predicted T_e and ι profiles were below 20 % for each specific shot. The estimated model parameters of RAPTOR can be used to enhance the TCV closed-loop and open-loop control schemes that make use of the RAPTOR predictions. The more extensive conclusions about this second part of research can be found in Section 5.7.

Chapter 7

Recommendations for further research

Based on the results and considerations in this thesis, the following list of actions are suggested for future work:

Recommendations for further research for the neutral beam module:

- The developed NBI module can only smooth one peak occurring in the calculated electron heating profile. In the future, the option to smear out several peaks should be added;

- More research is needed to investigate the effect of Z_{eff} on the NBI results of the code. A benchmark in this thesis showed that for a high number of Z_{eff}, the NBI module overestimates the neutral beam current drive;

- The developed NBI code was benchmarked for an ITER-like scenario. More benchmarks for different tokamaks and plasma scenarios should be performed to increase confidence in the developed NBI module.

Recommendations for further research for the developed model-parameter estimation routine:

- The model-parameter estimation routine should be run for a multitude of initial guesses of the model parameters. The nonlinear parameter estimation problem has multiple local minima. By using a shooting method the global minimum could be identified;

- The RAPTOR predictions could be improved by using electron heat diffusivity models χ_e which capture more physics. In the following papers [28], [29] and [30], models for χ_e are presented which are verified with experiments. These χ_e models are relative simple and hence suitable candidates for the fast RAPTOR code. A beneficial feature of the χ_e models mentioned in the papers could be that its model parameters can be estimated more independently compared to the currently used model of χ_e in RAPTOR. The identifiability of the parameters in the proposed χ_e models should be investigated with the methods discussed in this thesis;

- More shots should be investigated for the TCV tokamak to give reliable model parameters estimates. The shots should contain advanced scenarios in order to estimate the model parameters a_{ic}, w_{ic}, d_{ic};

- Instead of using simulation data from more complete codes, the developed method could also use direct profile measurements (T_e, $U_p l$ and ι) to optimize the model parameters. More research should be conducted to investigate the performance of the model-parameter estimation routine in case real profile measurements are used.

Bibliography

[1] Yuh, Howard Yung-Hao. *The Motional Stark Effect diagnostic on Alcator C-Mod*. PhD Thesis. Massachusetts Institute of Technology, 2005

[2] *Investigation of H-mode edge profile behaviour on MAST using Thomson scattering*. PhD thesis, National University of Ireland, 2007

[3] Felici, F. *Real-Time Control of Tokamak Plasmas: from Control of Physics to Physics-Based Control*. PhD thesis. Ecole Polytechnique Federale De Lausanne, 2011

[4] Maljaars, E. *Fast model-based control and prediction of the safety factor profile evolution in tokamak plasmas*. 40th EPS Conference on Plasma Physics

[5] Pereverzev, G. V. and P.N. Yushmanov. *ASTRA Automated System for TRansport Analysis in a Tokamak*. Tech. rep. 5/98. IPP Report, 2002

[6] Artaud, J.F. et al. *The CRONOS suite of codes for integrated tokamak modelling*. Nuclear Fusion 50.4, 2010

[7] R.K. Janev et al. *Penetration of energetic neutral beams into fusion plasmas*. Nucl. Fusion 29 2125, 1989

[8] J. Jacquinot et al. *Physics of energetic ions*. Nucl. Fusion 39, 1999

[9] Wesson, John et al. *Tokamaks*. Oxford University Press, 2004

[10] Kritz, A.H. et al. Proc. 3rd Int. Symp. on Heating in Toroidal Plasmas. Vol. II, 1982

[11] Decker, J and Y Peysson. Report EUR-CEA-FC-1736. Tech. rep. Euratom-CEA, 2004

[12] Wang, Ji. *Predictive simulation of neutral beam injection on EAST in H- and L-mode plasma*. Phys. Scr. 85, 2012

[13] H.C. Howe. *Physics Models in the Tokamak Transport Code PROCTR*, Oak Ridge National Laboratory Report ORNL/TM$-$9537, 1985

[14] D. R. Mikkelsen, C.E. Singer. *Optimization of steady$-$state beam driven tokamak reactors*, 1982

[15] K. Okano. *Neoclassical formula for neutral beam current drive*. Nucl. Fusion 30 423, 1990

[16] J.D. Gaffey. *Energetic Ion Distribution Resulting from Neutral Beam Injection in Tokamaks*. J. Plasma Physics 16, 14, 1976

[17] Madhavan M. Menon *Neutral beam heating applications and development*. Proceedings of the IEEE, vol. 69, N0. 8, 1981

[18] GAO Qing-DI et al. *Stochastic ripple diffusion of energetic particles in reversed magnetic shear tokamak*. Chin. phys. lett, 2004

[19] I.O. Bespamyatnov and W.L. Rowan and K.T. Liao (2012). *ALCBEAM − Neutral beam formation and propagation code for beam-based plasma diagnostics.* Computer Physics Communications

[20] Oikawa T. et al. *Benchmarking of neutral beam current drive codes as a basis for the integrated modeling for ITER* Proc. 22nd Int. Conf. on Fusion Energy, 2008

[21] R.M. Wieland and W.A. Houlberg. *Neutral Beam Deposition in Large, Finite-Beta Noncircular Tokamak Plasmas.* Journal of Fusion Energy, Vol 2, No. 3, 1982

[22] M. Schneider et al. *Simulation of the neutral beam deposition within integrated tokamak modelling frameworks.* Nuclear Fusion 51, 2011

[23] Breslau J.A, Jardin S.C and Park W. *Three-dimensional modeling of the sawtooth instability in a small tokamak.* Physics of plasmas 14, 2007

[24] Alexei Pankin. *Electron Temperature Gradient Model as Part of Integrated Predictive Modeling.* 29th EPS Conference on Plasma Phys. and Contr. Fusion Montreux, 2002

[25] Paul M.J. Van den Hof et al. *Identification of parameters in large scale physical model structures, for the purpose of model-based operations.* Springer, New York, USA, 256 pp. ISBN 978-1-4419-0894-0

[26] Nocedal, Jorge and Stephen Wright. *Numerical Optimization, Series in Operations Research and Financial Engineering.* Springer, 2006

[27] Bard, Y. *Nonlinear Parameter Estimation.* Academic Press, 1974

[28] M. ERBA et al. *Validation of a new mixed Bohm/gyro-bohm model for electron and ion heat transport against the ITER, TORE SUPRA and START database discharges.* Nucl. Fusion 38, 1998

[29] L. Garzotti et al. *Particle transport and density profile analysis of different JET plasmas.* Nucl. Fusion 43, 2003

[30] S. Fietz et al. *Investigation of transport models in ASDEX Upgrade current ramps.* Nucl. Fusion 53, 2013

Appendix A

Neutral beam code

A.1 Model of the beamline geometry

Figure A.1 shows a sketch of a tokamak. The machine coordinate system has its origin at the center of the tokamak. In this appendix a parametrization of the beamline in the machine coordinate system is calculated. This parametrization will be used in combination with an equilibrium to calculate the fluxcoordinate ρ at each point on the beamline. RAPTOR calculates the electron density and temperature profile as function of ρ. Knowing the fluxcoordinate ρ at each point on the beamline thus gives information about the electron temperature and density profile along the beamline. With this information the beam attenuation along the beamline can be calculated and hence the neutral beam power deposition profile.
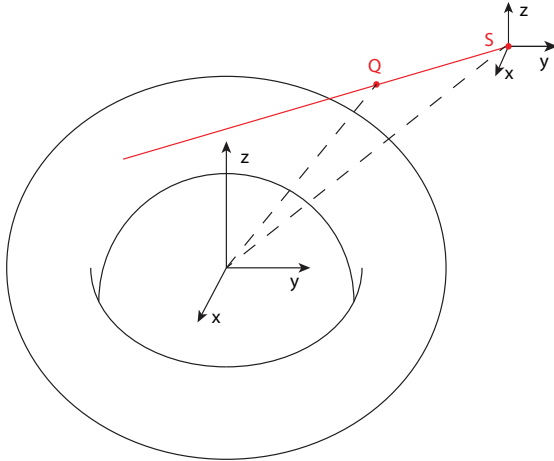
Figure A.1: Sketch of a tokamak and the neutral beam line (red). At the source of the neutral beam S a coordinate system is defined which coincides with the machine coordinate system.
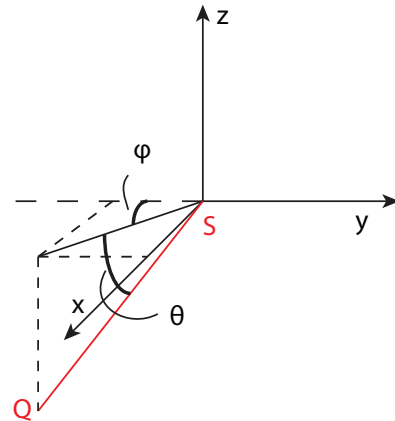
Figure A.2: Zoom of the source of the neutral beam. When the machine coordinates of point S, the horizontal angle ϕ and vertical angle θ are known, the equation of the beamline in the machine coordinate system can be calculated.

Equation of the beamline in the machine coordinate system

Figure A.2 depicts the beamline and its source S. The coordinate system in this figure coincides with the machine coordinate system. The parametrization of the beamline in the machine coordinate system can be calculated, when the coordinates of the source of the neutral beam are known

in the machine coordinate system together with the horizontal angle ϕ and vertical angle θ . Point Q on the beamline (see Figure A.1) is

$$\vec{Q} = \overrightarrow{SQ} + \vec{S}$$

From Figure A.2 the equation of $\overrightarrow{SQ}$ is obtained

$$\overrightarrow{SQ} = \cos(\theta)\sin(\phi)|\overrightarrow{SQ}|\vec{x} - \cos(\theta)\cos(\phi)|\overrightarrow{SQ}|\vec{y} - \sin(\theta)|\overrightarrow{SQ}|\vec{z}$$

The parametrization of point Q on the beamline in the machine coordinate system becomes

$$\vec{Q} = \left(S_x + \cos(\theta)\sin(\phi)|\overrightarrow{SQ}|\right)\vec{x} + \left(S_y - \cos(\theta)\cos(\phi)|\overrightarrow{SQ}|\right)\vec{y} + \left(S_z - \sin(\theta)|\overrightarrow{SQ}|\right)\vec{z}$$

The machine coordinate system can be transformed from cartesian to cylindrical. The R,Z coordinates of point Q in this coordinate system are

$$R_Q = \sqrt{\left(S_x + \cos(\theta)\sin(\phi)|\overrightarrow{SQ}|\right)^2 + \left(S_y - \cos(\theta)\cos(\phi)|\overrightarrow{SQ}|\right)^2} \tag{A.1}$$

$$Z_Q = S_z - \sin(\theta)|\overrightarrow{SQ}| \tag{A.2}$$

A.2 Algorithm to calculate NBCD and NBEH

The algorithm used to calculate the neutral beam current drive and electron heating is described below.

Algorithm 1 A global description of the algorithm to calculate the neutral beam current drive (NBCD) and electron heating (NBEH).

---

for Start up of the beam module calculate once only **do**

    STEP 1

    Use Equation A.1 and A.2 to calculate (R,Z) coordinates of points on the beamline

    STEP 2

    Load in the (ρ,V) profile from RAPTOR to calculate $\frac{\mathrm{d}\rho}{\mathrm{d}V}$ at gridpoints.

    STEP 3

    Load in the equilibrium (R,Z,ρ) used in RAPTOR.

    for $R < R_{plasma}$ **do**

        Map (R,Z) coordinates on the beamline to ρ coordinates using the equilibrium and interpolation.

    end for

    Final result: the evolution of ρ on the beamline is known. This (s,ρ) profile is used to compute $\frac{\mathrm{d}s}{\mathrm{d}\rho}$

    STEP 4

    Load in the grid of ρ values which is used in RAPTOR. At these gridpoints the NBCD and NBEH need to be calculated.

    for $i < length(grid)$ **do**

        Calculate how many times the beamline crosses the specific ρ coordinate.

    end for

    The final result of STEP 4 is that the number of intersections of the beamline with a specific fluxcoordinate is known.

end for

for each time step t **do**

    STEP 5

    RAPTOR gives the $T_e(t)$ and $n_e(t)$ profiles versus the ρ values of the grid. Because STEP 3 gives the evolution of the ρ coordinates along the beamline, the evolution of T_e and n_e along the beamline in function of s is known at each time step. This together with the $\frac{\mathrm{d}s}{\mathrm{d}\rho}$ and $\frac{\mathrm{d}\rho}{\mathrm{d}V}$ profiles and the information on how many times the beamline crosses a certain fluxcoordinate is used to calculate:

    $\Rightarrow$ The neutral beam power deposition per volume (Equation 3.5) versus s. The information in *STEP 1* to *STEP 5* is used to map the neutral beam power deposition per volume to ρ space.

    $\Rightarrow$ The neutral beam electron heating per volume (Equation 3.7). The information in *STEP 1* to *STEP 5* is used to map the neutral beam electron heating per volume to ρ space.

    $\Rightarrow$ The neutral beam current drive per volume (Equation 3.10). The information in *STEP 1* to *STEP 5* is used to map the neutral beam current drive per volume to ρ space.

end for

A.3 Calculation Sensitivities

Neutral Beam focussing

The divergence of the neutral beam is governed by its perveance number. The perveance number is determined by the beam current and energy. During neutral beam operation the perveance is held constant by the operator, making the beam current and energy coupled and hence the beam power and energy. The perveance is defined as:

$$\text{Perv} = \frac{I}{E^{3/2}}$$

The relation between the beam energy E and beam power P_a becomes:

$$P_a = EI = E \ \text{Perv} \ E^{3/2} = \text{Perv} \ E^{5/2}$$

Neutral Beam Electron Heating

$$\bullet \quad \frac{\mathrm{d}P_{NBI,e}}{\mathrm{d}P_{frac,1}} = \frac{\mathrm{d}s}{\mathrm{d}\rho}\frac{\mathrm{d}\rho}{\mathrm{d}V} P_a n_e(s)\phi_e(x(E,s))\sigma(E,Z_{eff})e^{-\int_{s=a}^{s} n_e(s)\sigma(E,Z_{eff})\,\mathrm{d}s}$$

$$\bullet \quad \frac{\mathrm{d}P_{NBI,e}}{\mathrm{d}P_{frac,2}} = \frac{\mathrm{d}s}{\mathrm{d}\rho}\frac{\mathrm{d}\rho}{\mathrm{d}V} P_a n_e(s)\phi_e(x(E/2,s))\sigma(E/2,Z_{eff})e^{-\int_{s=a}^{s} n_e(s)\sigma(E/2,Z_{eff})\,\mathrm{d}s}$$

$$\bullet \quad \frac{\mathrm{d}P_{NBI,e}}{\mathrm{d}P_{frac,3}} = \frac{\mathrm{d}s}{\mathrm{d}\rho}\frac{\mathrm{d}\rho}{\mathrm{d}V} P_a n_e(s)\phi_e(x(E/3,s))\sigma(E/3,Z_{eff})e^{-\int_{s=a}^{s} n_e(s)\sigma(E/3,Z_{eff})\,\mathrm{d}s}$$

$$\bullet \quad \frac{\mathrm{d}P_{NBI,e}}{\mathrm{d}Z_{eff}} = \frac{\mathrm{d}s}{\mathrm{d}\rho}\frac{\mathrm{d}\rho}{\mathrm{d}V} P_a n_e(s) \sum_{i=1}^{3} \phi_e(x(E/i,s))P_{frac,i}\frac{\mathrm{d}\sigma(E/i,Z_{eff})}{\mathrm{d}Z_{eff}} * \dots$$

$$e^{-\int_{s=a}^{s} n_e(s)\sigma(E/i,Z_{eff})\,\mathrm{d}s}\left[1 - \int_{s=a}^{s} n_e(s)\sigma(E/i,Z_{eff})\,\mathrm{d}s\right]$$

, with

$$\frac{\mathrm{d}\sigma(E/i,Z_{eff})}{\mathrm{d}Z_{eff}} = \frac{e^{S_1(E/i,n_e,T_e)}}{E/i}S_z(E/i,n_e,T_e)10^{-20}$$

$$\bullet \quad \frac{\mathrm{d}P_{NBI,e}}{\mathrm{d}T_e} = \frac{\mathrm{d}\phi_e}{\mathrm{d}x}\frac{\mathrm{d}x}{\mathrm{d}T_e}P_{dep} =$$
$$\left(x^{-2}\phi_e - x^{-1}\left[\frac{1}{2}\frac{-x^{-1/2}+1}{(1-x^{1/2}+x)(1+x^{1/2})} + \frac{6x^{-1/2}}{9+(2x^{1/2}-1)^2}\right]\right)\left(-\varepsilon_{bo}\varepsilon_c^{-2}\left(\frac{3\sqrt{\pi}}{4}\right)^{2/3}\left(\frac{m_i}{m_e}\right)^{1/3}\frac{m_b}{m_i}\right)P_{dep}$$

$$\bullet \quad \frac{\mathrm{d}P_{NBI,e}}{\mathrm{d}E} = \frac{P_{NBI,e}}{P_a}\frac{\mathrm{d}P_a}{\mathrm{d}E} + \frac{\mathrm{d}s}{\mathrm{d}\rho}\frac{\mathrm{d}\rho}{\mathrm{d}V}P_a n_e(s)\left(\sum_{i=1}^{3}\frac{\mathrm{d}\phi_{e,i}}{\mathrm{d}E}P_{frac,i}\sigma_i e^{-\int_{s=a}^{s} n_e(s)\sigma_i\,\mathrm{d}s} + \dots\right.$$
$$\left.\sum_{i=1}^{3}\phi_{e,i}P_{frac,i}\frac{\mathrm{d}\sigma_i}{\mathrm{d}E}e^{-\int_{s=a}^{s} n_e(s)\sigma_i\,\mathrm{d}s}\left[1 - \int_{s=a}^{s} n_e(s)\sigma_i\,\mathrm{d}s\right]\right)$$

, with

$$\frac{\mathrm{d}\phi_{e,i}}{\mathrm{d}E} = \frac{\mathrm{d}\phi_{e,i}}{\mathrm{d}x}\frac{\mathrm{d}x}{\mathrm{d}E} = \frac{\mathrm{d}\phi_{e,i}}{\mathrm{d}x}\frac{e}{E_c}$$

$$\frac{\mathrm{d}\sigma_i}{\mathrm{d}E} = -\frac{\sigma_i}{E_i} + \frac{\mathrm{d}S_1}{\mathrm{d}E_i}\sigma_i + m_u 10^{-17}\frac{e^{S_1}}{E_i}(Z_{eff}-1)\frac{\mathrm{d}S_z}{\mathrm{d}E_i}$$

$$\frac{\mathrm{d}P_a}{\mathrm{d}E} = \mathrm{Perv}\,\frac{5}{2}E^{3/2}$$

- $$\frac{\mathrm{d}P_{NBI,e}}{\mathrm{d}Pa} = \frac{\mathrm{d}P_{NBI,e}}{\mathrm{d}E}\frac{\mathrm{d}E}{\mathrm{d}P_a}$$

, with

$$\frac{\mathrm{d}E}{\mathrm{d}P_a} = (\mathrm{Perv}\,\frac{5}{2}E^{3/2})^{-1}$$

Neutral Beam Current Drive

- $$\frac{\mathrm{d}J_{NB}}{\mathrm{d}E} = \left[1 - \frac{Z_b}{Z_{eff}}[1 - G(Z_{eff},\epsilon)]\right]\sum_{i=1}^{3}\frac{\mathrm{d}J_{fi}(\rho)}{\mathrm{d}E}$$

, with

$$\frac{\mathrm{d}J_{fi}(\rho)}{\mathrm{d}E} = eZ_b\tau_s\xi_b\left(v_{b,i}I_i\frac{\mathrm{d}S_i}{\mathrm{d}E} + S_iI_i\frac{\mathrm{d}v_{b,i}}{\mathrm{d}E} + S_iv_{b,i}\frac{\mathrm{d}I_i}{\mathrm{d}E}\right)$$

, in which

$$\frac{\mathrm{d}I_i}{\mathrm{d}E} = \frac{\mathrm{d}I_i}{\mathrm{d}y_c}\frac{\mathrm{d}y_c}{\mathrm{d}v_b}\frac{\mathrm{d}v_b}{\mathrm{d}E}$$

$$\frac{\mathrm{d}v_b}{\mathrm{d}E} = \frac{e}{m_{b,1}v_b}$$

$$\frac{\mathrm{d}y_c}{\mathrm{d}v_b} = -\frac{y_c}{v_b}$$

- $$\frac{\mathrm{d}J_{NB}}{\mathrm{d}P_a} = \frac{\mathrm{d}J_{NB}}{\mathrm{d}E}\frac{\mathrm{d}E}{\mathrm{d}P_a}$$

- $$\frac{\mathrm{d}J_{NB}}{\mathrm{d}P_{frac,1}} = \left[1 - \frac{Z_b}{Z_{eff}}[1 - G(Z_{eff},\epsilon)]\right]\frac{J_{f1}}{P_{frac,1}}$$

- $$\frac{\mathrm{d}J_{NB}}{\mathrm{d}P_{frac,2}} = \left[1 - \frac{Z_b}{Z_{eff}}[1 - G(Z_{eff},\epsilon)]\right]\frac{J_{f1}}{P_{frac,2}}$$

- $$\frac{\mathrm{d}J_{NB}}{\mathrm{d}P_{frac,3}} = \left[1 - \frac{Z_b}{Z_{eff}}[1 - G(Z_{eff},\epsilon)]\right]\frac{J_{f1}}{P_{frac,3}}$$

- $$\frac{\mathrm{d}J_{NB}}{\mathrm{d}T_e} = \left[1 - \frac{Z_b}{Z_{eff}}[1 - G(Z_{eff},\epsilon)]\right]\sum_{i=1}^{3}\frac{\mathrm{d}J_{fi}(\rho)}{\mathrm{d}T_e}$$

, with

$$\frac{dJ_{fi}(\rho)}{dT_e} = eZ_b\tau_s\xi_b S_i v b_i\Big(\frac{dI_i}{dT_e} + \frac{3I_i}{2T_e}\Big)$$

, in which

$$\frac{dI_i}{dT_e} = \frac{dI_i}{dy_c}\frac{dy_c}{dv_c}\frac{dv_c}{dE_c}$$

$$\frac{dy_c}{dv_c} = \frac{1}{v_b}$$

$$\frac{dv_c}{dE_c} = \sqrt{\frac{e}{2m_b E_c}}$$

$$\frac{dE_c}{dT_e} = \Big(\frac{3\sqrt{\pi}}{4}\Big)^{2/3}\Big(\frac{m_i}{m_e}\Big)^{1/3}\frac{m_b}{m_i}$$

- $$\frac{dJ_{NB}}{dZ_{eff}} = \Big(Z_b Z_{eff}^{-2}[1-G] + Z_b(-0.85 Z_{eff}^{-3}\sqrt{\epsilon} + 1.55 Z_{eff}^{-3}\epsilon)\Big)\sum_{i=1}^{3} J_{fi}(\rho) + ...$$
$$\Big(1 - Z_b Z_{eff}^{-1}[1-G]\Big)\frac{d\sum_{i=1}^{3} J_{fi}(\rho)}{dZ_{eff}}$$

A.4   Implementation of the beam code in RAPTOR

Verification of the implementation of the beam code in RAPTOR

The beam code presented in this thesis, was first developed as a stand alone version. In this appendix the results of the benchmark of this stand-alone version with the beam code implemented in RAPTOR are presented.

For this benchmark the same ρ grid, temperature and density profiles were used in both codes as well as the same plasma $2D$ equilibrium. Attention was paid to use the same plasma parameters and beam parameters in both versions of the code. In Figures A.3 and A.4 the neutral beam electron heating profile and neutral beam current drive profile are shown respectively. The stand-alone version of the beam code yield the same results as the implemented beam code in RAPTOR, which demonstrates the correct implementation in RAPTOR.

Verification of the analytic expressions of the sensitivities

In Appendix A.3 the analytical expressions of the sensitivity of the neutral beam electron heating and current drive profile to changes in electron temperature, beam power, electron density,... are derived. The beam code implemented in RAPTOR was used to check these expressions. In this section the sensitivity of the neutral beam electron heating and current drive profile to a perturbation of the electron temperature profile and beam power P_a at the plasma edge was checked. The following two expressions should converge for an infinitesimal change of for instance the temperature profile:

$$\delta P_{NBI,e} \quad = \quad P_{NBI,e}(T_e + \delta T_e) - P_{NBI,e}(T_e) \tag{A.3}$$

$$\delta P_{NBI,e} \quad = \quad \frac{dP_{NBI,e}}{dT_e}\delta T_e \tag{A.4}$$
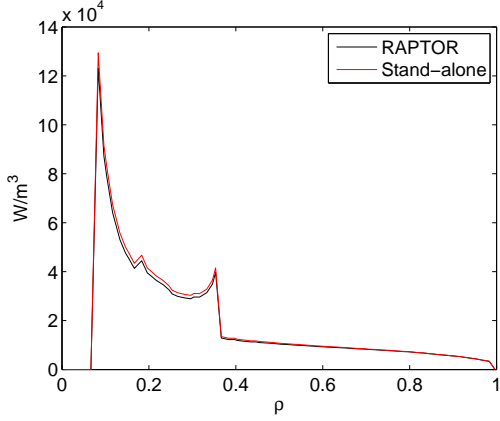
Figure A.3: The beam power to the electrons versus ρ calculated by the stand-alone version and the version implemented in RAPTOR.
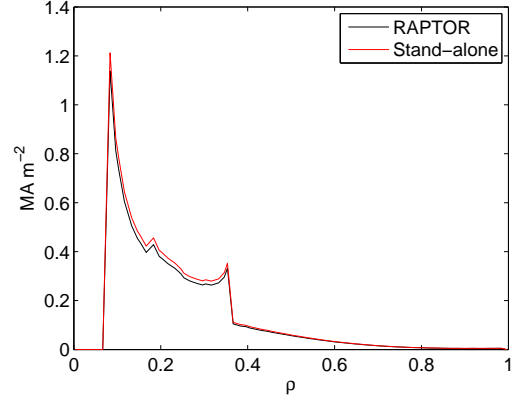
Figure A.4: The neutral beam current drive versus ρ calculated by the stand-alone version and the version implemented in RAPTOR.

The first expression is obtained from subtracting the results of two RAPTOR simulations, the second expression is based on the analytical expression derived in Appendix A.3.

The sensitivity of the neutral beam electron heating and current drive profile to an infinitesimal change in the temperature profile and power at the plasma edge are checked in the figures below. The difference between the numerical (Equation A.3) and analytical (Equation A.4) obtained $\delta P_{NBI,e}$ and δJ_{NB} are shown. From these figures it becomes clear that both approaches converge if the perturbation becomes smaller.
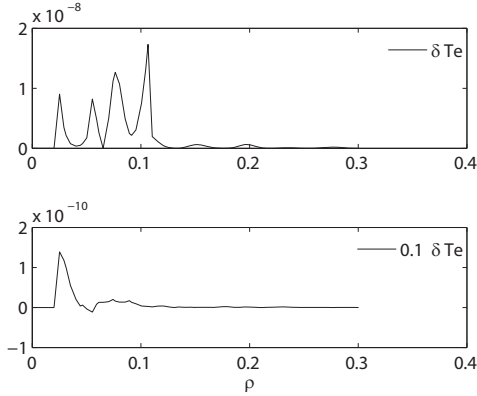
Figure A.5: The difference between $\delta P_{NBI,e}$ obtained from two simulations (Equation A.3) and the analytical approach (Equation A.4). When the perturbation δT_e becomes smaller the two methods converge.
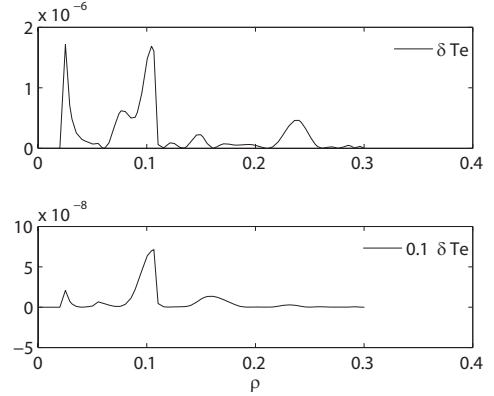
Figure A.6: The difference between δJ_{NB} obtained from two simulations and the analytical approach. When the perturbation δT_e becomes smaller the two methods converge.
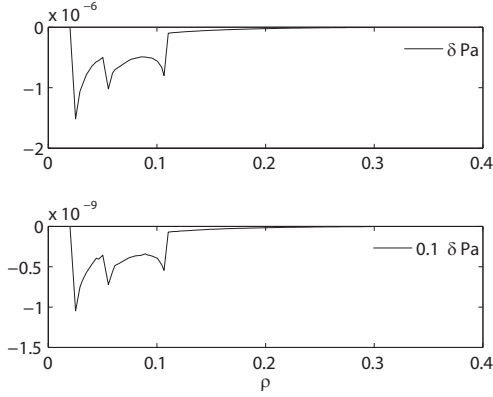
Figure A.7: The difference between $\delta P_{NBI,e}$ obtained from two simulations (Equation A.3) and the analytical approach (Equation A.4). When the perturbation δP_a becomes smaller the two methods converge.
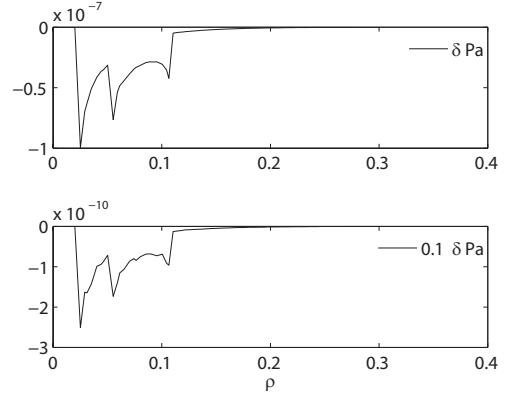
Figure A.8: The difference between δJ_{NB} obtained from two simulations and the analytical approach. When the perturbation δP_a becomes smaller the two methods converge.

A.5 Explanation of the origin of singularities in the developed NBI code
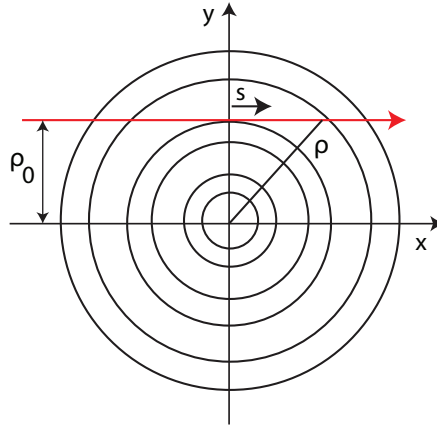
Figure A.9: Poloidal cross-section for a plasma equilibrium.

In Figure A.9 the poloidal cross-section of a typical plasma equilibrium is given together with a neutral beam line path (red line). In this appendix the origin of the singularities that arise in the developed NBI code are explained. Formula 3.5 is used in the NBI code to calculate the neutral beam power deposition per unit volume in the plasma. The first term in this equation $\frac{\mathrm{d}P_{beam}(s)}{\mathrm{d}s}$ contains no singularities, because it is a continuous function (See Equation 3.4). The cause of the singularities must therefore lie in the calculations of $\frac{\mathrm{d}s}{\mathrm{d}\rho}$ and $\frac{\mathrm{d}\rho}{\mathrm{d}V}$. Let's address the two functions in the remainder of this section. The volume enclosed by a flux surface can be approximated by

$$V \approx 2\pi^2 R_0 \rho^2$$

From this equation it follows that

$$\frac{\mathrm{d}\rho}{\mathrm{d}V} = \frac{1}{4\pi^2 R_0 \rho}$$

At the magnetic axis, where $\rho = 0$ a singularity occurs because the volume enclosed by a flux surface goes to zero. This is not the only type of singularity that can occur. The coordinate along the beamline s can be written as

$$s = \sqrt{\rho^2 - \rho_0^2}$$

The term $\frac{\mathrm{d}s}{\mathrm{d}\rho}$ becomes

$$\frac{\mathrm{d}s}{\mathrm{d}\rho} = \frac{2\rho}{2\sqrt{\rho^2 - \rho_0^2}}$$

This gives rise to a singularity at $\rho = \rho_0$.

A.6 Additional benchmarks results of the developed NBI code

For the benchmarks shown in this section the same settings as for the benchmark presented in Chapter 3.5 were used as starting point. In each benchmark one profile was changed (n_e, T_e or Z_{eff}) each time. The last benchmarks shown in this section uses three different profiles of n_e, T_e or Z_{eff} at once.
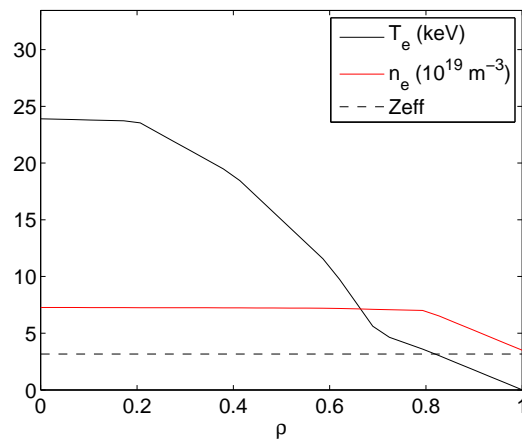
Benchmark 1: n_e variation
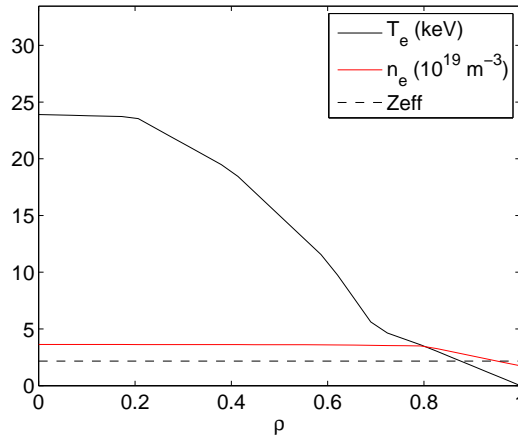
Figure A.10: The profiles of the electron temperature, density and Z_{eff}.
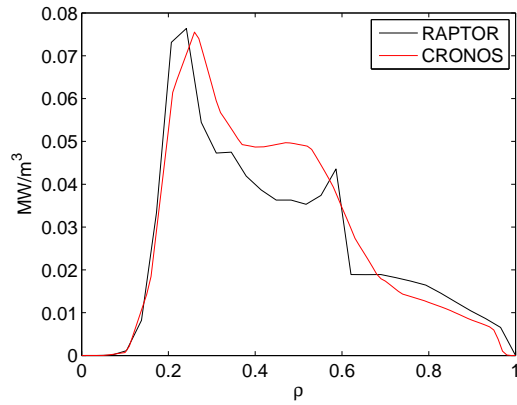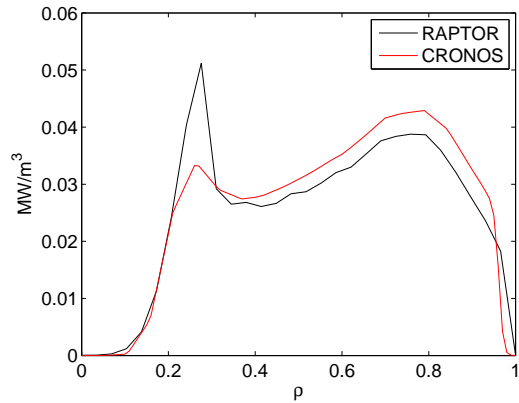
Figure A.11: The beam power to the electrons versus ρ calculated by the developed model and NEMO/SPOT (NBI module in the CRONOS code).
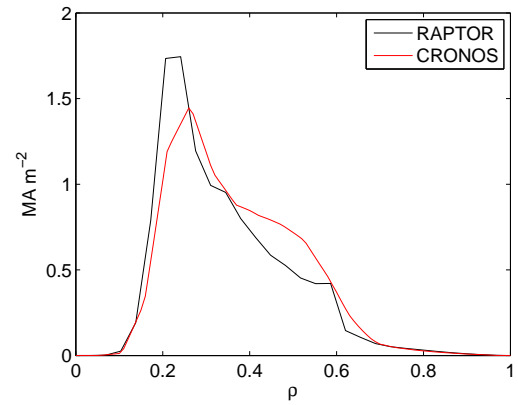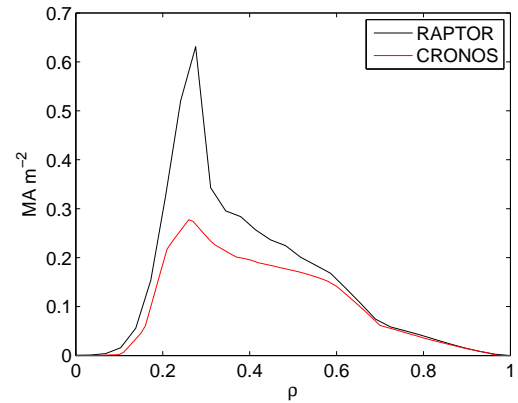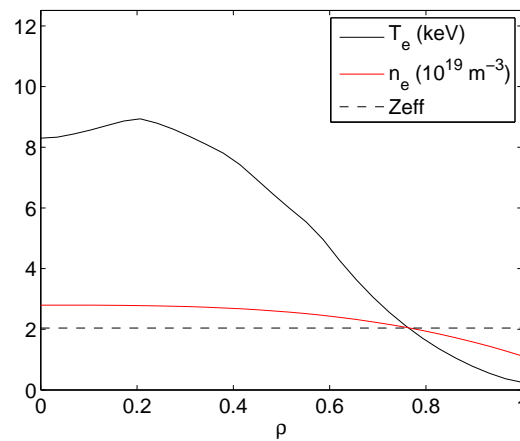

Figure A.12: The neutral beam current drive versus ρ calculated by the developed model and NEMO/SPOT (NBI module in the CRONOS code).

Benchmark 2: T_e variation
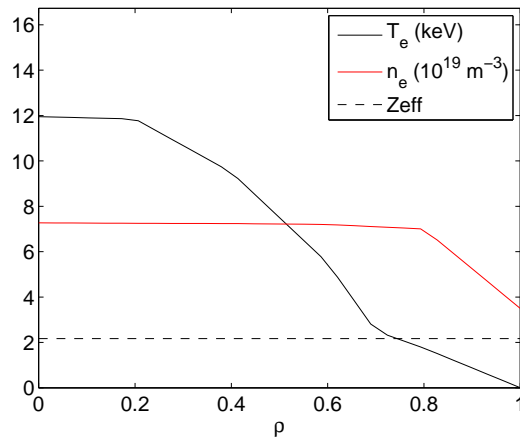
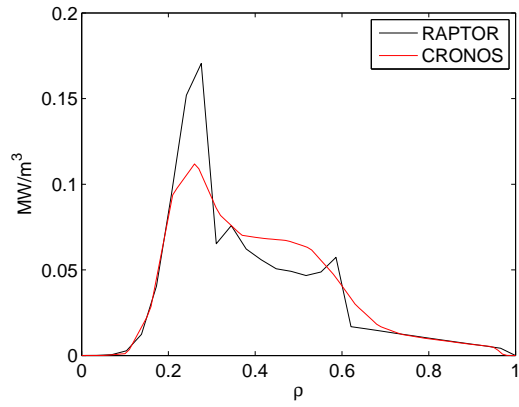Figure A.13: The profiles of the electron temperature, density and Z_{eff}.
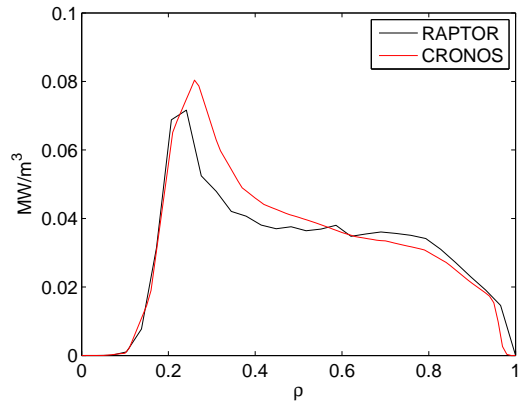
Figure A.14: The beam power to the electrons versus ρ calculated by the developed model and NEMO/SPOT (NBI module in the CRONOS code).
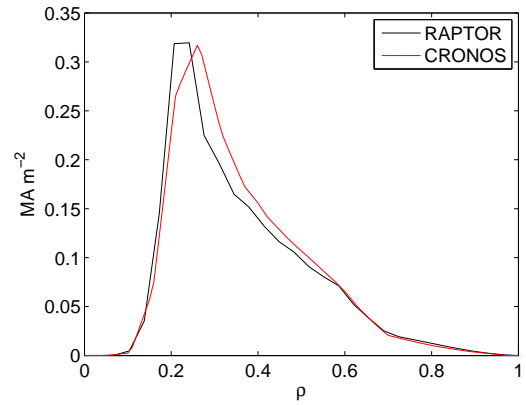
Figure A.15: The neutral beam current drive versus ρ calculated by the developed model and NEMO/SPOT (NBI module in the CRONOS code).

Benchmark 3: Z_{eff} variation

Figure A.16: The profiles of the electron temperature, density and Z_{eff}.

Figure A.17: The beam power to the electrons versus ρ calculated by the developed model and NEMO/SPOT (NBI module in the CRONOS code).
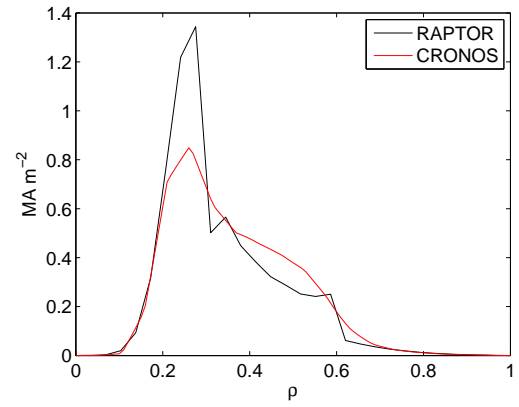

Figure A.18: The neutral beam current drive versus ρ calculated by the developed model and NEMO/SPOT (NBI module in the CRONOS code).

Benchmark 4: n_e, T_e and $\mathbf{Z}_{eff}$ variation

Figure A.19: The profiles of the electron temperature, density and Z_{eff}.

Figure A.20: The beam power to the electrons versus ρ calculated by the developed model and NEMO/SPOT (NBI module in the CRONOS code).

Figure A.21: The neutral beam current drive versus ρ calculated by the developed model and NEMO/SPOT (NBI module in the CRONOS code).

Appendix B

Model parameter optimization

B.1 Derivatives of χ_e and σ to its model parameters

$$\frac{\partial \chi_e}{\partial \chi_{neo}} = 1$$

$$\frac{\partial \chi_e}{\partial c_{ano}} = \rho q F(s) \left(\frac{T_{e_0}[eV]}{1000}\right)^{c_{T_e}}$$

$$\frac{\partial \chi_e}{\partial \chi_{central}} = e^{\rho^2/\delta_0^2},$$

$$\frac{\partial \chi_e}{\partial c_{\chi saw}} = G(q)$$

$$\frac{\partial \chi_e}{\partial c_{T_e}} = c_{ano} \rho q F(s) \left(\frac{T_{e_0}[eV]}{1000}\right)^{c_{T_e}} \ln \frac{T_{e_0}[eV]}{1000}$$

$$\frac{\partial \chi_e}{\partial \delta_0} = 2\rho^2 \delta_0^{-3} \chi_{central} e^{\rho^2/\delta_0^2}$$

$$\frac{\partial \chi_e}{\partial w_{\chi saw}} = c_{\chi saw} \frac{\partial G(q)}{\partial w_{\chi saw}}$$

$$\frac{\partial \chi_e}{\partial a_{ic}} = c_{ano} \rho q \frac{\partial F(s)}{\partial a_{ic}} \left(\frac{T_{e_0}[eV]}{1000}\right)^{c_{T_e}}$$

$$\frac{\partial \chi_e}{\partial w_{ic}} = c_{ano} \rho q \frac{\partial F(s)}{\partial w_{ic}} \left(\frac{T_{e_0}[eV]}{1000}\right)^{c_{T_e}}$$

$$\frac{\partial \chi_e}{\partial d_{ic}} = c_{ano} \rho q \frac{\partial F(s)}{\partial d_{ic}} \left(\frac{T_{e_0}[eV]}{1000}\right)^{c_{T_e}}$$

B.2   Magnetic shear of TCV shots

In the figures below, the minimum magnetic shear s in the ρ interval from 0.05 to 1 is plotted versus the time evolution of the shot. These plots make clear that the shots don't represent advanced scenarios characterized by reverse shear. (Low ($s \leq 0.01$) or negative magnetic shear)
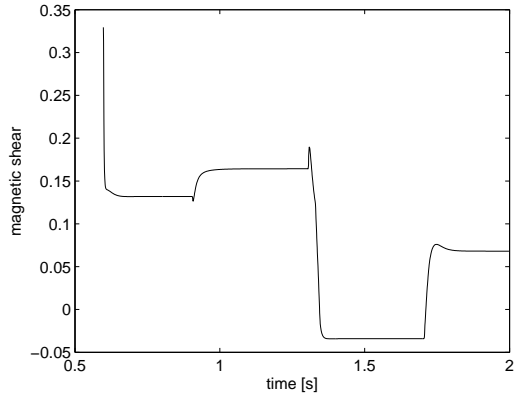

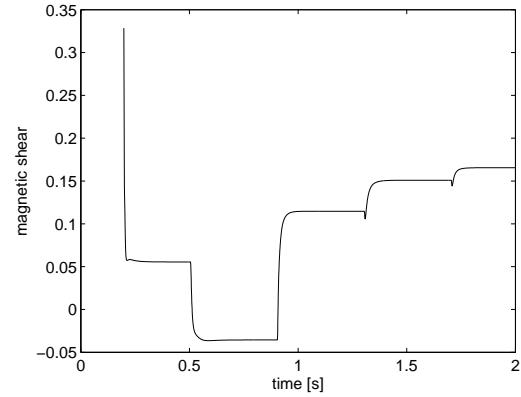Figure B.1: Minimum magnetic shear s versus time for the ECCD/ECCH shot 46712.

Figure B.2: Minimum magnetic shear s versus time for the ECCD/ECCH shot 46715.
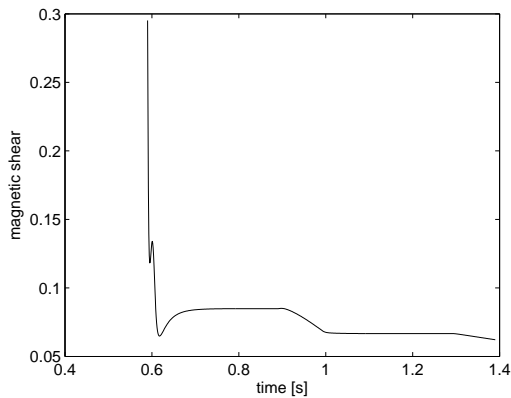

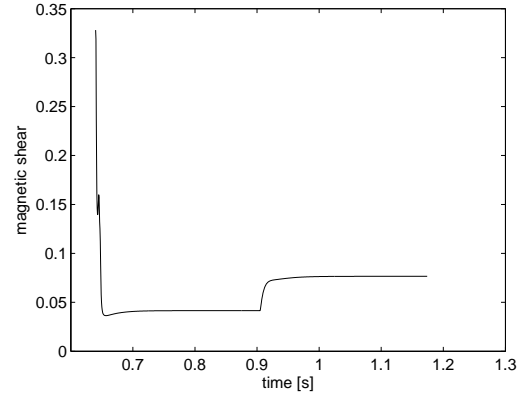Figure B.3: Minimum magnetic shear s versus time for the shot with constant ECH.

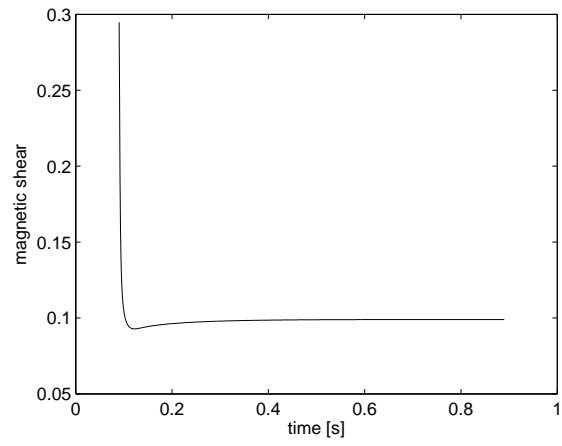Figure B.4: Minimum magnetic shear s versus time for the shot with ECH varying power.

Figure B.5: Magnetic shear s versus time for the Ohmic shot.